



**DESIGN AND CHARACTERIZATION OF OPTICAL METAMATERIALS  
USING TUNABLE POLARIMETRIC SCATTEROMETRY**

DISSERTATION

Jason C. Vap, Major, USAF

AFIT-ENP-DS-12-03

**DEPARTMENT OF THE AIR FORCE  
AIR UNIVERSITY**

***AIR FORCE INSTITUTE OF TECHNOLOGY***

---

**Wright-Patterson Air Force Base, Ohio**

APPROVED FOR PUBLIC RELEASE; DISTRIBUTION UNLIMITED

The views expressed in this dissertation are those of the author and do not reflect the official policy or position of the United States Air Force, Department of Defense, or the United States Government.

**DESIGN AND CHARACTERIZATION OF OPTICAL METAMATERIALS  
USING TUNABLE POLARIMETRIC SCATTEROMETRY**

DISSERTATION

Presented to the Faculty

Department of Electrical Engineering

Graduate School of Engineering and Management

Air Force Institute of Technology

Air University

Air Education and Training Command

In Partial Fulfillment of the Requirements for the  
Degree of Doctor of Philosophy in Electrical Engineering

Jason C. Vap, B.S.E.E., M.S.E.E

Major, USAF

December 2012

APPROVED FOR PUBLIC RELEASE; DISTRIBUTION UNLIMITED

AFIT-ENP-DS-12-03

DESIGN AND CHARACTERIZATION OF OPTICAL METAMATERIALS USING  
TUNABLE POLARIMETRIC SCATTEROMETRY

Jason C. Vap, B.S.E.E., M.S.E.E.  
Major, USAF

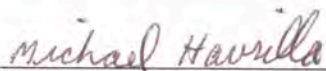
Approved:



Michael A. Marciniak, PhD (Chairman)

29 Nov 2012

Date



Michael J. Havrilla, PhD (Member)

21 Nov 12

Date



Ronald A. Coutu Jr., PhD (Member)

21 NOV 12

Date

Accepted:



M. U. Thomas  
Dean, Graduate School of Engineering  
and Management

7 Dec 12

Date

## ABSTRACT

Optical metamaterials are a class of engineered materials with a wide range of material properties and an equally wide range of anticipated applications. These materials traditionally attain their unique material properties from unit cell structures or material layers which are periodically arranged. These periodic structures are often described using effective medium theory (EMT), which is believed to remain valid so long as the EMT description of the material is applied under long wavelength conditions (*i.e.* where the incident wavelength can be assumed much larger than the unit cell or period dimensions). This condition is increasingly difficult to achieve at optical wavelengths. This problem was singled-out for negative refractive index materials, but they are not the only optical metamaterial violating these dimensional constraints. One of the simplest optical metamaterial structures was also found to be violating these constraints - a periodic layered metal-dielectric structure used to attain near-zero permittivity at a visible wavelength. In this research, a set of four periodic near-zero permittivity structures was developed. A transfer matrix method (TMM) model was found to accurately predict the experimental behavior of these structures but EMT did not. Additional modeling work was completed to demonstrate the dimensional constraints necessary for EMT predictions to match the predictions of a trusted and verified TMM model and establish a foundation for future near-zero permittivity designs.

Of additional concern in metamaterials research, theoretical predictions for metamaterials have been shown to have incident angle and incident polarization state dependencies. Furthermore, these properties are narrow-band in nature. To date, optical

metamaterials have not been subjected to full-directional, full-polarimetric characterization because there has yet to be an instrument developed with the spectral range and full-directional, full-polarimetric capabilities needed to carry out this work. This research work also addressed the instrument/characterization void in optical metamaterials research. A tunable infrared (IR) Mueller matrix (Mm) polarimeter-scatterometer was developed and operates with a fully optimized dual-rotating retarder having  $1/3$  wavelength achromatic retarders.

After developing this instrument, it was used to measure the polarimetric behavior of an infrared metamaterial absorber (MMA) at  $5.0\mu\text{m}$ . This is the first spectral, fully polarimetric and fully directional characterization reported for an optical metamaterial. The extracted Mm for this sample was found to have incident angle dependence which did not follow isotropic or anisotropic Fresnel reflectance behavior. However, the experimentally retrieved Mm is valid and was used to predict the reflected polarimetric behavior of the MMA when canonical polarization states were assumed incident on the material.

## **ACKNOWLEDGMENTS**

I would like to thank my family for their immense amount of support throughout this research work. My love for you guys is truly without bound.

I would like to thank my research advisor for his tireless support over the duration of this research, particularly in these closing months. You have forever changed another mind.

I would like to thank our post doc for his commitment to our research and his friendship over the last couple of years. You have been a great friend, and my family and I are grateful for having the opportunity to get to know you.

In closing, I would also like to thank my committee members for taking the time out of their busy research and teaching schedules to be a part of my committee.

Jason C. Vap

# TABLE OF CONTENTS

	Page
Abstract.....	iv
Acknowledgments.....	1
Table of Contents .....	2
List of Figures .....	6
List of Tables .....	11
DESIGN AND CHARACTERIZATION OF OPTICAL METAMATERIALS USING TUNABLE POLARIMETRIC SCATTEROMETRY .....	12
I. Introduction .....	12
1.1 Optical Metamaterials and Effective Media .....	12
1.2 Problem Statements.....	13
1.2.1 Validating the Use of Effective Medium Theory.....	13
1.2.2 Instrument Demand for Infrared Metamaterials Research.....	13
1.3 Research Objectives .....	14
1.4 Research Objective Accomplishment .....	15
1.4.1 EMT use in periodic metal-dielectric near-zero permittivity designs.....	15
1.4.2 Development of an IR Mm Polarimeter Scatterometer.....	15
1.4.3 Measuring and Modeling an IR Metamaterial .....	16
1.5 Organization.....	16
II. Background .....	18
2.1 Near-Zero Permittivity Structures.....	18
2.2 Dual Rotating Retarder Optimization .....	22
2.2.1 Discussion of the optimization problem .....	23
2.2.2 The unique optimization solution – random error analysis.....	24
2.3 Tunable Infrared Mueller-matrix Polarimeter-Scatterometer .....	24
2.3.1 Complete Angle Scatter Instrument .....	25
2.3.2 Practical design considerations .....	26
2.4 Mm Measurements and Modeling of Novel Metamaterial Absorber .....	28
2.4.1 The Stokes Vector and its Poincaré Sphere Representation .....	29
2.5 Conclusion .....	31
III. Modeling, Design and Experimental Analysis of Near-Zero Permittivity Structures at Optical Wavelengths.....	32
3.1 Executive Summary of Research .....	32

	Page
3.2 Introduction .....	33
3.3 Modeling .....	34
3.3.1 Transfer Matrix Method .....	34
3.3.2 Effective Medium Theory .....	36
3.4 Design .....	36
3.4.1 Designing for near-zero effective permittivity .....	36
3.4.2 Constraining the design .....	39
3.5 Experimental Results .....	41
3.5.1 Layered Material Design .....	41
3.5.2 Transfer Matrix Method .....	42
3.5.3 Effective Medium Theory .....	43
3.5.4 Model-to-Model Agreement .....	44
3.6 Discussion .....	45
3.7 Conclusion .....	46
 IV. Optimizing a Dual Rotating Retarder for a Tunable Mueller Matrix Polarimeter- Scatterometer .....	 47
4.1 Executive Summary of Research .....	47
4.2 Introduction .....	48
4.3 Theory .....	50
4.3.1 Background .....	50
4.3.2 Measurement Matrix Method .....	51
4.3.3 Condition Number Analysis .....	52
4.3.4 Fourier Method .....	53
4.3.5 Calibration Method .....	54
4.4 Error Analysis .....	55
4.4.1 Optimal Retarder Rotation Ratios .....	56
4.4.2 Creating ideal, free-space intensity signals .....	57
4.4.3 Introducing random noise .....	57
4.4.4 Experimental Results .....	61
4.5 Discussion .....	63
4.6 Conclusion .....	64
 V. Development of a Tunable Mid-Wave Infrared Mueller Matrix Polarimeter- Scatterometer .....	 65
5.1 Executive Summary of Research .....	65
5.2 Introduction .....	66
5.3 Instrument .....	67
5.3.1 Physical Layout .....	67
5.3.2 EC-QCLs .....	68
5.3.3 Achromatic Dual Rotating Retarder Polarimeter .....	70
5.4 Mm Polarimeter-Scatterometer .....	71

	Page
5.4.1 Mm Polarimeter Experimental Results .....	72
5.4.2 Mm Scatterometer Experimental Results.....	73
5.5 Discussion and Conclusion .....	75
VI. Evaluation of a Novel Optical Metamaterial Absorber .....	76
6.1 Executive Summary of Research .....	76
6.2 Introduction .....	77
6.3 IR VASE Measurements .....	78
6.4 Mm Polarimeter Measurements .....	81
6.5 Determining the Mm is physically realizable .....	82
6.6 Mm Reflectance Model.....	83
6.6.1 Un-normalized Mm Reflectance Model.....	84
6.6.2 Normalized Mm Reflectance Model .....	86
6.6.3 Fresnel Reflectance Comparisons .....	88
6.7 Example Behavior of the MMA.....	91
6.6.1 Stokes Interpretation .....	91
6.7.2 Poincaré Sphere Interpretation .....	92
6.8 Discussion and Conclusion .....	94
VII. Future Work .....	96
7.1 Metamaterial Absorbers .....	96
7.2 Releasable IR Metamaterials.....	98
7.3 Photonic Crystals .....	99
7.4 Dielectric Resonators .....	99
7.5 Conclusion .....	100
VIII. Discussion and Conclusions.....	101
8.1 Research Objective Restatement.....	101
8.2 Research Objective Accomplishment .....	101
Appendix A.....	107
A.1 Complex Refractive Index Data.....	107
A.2 Complex Permittivity Data .....	109
A.3 Practical design constraints to achieve a near zero permittivity structure .....	110
A.4 TMM and EMT model agreement .....	111
Appendix B .....	113
B.1. Mueller Matrix Model for Fresnel Reflector – Gold Mirror .....	113
B.2 Mm Polarimeter Measurements of Gold Mirror .....	116

	Page
Bibliography .....	118

## LIST OF FIGURES

	Page
Figure 2-1. The set of four Ag/AlN layered near-zero permittivity design structures on transparent substrate, where the grey layers refer to Ag and the blue layers refer to AlN. ....	20
Figure 2-2. Reflectance (red) and transmittance (blue) modeled results for [6] using TMM (a) and EMT (c) and for [7] using TMM (b) and EMT (d). ....	20
Figure 2-3. Permittivity results using mixing fractions to achieve a zero crossing for [6] (left) and [7] (right). The zero crossing of the permittivity for [6] was 580nm and 520nm for [7]. ....	21
Figure 2-4. Illustration of a dual rotating retarder (DRR) in a transmission measurement configuration. The retardances specified ( $\delta_G = \delta_A = \lambda/5, \lambda/4$ and $\lambda/3$ ) represent values examined during the optimization process. ....	22
Figure 2-5. Expected retardance curves for the 3.39 $\mu$ m quarter-wave retarder (left) and 10.6 quarter-wave retarder (right). ....	27
Figure 2-6. Measured transmission curves for the 3.39 $\mu$ m quarter-wave retarder (red) and 10.6 $\mu$ m quarter-wave retarder (blue). The approximate spectral range of each EC-QCL (each represented by an individual color) is overlaid. ....	27
Figure 2-7. The Poincaré sphere with the canonical polarization states depicted (left) and a right hand elliptical polarization state depicted (right). The ellipticity ( $\chi$ ) is measured from the $S_1S_2$ -plane, where the linear polarization states exist, and the orientation ( $\psi$ ) is measured from the $S_1$ -axis. RCP refers to right-hand circular polarization. ....	30
Figure 3-1. (a) The metal filling fraction needed to achieve a near-zero permittivity design as a function of wavelength and refractive index. (b) The dielectric thickness needed to meet the near-zero permittivity design assuming a Ag layer thickness of 20nm is used. ....	39
Figure 3-2. The left column of plots represents the <i>electrical</i> length of a dielectric as a function of refractive index and wavelength, when reduced according to (a) $\lambda/2$ , (c) $\lambda/3$ and (e) $\lambda/10$ design constraints. The right column of plots represent the region in which Figure 2-3 (b) remains valid under the (b) $\lambda/2$ , (d) $\lambda/3$ and (f) $\lambda/10$ design constraints, with the scale representing the margin in which the dielectric thickness meets the design constraint. The dotted lines on the right column plots represent dispersion curve for AlSb, AlAs, AlN, Al <sub>2</sub> O <sub>3</sub> , SiO <sub>2</sub> and MgF <sub>2</sub> from top to bottom. ....	40

- Figure 3-3. (a) Index of refraction results from ellipsometry measurements for a 22nm Ag layer compared to Palik's data [36]. The solid lines refer to Palik's data, and the markers refer to measured values. (b) Index of refraction results from ellipsometry measurements on 83nm of AlN. .... 42
- Figure 3-4. Experimental ('o' marked lines) reflectance (left) and transmittance (right) results compared to transfer matrix method modeling (solid lines) for the single- (p=1), two-, three-, and four-period (p=4) sample. The material thicknesses used were 22nm and 83nm for Ag and AlN respectively. .... 43
- Figure 3-5. EMT modeling predictions for a single- to four-period near-zero permittivity design. The material thicknesses used were 22nm and 83nm for Ag and AlN, respectively. .... 44
- Figure 3-6.  $\lambda/10$  model-to-model comparison for a four period design using 20nm silver layer thickness and the dielectric thicknesses prescribed by EMT analysis. .... 45
- Figure 4-1. Condition number plot for DRR under a 48-measurement collection configured with a  $\lambda/5$  (a) and  $\lambda/3$  (b) retarder. The x-axis refers to angular increments applied to the generator retarder, and the y-axis analyzer retarder increments. .... 53
- Figure 4-2. Condition number plot for the retardance cases tested (a)  $\lambda/5$  (b)  $\lambda/4$  and (c)  $\lambda/3$  for the retarder rotation ratios 34:26, 37.5:7.5 and 25:5. .... 57
- Figure 4-3. Ideal free-space intensity signal under three different DRR retardance conditions ( $\lambda/5$ ,  $\lambda/4$  and  $\lambda/3$ ) when the retarders are rotated under a ratio of (a) 34:26, (b) 37.5:7.5 and (c) 25:5. .... 58
- Figure 4-4. Expected error in the free-space Mm extraction for the rotation ratios,  $\theta_A:\theta_G = 34:26$  (blue), 25:5 (green) and 37.5:7.5 (red) using the three retardance restrictions (a)  $\delta=\lambda/5$ , (b)  $\lambda/4$  and (c)  $\lambda/3$  and varying the number of intensity measurements (q) when additive random errors were introduced to ideal modeled intensity measurements for the DRR configuration represented. .... 60
- Figure 4-5. Comparison of (a) modeled error in the free-space Mm extraction with the (b) experimental error for the instrument configured with  $\sim\lambda/3$  retarders in the DRR for three rotation ratio configurations ( $\theta_A:\theta_G = 34:26$ , 25:5 and 37.5:7.5). .... 62
- Figure 5-1. Physical layout of the Mueller matrix scatterometer using the following labeling conventions: TM – turning mirror; BC – beam combiner; Ch – chopper; PH – pinhole; FL – focusing lens; OAP – off-axis parabolic mirror; GP – generator-stage polarizer; GR – generator-stage retarder; AR – analyzer-stage retarder; AP – analyzer-stage polarizer. .... 68

- Figure 5-2. Nominal retardance for the achromatic waveplate designed for 7.4-10.6 $\mu\text{m}$ . Similar retardance behavior is expected for the 4.3-6.5 $\mu\text{m}$  achromatic waveplates. 71
- Figure 5-3. Mm specular reflectance plot for a novel optical metamaterial sample [33] at 5.0 $\mu\text{m}$  when the instrument was operating as a Mm polarimeter. I.e. in specular mode such that the angles represent both incident and reflected angle. .... 73
- Figure 5-4. Mm BRDF of a novel optical metamaterial sample [33] at 5.0  $\mu\text{m}$  and 25 $^\circ$  incident angle. The resonant feature of Figure 5-3 is repeated here. The periodic structure is diffraction orders generated by the periodic nature of the sample. .... 74
- Figure 5-5. Mm BRDF of a novel optical metamaterial sample [33] at 5.0  $\mu\text{m}$  and 60 $^\circ$  incident angle, illustrating the off-resonant condition. The diffraction orders seen in Figure 5-4 are again found here. .... 74
- Figure 6-1. (left) P-pol and (right) s-pol reflectance measurements taken of the MMA with increasing incident angle using the IR-VASE ..... 79
- Figure 6-2. Surface plasmon polariton resonance calculated for the MMA, using the material properties of Au at 5.0 $\mu\text{m}$  ( $\tilde{n} = 3.7 + i30.5$ ) [34] and the dielectric ( $\tilde{n} = 2.06 + 0.12i$ ) [17], while the periodic spacing  $a = 3.2\mu\text{m}$ . .... 81
- Figure 6-3. Normalized specular reflectance Mm plot for the MMA at 5.0 $\mu\text{m}$ . .... 81
- Figure 6-4. The trace of  $\text{MM}^T$  for the extracted specular reflectance Mm for the MMA at 5.0 $\mu\text{m}$ . .... 83
- Figure 6-5.  $R_s$  (green) and  $R_p$  (blue) reflectance behaviors determined from unnormalized Mm data for the MMA at 5.0 $\mu\text{m}$ . Markers represent reflectance data from the IR-VASE measurement. .... 85
- Figure 6-6. Ratio of the reflectances (top) and phase difference between the p-pol and s-pol reflectances (bottom). .... 87
- Figure 6-7. Modeled Fresnel reflectance and phase curves for gold (surface material of MMA) at 0.2 $\mu\text{m}$  (a) and (b) ( $\tilde{n} = 1.427 + i1.215$ ) and 5.0 $\mu\text{m}$  (c) and (d) ( $\tilde{n} = 3.7 + i30.5$ ). .... 89
- Figure 6-8. Modeled Fresnel reflectance curves for an anisotropic uniaxial material, where  $n_x = n_y = 3.7$ ,  $\kappa_x = \kappa_y = 30.5$ ,  $n_z = 3$  (a), 0.3 (b), 0.03 (c), and 0.003 (d)  $\kappa_z = 0.01$ . .... 90
- Figure 6-9. Predicted Fresnel reflectances using an anisotropic biaxial model ( $n_x = 0.03$ ,  $\kappa_x = 0.05$ ,  $n_y = 3.7$ ,  $\kappa_y = 30.5$ ,  $n_z = 0.45$ ,  $\kappa_z = 0.01$ ). .... 91

Figure 6-10. Stokes plots for the MMA when canonical Stokes polarization states (a) horizontal (b) $+45^\circ$ and (c) right-hand circular are applied to the extracted Mm, with the respective incident Stokes vector shown below each plot. ....	92
Figure 6-11. The ellipticity ( $\chi$ ) and major axis orientation ( $\psi$ ) of the reflected Stokes vector with linear $+45^\circ$ (left) and right hand circular (right) polarization states incident on the MMA at $5.0\mu\text{m}$ . ....	93
Figure 6-12. Traces of the reflected polarization states on the Poincaré sphere for the MMA when the incident wavelength is $5.0\mu\text{m}$ and the polarization state is linear $+45^\circ$ (left) and RHC (right). ....	94
Figure 7-1. Theoretical MMA design (top) where the available unit cell dimensions are varied to show the expected changes in the resonant response [74]. ....	97
Figure 7-2. A wide-band MMA design (left) with its measured absorption (right) [75].	97
Figure 7-3. A non-multiplexed (a) and multiplexed (b) MMA design with the measured reflectance (c) [76]. ....	98
Figure 7-4. Scanning electron microscope (SEM) image of releasable IR metamaterial flakes (left) and the spectral reflectance (right), with the right axis depicting the measured results for the flakes [77]. ....	98
Figure 7-5. SEM image (left) for a photonic crystal made of tungsten, which demonstrated a photonic bandgap over $8\text{-}20\mu\text{m}$ [78]. ....	99
Figure 7-6. SEM image of cubic dielectric array (left) with the unique reflectance and transmittance spectra (right) [79]. ....	99
Figure A-1. Comparison of complex refractive index data from Johnson [37] (a) and (c) Palik's [36] (b) and (d) for the noble metals copper (Cu), gold (Au) and silver (Ag). ....	107
Figure A-2. Modeled reflectance and transmittance spectra for a 30nm layer of Ag using the complex refractive index data from Johnson [37] (left) and Palik [36] (right).	108
Figure A-3. Comparison of complex permittivity data from Johnson [37] (a) and (c) and Palik [36] (b) and (d) for the noble metals copper (Cu), gold (Au) and silver (Ag). ....	109
Figure A-4. The real part of the complex permittivity from Palik's data [36], which show the zero crossings. ....	110

	Page
Figure A-5. EMT to TMM modeling comparison of a four period structure at the design wavelengths of 0.35 and 0.4 $\mu$ m for the refractive indexes n=2, 3 and 4.....	112
Figure A-6. EMT to TMM modeling comparison of a four period structure at the design wavelengths 0.47 and 0.55 $\mu$ m for the refractive indexes n = 2.0 and n = 4.0, respectively.....	112
Figure B-1. The modeled $m_{10}$ term of the normalized reflectance Mm for a gold mirror. ....	114
Figure B-2. The modeled $m_{22}$ , $m_{23}$ , $m_{32}$ , and $m_{33}$ terms of the normalized reflectance Mm for a gold mirror.....	114
Figure B-3. Modeled-to-measured results comparison of the $m_{22}$ , $m_{23}$ , $m_{32}$ , and $m_{33}$ elements of a Mm reflectance for a gold mirror at 3.39 $\mu$ m and 5.0 $\mu$ m.....	115
Figure B-4. Mm plot for a gold mirror at 3.39 $\mu$ m. ....	116
Figure B-5. Mm plot for a gold mirror at 5.0 $\mu$ m. ....	117

## LIST OF TABLES

	Page
Table 2-1. Ideal polarizer measurements for Stokes vector specification .....	29
Table 5-1. EC-QCLs selected for the Mm polarimeter-scatterometer.....	69
Table 5-2. EC-QCL wavelength stability performance under different bias conditions ..	69
Table 8-1 List of Contributions.....	106
Table A-1. $\lambda/10$ design values tested for TMM and EMT agreement.....	111

# DESIGN AND CHARACTERIZATION OF OPTICAL METAMATERIALS USING TUNABLE POLARIMETRIC SCATTEROMETRY

## I. INTRODUCTION

### 1.1 Optical Metamaterials and Effective Media

Optical metamaterials are a class of engineered materials, typically made from metal and dielectrics, designed to interact with optical frequencies at terahertz (THz), infrared (IR) and visible wavelengths. These materials are designed to obtain their electromagnetic behavior from a unit structure which is much smaller than the designed wavelength of interest. By having a subwavelength periodicity, they are distinguished from photonic bandgap and photonic crystal structures [1, 2]. When the unit cell and inclusion dimensions of these materials are very small in comparison to the design wavelength, the optical materials can also be afforded an effective media description [4].

Optical metamaterials' electromagnetic properties (permittivity -  $\epsilon$  and permeability -  $\mu$ ) can be considered macroscopic and afforded an effective medium theory (EMT) description by using the inclusion size ( $\delta$ ) and the unit cell period ( $a$ ) in the assessment. It has been suggested that these material features should adhere to the inequality [4]

$$0.01 < \frac{(\delta, a)}{\lambda} < 0.2. \quad (1-1)$$

Meeting these limits has been especially difficult as optical wavelengths are approached. A review of how well optical metamaterials designed for negative refractive index were adhering to these limits was shown by Soukoulis [5]. As the visible optical wavelengths were approached, the best achieved unit cell periodicity was on the order of  $a/\lambda = 0.5$ . It

was pointed out that it is difficult to argue that EMT could validly be used with this level of *constraint* and that a new design is needed to reduce the design dimensions and recover the justification of using EMT to describe the macroscopic behavior of these materials. Thus, the coexistence of an optical metamaterial and an effective medium description have been difficult to achieve.

## **1.2 Problem Statements**

### ***1.2.1 Validating the Use of Effective Medium Theory***

The valid use of EMT in optical metamaterials research is not isolated to negative refractive index materials; it is a global challenge in optical metamaterials research. This has been revealed in some of the simplest metamaterial structures, periodic layered metal-dielectric structures [6, 7, 8], which were used to achieve near-zero permittivity ( $\epsilon$ ) material properties at visible wavelengths. The near-zero permittivity property is achieved by *diluting* the metal's permittivity. This is accomplished by pairing the metal with a positive permittivity material (*i.e.* a dielectric) in a periodic, layered material design. The thickness of the dielectric is determined by EMT calculations but will not properly describe/predict the post-fabrication behavior of these materials unless an appropriate dimensional constraint is applied to the dielectric thicknesses [8].

### ***1.2.2 Instrument Demand for Infrared Metamaterials Research***

A full directional, full polarimetric instrument which can target the narrow-band features of optical metamaterials is needed to adequately experimentally determine the behavior of optical metamaterials. In particular, the instrument should target infrared (IR)

wavelengths because the natural progression of optical metamaterial designs is from IR to visible wavelengths, and would thereby permit the early identification of problems.

The theoretical predictions of metamaterial properties of interest ( $\epsilon$  and  $\mu$ ) will often depend on incident angle and the polarization state of the incident radiation [9]. The optical phenomenon of these materials, often Bragg or plasmonic resonances, are frequently narrow-band in nature [10, 11]. Typical methods of analyzing these materials have been Fourier-transform spectrometry (FTS) specular transmittance [12-15], reflectance [16-18], emission [19-25] and IR specular spectrophotometric transmittance and reflectance [26, 27] and Variable-Angle Spectrometric Ellipsometry (VASE) [10]. However, the ability to perform optical characterization of fabricated samples which are complete from a spectral, polarization and directional point-of-view has not been available to IR metamaterial researchers.

### 1.3 Research Objectives

A series of research objectives was assembled to address the use of EMT in the simplest structures of metamaterial research and address the absence of an instrument capable of meeting the full-directional and full-polarization characterization demands of IR metamaterials.

- *Model, design, fabricate and test an optical near-zero permittivity structure and identify the appropriate design constraints to apply for EMT usage in the design and post-fabrication analysis steps*
- *Develop an optimal dual rotating retarder (DRR) polarimeter which is compatible with mid-wave infrared (MWIR, 4.37-6.54 $\mu\text{m}$ ) and long-wave infrared (LWIR, 7.41-9.71 $\mu\text{m}$ ) wavelengths*

- *Develop the first tunable IR Mm polarimeter-scatterometer for the characterization of IR optical metamaterials*
- *Measure an IR metamaterial with the tunable IR Mueller matrix (Mm) polarimeter, determine the appropriate model needed to replicate the experimental results, and perform polarimetric analysis using canonical polarization states to describe the measured results*

## **1.4 Research Objective Accomplishment**

The research objectives in this research were primarily accomplished in a model, design, and then experimentally verify approach.

### ***1.4.1 EMT use in periodic metal-dielectric near-zero permittivity designs***

Models were built and used to deduce the experimental behaviors seen in near-zero permittivity research conducted at visible frequencies [6, 7]. The findings were that a transfer matrix method (TMM) model predicted the behavior and an EMT-derived model, although leveraged in the design steps, did not accurately predict the experimental results. Novel research steps were taken in this document to design and develop a series of near-zero permittivity structures to make clear the model that produces the experimental findings is the TMM model. The design constraints necessary for reaching agreement between the TMM and EMT models were then found and used to identify the design region where EMT could validly be used in the design and experimental analysis steps [8].

### ***1.4.2 Development of an IR Mm Polarimeter Scatterometer***

The development of a tunable IR Mm polarimeter-scatterometer is a multi-faceted problem. The starting point was a Schmitt Measurement Systems (SMS) Complete Angle Scatter Instrument (CASI®) and optics capable of implementing a DRR polarimeter at 3.39 $\mu\text{m}$  and 10.6 $\mu\text{m}$ . This instrument needed beam train modifications to introduce a

series of tunable external-cavity quantum cascade lasers (EC-QCLs) and a set of experimental methodologies that could be used to leverage the use of the 3.39 $\mu\text{m}$  and 10.6 $\mu\text{m}$  optical components. When it was determined that a DRR design, compatible with the EC-QCLs, could not be achieved with the on-hand optics [28], the findings were applied to a new research objective directed at determining the best possible design. The optimal design was determined using a novel modeling approach [29, 30] and, when implemented, it led to the first third-wavelength DRR design to be used in a Mm scatterometer [31].

#### ***1.4.3 Measuring and Modeling an IR Metamaterial***

The abilities of the tunable IR Mm polarimeter-scatterometer were confirmed when the first Mm-polarimeter measurements were collected on an IR metamaterial absorber (MMA) [33]. The MMA was found to have an incident angle depend resonance, which was captured with Mm polarimetry measurements conducted at 5.0 $\mu\text{m}$ . Modeling steps were then used to distill the polarized reflectance and reflectance phase information which was responsible for this behavior. Additionally, example behaviors of this material under the influence of incident canonical polarization states were analyzed and explained from using the extracted Mm results.

### **1.5 Organization**

This document is organized according to the accomplishment of each of the research objectives, which are preceded with background material and followed with conclusions. Chapter 2 provides background information needed to introduce the material covered in Chapters 3-6. Chapter 3 covers the modeling, design, fabrication and

experimental analysis of near-zero permittivity structures. Chapter 4 covers the development of the DRR needed for the wavelength tunable, polarimetric IR instrument. Chapter 5 covers the development of the tunable IR Mm polarimeter-scatterometer and the novel measurements validating its use. Chapter 6 covers the unique measurements, modeling and polarimetric analysis of an IR metamaterial. Chapter 7 covers future work following the successful development of the tunable IR Mm polarimeter-scatterometer, where several recently developed IR samples from literature are identified. Chapter 8 covers the overall conclusions to the research contained in this document.

## II. BACKGROUND

The goal of this chapter is to provide the background material for the problems confronted in this research. Each section is aligned with a research objective and a chapter of this document.

### 2.1 Near-Zero Permittivity Structures

The contents of this section provide the background information needed to introduce the research covered in Chapter 3 “Modeling Design and Experimental Analysis of Near-Zero Permittivity Structures at Optical Wavelengths.”

Tailoring the permittivity ( $\epsilon$ ) of materials is a broad metamaterial topic. The field of research was restricted to stratified, composite materials directed at achieving a near-zero permittivity. This research recently became relevant when the near-zero permittivity property was theoretically predicted to be useful for enhancing the transmission of extraordinary transmission devices [32]. Two attempts at developing these material properties at optical frequencies in the visible have been conducted [6, 7] by using metal-dielectric layered media. Effective medium theory (EMT) and mixing fractions were used to arrive at the dielectric material design thicknesses, while the metal used (silver - Ag) was restricted to thicknesses on the order of 20-30nm (where a continuous layer that is still transmissive can be achieved). Claims at achieving the near-zero permittivity were made despite clear evidence that the material layers used were too thick, leading to oscillatory behavior in the measured reflectance and transmittance spectra. There were no attempts to restrict the dielectric thickness to levels necessary to leverage EMT in the design and post-fabrication analysis steps.

The novel approach taken in my research was to first design a near-zero permittivity structure consistent with literature through the use of EMT and mixing fractions, then show the appropriate theory for modeling and post fabrication predictions should be the transfer matrix method (TMM) [8, 35] (unless appropriate design constraints are imposed, *i.e.* dielectric thicknesses). The EMT design would then be expanded to look at a range of refractive index scaled dielectric thicknesses (*i.e.* electrical length) where the EMT modeling results were found to be in agreement with the TMM results – to identify the practical design constraints needed to achieve an optical near-zero permittivity design. With these design constraints imposed, the reflectance and transmittance spectra could be expected to be void of oscillatory behavior above the design wavelength and have near-zero permittivity properties at the design wavelength.

In order to carry this research out, the development of four periodic metal-dielectric (Ag/AlN, 20nm/80nm) layered structures for a 630nm near-zero permittivity crossing were specified. The fabrication was carried by Naval Air Warfare Center Weapons Division in China Lake, CA where the staff has decades of optical fabrication experience. A depiction of the samples is shown in Figure 2-1. The TMM and EMT modeling are covered in Chapter 2, along with the near-zero permittivity design methodology, which shows how to arrive at a dielectric thickness that will deliver a zero permittivity crossing at a desired wavelength.

The origin of the oscillatory features became clear when the TMM and EMT models were built to replicate the experimental data in the near-zero permittivity designs found in [6] and [7]. The TMM- and EMT-derived results are shown in Figure 2-2 and provided the impetus for this research – the TMM and EMT results were clearly not in

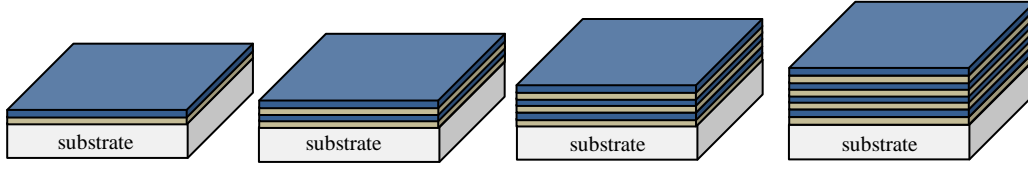


**Figure 2-1. The set of four Ag/AlN layered near-zero permittivity design structures on transparent substrate, where the grey layers refer to Ag and the blue layers refer to AlN.**

agreement. Figure 2-3 is used to show the zero permittivity crossing for each of the designs [6, 7], which comes from using the EMT (essentially volumetrically averaging the materials) in the design steps. It should be noted here that Palik's bulk material data

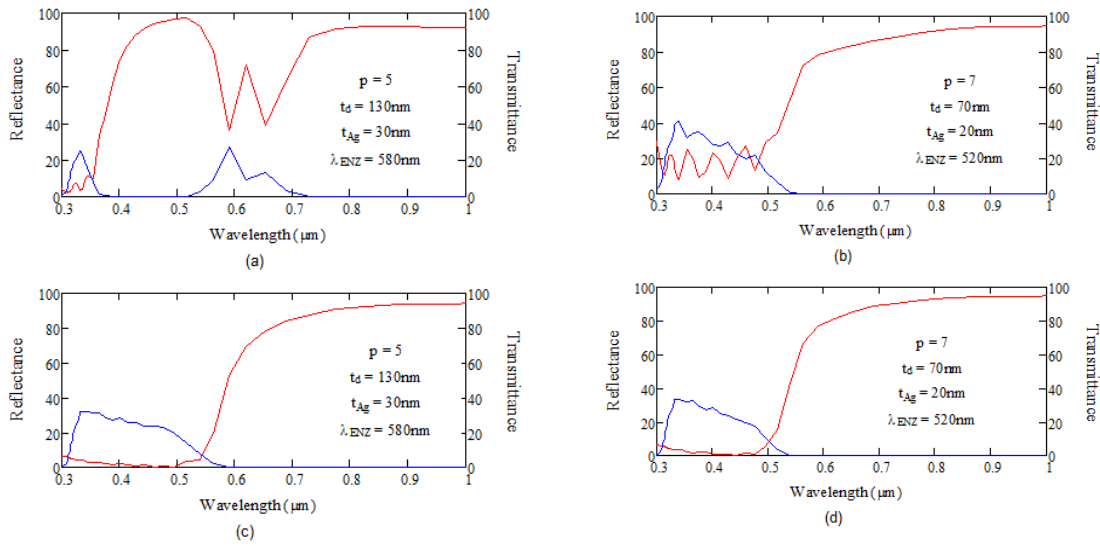


**Figure 2-2. Reflectance (red) and transmittance (blue) modeled results for [6] using TMM (a) and EMT (c) and for [7] using TMM (b) and EMT (d).**

for Ag [36] was used to generate the plots found in Figures 2-2 and 2-3. It was found to achieve the best agreement between the model and experimental results. Appendix A spends some time elucidating the details on why Palik's [36] rather than Johnson's bulk data [37] provides more accurate results at the optical wavelengths in these design regions.

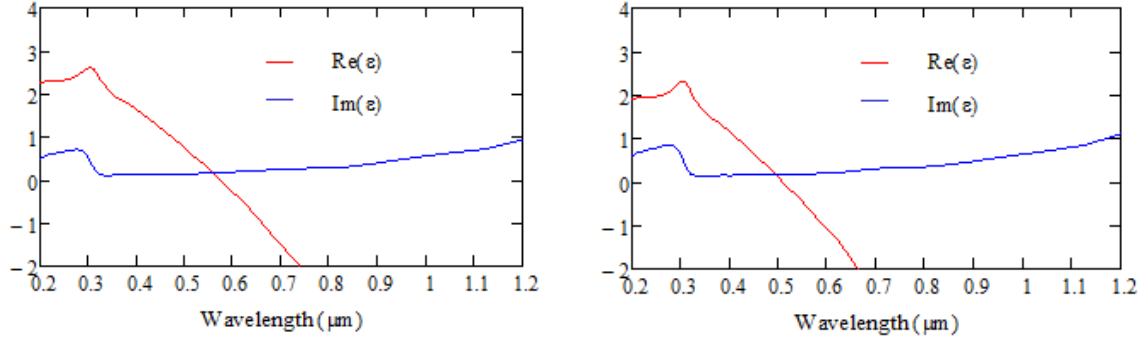


**Figure 2-3. Permittivity results using mixing fractions to achieve a zero crossing for [6] (left) and [7] (right). The zero crossing of the permittivity for [6] was 580nm and 520nm for [7].**

On a final note here, a brief discussion is needed to understand what kind of result should be predicted from a near-zero permittivity design. The short answer is it should behave as a perfect reflector because it emulates an infinite impedance mismatch with free-space. This reflective condition is readily accessible by first examining the relationship between the permittivity ( $\epsilon$ ) and refractive index ( $n$ )

$$n = \sqrt{\epsilon / \mu}, \quad (2-1)$$

where  $\mu$  refers to the permeability of the material. At optical frequencies, the permeability of materials is generally unity, leading to a simplification of the relationship and shows a near-zero permittivity leads to a near-zero refractive index. When a near-zero refractive index is inserted into the Fresnel reflectance equation (at normal

incidence),  $R = \left( \frac{n_0 - n_{ENZ}}{n_0 + n_{ENZ}} \right)^2$  the strong reflective character is predicted since the

reflectance ( $R$ ) evaluates to unity. High reflectivity is predicted in the near-zero permittivity plots of Figure 2-2, just after the intersection of the transmittance and

reflectance curves, and will similarly be manifested in the TMM modeling results when the appropriate design dimensions are applied [8].

## 2.2 Dual Rotating Retarder Optimization

The contents of this section provide the background information needed to introduce the research covered in Chapter 4 “Optimizing a Dual Rotating Retarder for a Tunable Infrared Mueller-Matrix Polarimeter-Scatterometer.”

A dual rotating retarder (DRR) is considered a complete polarimeter, that is, it leads to the full polarimetric specification of a sample under test through determining the Mueller matrix (Mm) of that sample [38]. A diagram of a DRR is shown in Figure 2-4, which shows two fixed linear polarizers that are co-aligned and two linear rotating retarders, one in front of and one behind the sample under analysis. The linear polarizer

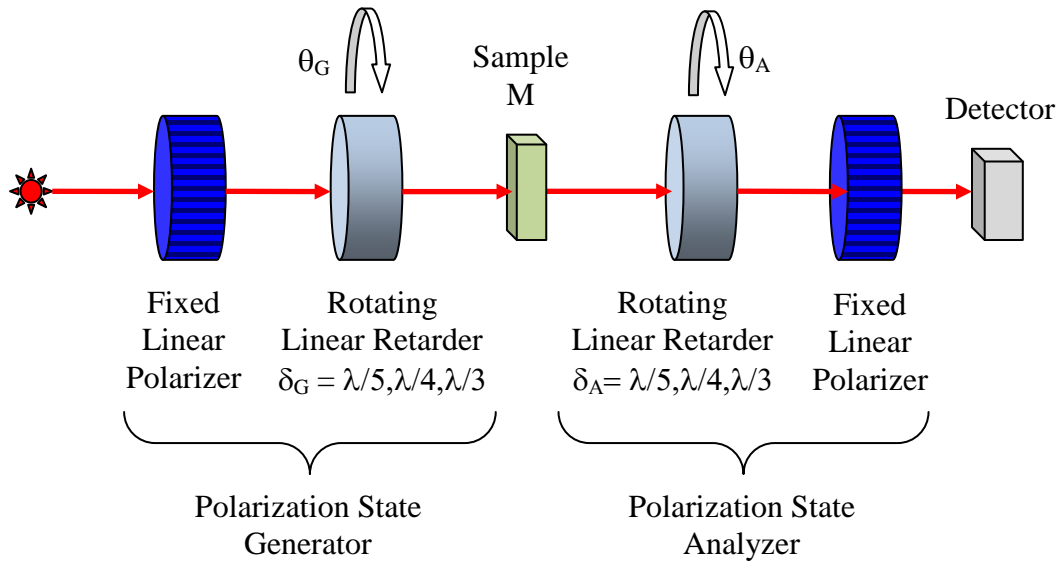


**Figure 2-4. Illustration of a dual rotating retarder (DRR) in a transmission measurement configuration. The retardances specified ( $\delta_G = \delta_A = \lambda/5, \lambda/4$  and  $\lambda/3$ ) represent values examined during the optimization process.**

and retarder in front of the sample make up the polarization state generator (PSG) stage, and the linear polarizer and retarder behind the sample make up the polarization state analyzer (PSA) stage. As shown, the DRR is in a transmission configuration, but the PSA can be rotated about the sample to operate in reflection too. Here, it can be used to observe specular reflection from the sample (acting like a Mm polarimeter) or off-specular angles to observe the polarimetric content of scatter (acting like a Mm scatterometer).

### ***2.2.1 Discussion of the optimization problem***

The simplest equation representing the measurement of a sample with a DRR polarimeter is

$$I = WM, \quad (2-2)$$

where  $I$  represents a matrix of the intensity measurements collected for incremental retarder rotation positions,  $W$  is a matrix representing the optical components of the DRR, and  $M$  represents the Mm of the sample under test. There are two pieces to the optimization problem. First, all the optical components are summed up in  $W$ . If these components are not well-known, or if there are misalignments among the optical components, systematic errors will be introduced to the intensity signal. These systematic errors will subsequently be introduced to the Mm of the sample ( $M$ ) when a  $W$ -matrix that does not accurately represent the DRR is used in the inversion process of Eqn. (2-2) to find  $M$ . Second, if  $W$  is well-known but ill-conditioned (too little retardance, too few measurements, or a poorly selected rotation ratio), then high levels of error can be introduced to the extracted Mm [39]. It is a calibration technique that mitigates the first problem [39, 40]. It is the body of research, contained in Chapter 4, that uniquely

addresses the second problem and led to the first third-wavelength achromatic DRR to be used in a Mm scatterometer [29, 30].

### ***2.2.2 The unique optimization solution – random error analysis***

Three retardance values are shown in Figure 2-5, fifth, fourth and third-wavelength ( $\lambda/5$ ,  $\lambda/4$  and  $\lambda/3$ , respectively) and represent: the retardance available during the initial design stages of the tunable Mm scatterometer development; the common DRR retardance configuration for the Fourier method [41]; and the optimal retardance configuration [42, 43]. High levels of error from measurements collected with the DRR using  $\lambda/5$  retarders (which were on-hand), despite employing optimization methods from [43]. It was by mathematically applying a constant level of random error to free-space intensity measurements ( $I$  in Eqn. (2-2), with  $M$  as the identity matrix), and varying the retardance and rotation ratios (each contained in  $W$  of Eqn. (2-2)), that the origin of the error was determined. It was insufficient retardance [28]. This same process was then used to determine the optimal DRR configuration – a Fourier retarder rotation ratio and  $\lambda/3$  retarders were found to be optimal [29, 30].

## **2.3 Tunable Infrared Mueller-matrix Polarimeter-Scatterometer**

The contents of this section provide the background information needed to introduce the research covered in Chapter 5 “Development of a Tunable Infrared Mueller-Matrix Polarimeter-Scatterometer.” The previous section and the contents of Chapter 4 dealt with DRR operating theories, calibration methods and the modeling used to identify the optimal DRR configuration for the tunable IR Mm polarimeter-scatterometer. This section examines the starting point of the instrument, practical

implementation of the DRR configuration to ensure compatibility with the set of tunable external-cavity quantum cascade lasers (EC-QCLs).

### 2.3.1 Complete Angle Scatter Instrument

The starting point for the tunable infrared (IR) Mueller-matrix (Mm) polarimeter-scatterometer development was a Schmitt Measurement Systems (SMS) Complete Angle Scatter Instrument (CASI®). In its original state, the CASI® was a scalar scatterometer, that is, it measured the scalar form of the bi-directional scatter distribution function (BSDF) of a sample by transmission or reflection measurements. The BSDF has units of  $\text{steradian}^{-1}$  defined according to [44]

$$f_{BSDF} = \frac{L(\theta_s, \phi_s)}{E(\theta_i, \phi_i)} \text{sr}^{-1}, \quad (2-3)$$

where  $L$  is the scattered radiance (in reflection or transmission),  $\theta_s$  is the observed scatter angle,  $\phi_s$  is the observed scatter azimuth angle,  $E$  is the irradiance,  $\theta_i$  is the incident angle, and  $\phi_i$  is the incident azimuth. For in-plane measurements,  $\phi_s - \phi_i = 180^\circ$ . The polarimetric form of the instrument is realized with the introduction of the DRR. In the polarimetric form, the BSDF becomes a Mm according to [45]

$$L(\theta_s, \phi_s) \begin{bmatrix} S_0 \\ S_1 \\ S_2 \\ S_3 \end{bmatrix}_{out} = \begin{bmatrix} f_{00} & f_{01} & f_{02} & f_{03} \\ f_{10} & f_{11} & f_{12} & f_{13} \\ f_{20} & f_{21} & f_{22} & f_{23} \\ f_{30} & f_{31} & f_{32} & f_{33} \end{bmatrix} E(\theta_i, \phi_i) \begin{bmatrix} S_0 \\ S_1 \\ S_2 \\ S_3 \end{bmatrix}_{in}, \quad (2-4)$$

where  $\mathbf{S}_{in}$  is a Stokes vector (discussed in Section 2.4) representing the polarization state which is incident on the sample and  $\mathbf{S}_{out}$  represents the polarization state after encountering the sample. It is in this form that the mechanics of operating the instrument

as a scatterometer versus a polarimeter can be seen. When  $\theta_i$  is held constant but  $\theta_s$  is allowed to vary during measurements, the instrument is operated as a scatterometer. When  $\theta_i$  and  $\theta_s$  are equal, and  $\phi_s - \phi_i = 180^\circ$ , the instrument is operated as a polarimeter. The later of these configurations is generally exercised for very specular samples, while the former is exercised with a sample having diffuse or diffractive qualities. The Mm polarimeter functionality was introduced to the instrument during this research using external programming features.

### ***2.3.2 Practical design considerations***

The CASI® contained four different laser sources: 633nm, 533nm, 3.39 $\mu$ m and 10.6 $\mu$ m. Optics were available to implement a DRR at each of the discrete wavelengths. Two primary tasks for developing the tunable IR Mm polarimeter-scatterometer were identified at the beginning of this research: modify the existing optical beam train to introduce the six tunable EC-QCLs to the CASI®; and determine a way to use the existing sets of IR quarter-wave retarders for a DRR which is compatible with the six EC-QCLs. The beam train modifications are covered in Chapter 5. The findings from the attempts to implement the DRR with the existing set of quarter-wave retarders are covered here.

The difficulty with implementing a DRR to be compatible with the EC-QCLs using existing 3.39 $\mu$ m and 10.6 $\mu$ m quarter-wave retarders can be summarized with: the hind-sight knowledge presented in Section 2.2 (retardances less than  $90^\circ$  should generally be avoided); the modeled retardance for the retarders in Figure 2-5; and the spectral transmission curves for the retarders in Figure 2-6. First, Figure 2-5 shows the 3.39 $\mu$ m

retarders should not be considered due to a lack of retardance. This figure does suggest the 10.6  $\mu\text{m}$  retarders may be viable down to 7.0  $\mu\text{m}$  (where the modeled retardance reaches  $135^\circ$ ), but the EC-QCL source covering this wavelength range broke and was

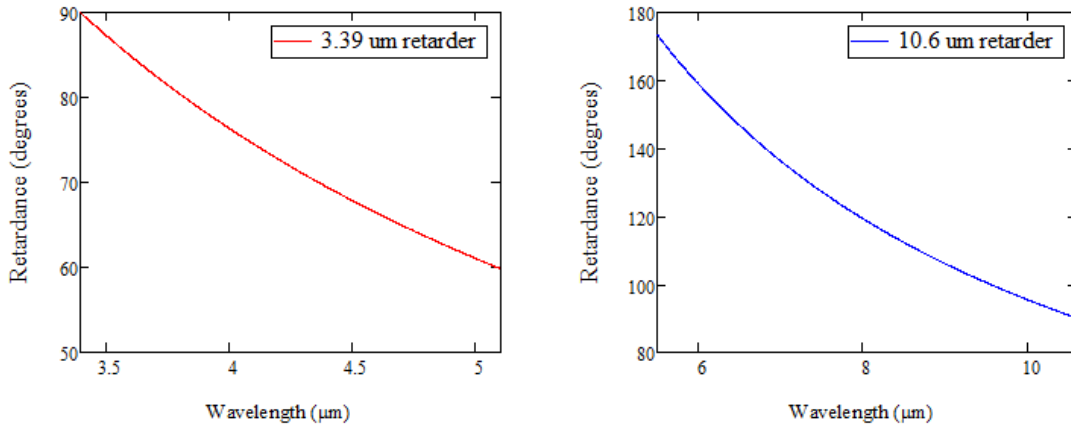


**Figure 2-5. Expected retardance curves for the 3.39 $\mu\text{m}$  quarter-wave retarder (left) and 10.6  $\mu\text{m}$  quarter-wave retarder (right).**

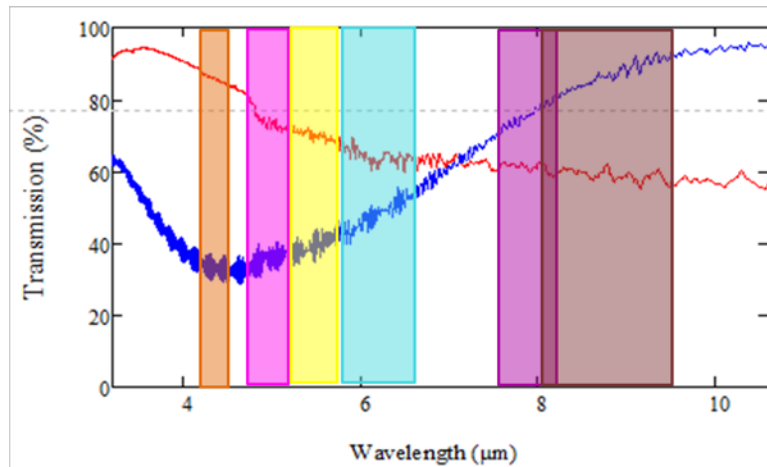


**Figure 2-6. Measured transmission curves for the 3.39 $\mu\text{m}$  quarter-wave retarder (red) and 10.6  $\mu\text{m}$  quarter-wave retarder (blue). The approximate spectral range of each EC-QCL (each represented by an individual color) is overlaid.**

unavailable for over 6 months. Figure 2-6 shows why the 3.39  $\mu\text{m}$  and 10.6  $\mu\text{m}$  quarter-wave retarders should generally be avoided. The anti-reflective coatings did not span the

wavelengths covered by the EC-QCLs (4.35-9.71 $\mu\text{m}$ ). These findings led to the research work covered in the previous section and illustrate non-trivial steps in the development of this instrument.

## **2.4 Mm Measurements and Modeling of Novel Metamaterial Absorber**

The contents of this section are used to briefly introduce the material to be covered in Chapter 6 “Evaluation of a Novel Optical Metamaterial Absorber.”

A metamaterial absorber (MMA) [33] was the first sample analyzed with the Mm polarimeter-scatterometer. An IR variable angle spectrometric ellipsometer (IR-VASE) was used to examine the p-polarized and s-polarized reflectances of the sample for resonant features of interest in the tunable range of the Mm polarimeter-scatterometer. A narrow-band feature with incident angle dependence was found at 5.0 $\mu\text{m}$ , which was subsequently analyzed with the Mm polarimeter-scatterometer. A Mm reflectance model was used to interpret the findings [38], while Fresnel reflectance models (isotropic, uniaxial anisotropy and biaxial anisotropy) were evaluated for agreement with the findings. The Mm reflectance model had been successfully used to corroborate Mm polarimeter measurements conducted on a gold mirror following the instrument development and was leveraged in the Mm analysis of the MMA in Chapter 6.

Most importantly, the measured Mm for the MMA was found physically realizable. This permitted follow-on polarimetric analysis of the MMA using the measured Mm results. Example behavior of the MMA was modeled under the assumption canonical polarization states incident on the material. These were analyzed via Stokes and Poincaré sphere representations. Background information on Stokes

vectors and Poincaré sphere are provided here, while the Mm reflectance model is covered in Chapter 6.

#### **2.4.1 The Stokes Vector and its Poincaré Sphere Representation**

A first principles development of the Stokes vector can be found in [46]. However, it is the phenomenological definition of the Stokes vector [38] and its specification in terms of the angles  $\chi$  and  $\psi$  in the Poincaré sphere [46] that led to the greatest insight into interpreting the behaviors of an extracted Mm. So, it is the phenomenological representation of the Stokes vector and its Poincaré sphere representation that is presented here.

The Stokes vector is a four element vector which fully defines the polarization state of an optical signal. It can be constructed from a series of six intensity measurements with *ideal* polarization elements [38]. The ideal polarizer measurements are listed in Table 2-1.

**Table 2-1. Ideal polarizer measurements for Stokes vector specification**

$I_H$	Intensity measurement from a linear polarizer oriented at $0^\circ$
$I_V$	Intensity measurement from a linear polarizer oriented at $90^\circ$
$I_{45}$	Intensity measurement from a linear polarizer oriented at $45^\circ$
$I_{135}$	Intensity measurement from a linear polarizer oriented at $135^\circ$
$I_R$	Intensity measurement from a right hand circular polarizer
$I_L$	Intensity measurement from a left hand circular polarizer

These measurements can be used to specify the Stokes vector by

$$S = \begin{bmatrix} S_0 \\ S_1 \\ S_2 \\ S_3 \end{bmatrix} = \begin{bmatrix} I_H + I_V \\ I_H - I_V \\ I_{45} - I_{135} \\ I_R - I_L \end{bmatrix}. \quad (2-5)$$

The Stokes vector can also be specified in terms of the angles  $\chi$  (ellipticity) and  $\psi$  (orientation) in the Poincaré sphere to visually depict the polarization state [46]. The Stokes vector can also be represented in terms of  $\chi$  and  $\psi$ .

$$\mathbf{S} = \begin{bmatrix} S_0 \\ S_1 \\ S_2 \\ S_3 \end{bmatrix} = \begin{bmatrix} 1 \\ \cos(2\chi)\cos(2\psi) \\ \cos(2\chi)\sin(2\psi) \\ \sin(2\chi) \end{bmatrix} \quad (2-6)$$

If the Stokes vector is known, the values  $\chi$  and  $\psi$  for a Poincaré sphere illustration of the Stokes polarization state can be found. Figure 2-7 illustrates the Poincaré sphere. The linear polarization states reside on the equator. The right-hand circular state resides at the north pole, and the left hand circular state resides at the south pole. The right hand elliptical states reside between the equator and the north pole, and the left hand elliptical states reside between the equator and the south pole.

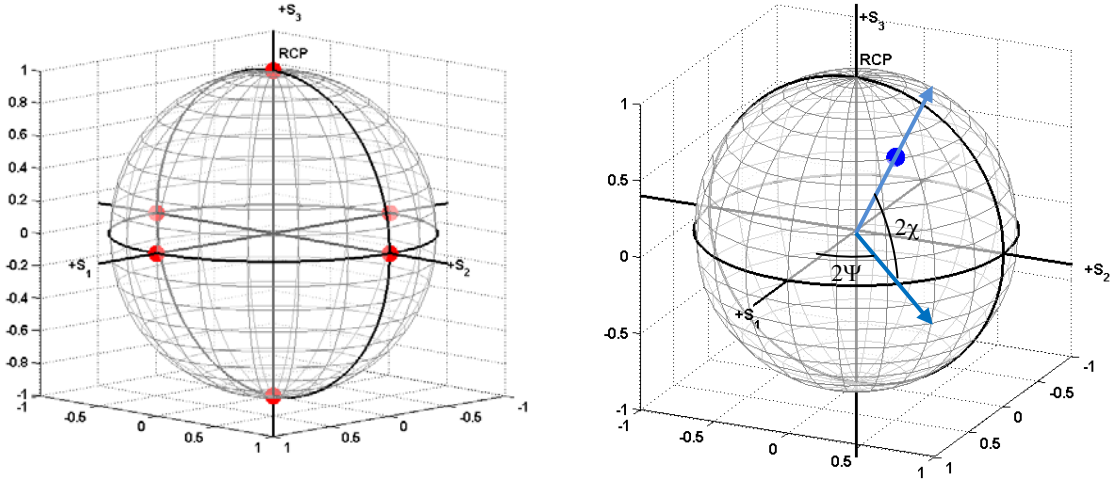


**Figure 2-7. The Poincaré sphere with the canonical polarization states depicted (left) and a right hand elliptical polarization state depicted (right). The ellipticity ( $\chi$ ) is measured from the  $S_1S_2$ -plane, where the linear polarization states exist, and the orientation ( $\psi$ ) is measured from the  $S_1$ -axis. RCP refers to right-hand circular polarization.**

## **2.5 Conclusion**

This chapter was used to introduce some of the details needed to transition into the research topics that follow in a chapter-by-chapter basis. This document was organized in a scholarly format, where Chapters 3-6 individually represent research which has either been published, submitted for publication or is in the preparatory steps of submitting for publication. The status of publications is cited in the introductory paragraph of each chapter.

### III. MODELING, DESIGN AND EXPERIMENTAL ANALYSIS OF NEAR-ZERO PERMITTIVITY STRUCTURES AT OPTICAL WAVELENGTHS

This chapter covers the research work directed at modeling, design, and experimental analysis of a set of near-zero permittivity structures. The content of this chapter has been accepted for publication in *Optics Express* [8]. The primary research contribution was determining the appropriate design constraints to apply to composite, stratified media for agreement between the transfer matrix method (TMM) and effective medium theory (EMT) modeling, thereby permitting EMT to be used in design *and* post-fabrication analysis, and equivalently, identifying the limits of its use.

#### 3.1 Executive Summary of Research

The design and analysis of near-zero permittivity structures composed of periodic metal-dielectric thin films are examined from transfer matrix method (TMM) and effective medium theory (EMT) modeling approaches. Dimensional constraints of  $\lambda/2$ ,  $\lambda/3$ , and  $\lambda/10$  are enforced for designs using silver paired with a dielectric having a refractive index in the range of 1.2 to 4.0. The wavelengths considered span 0.35 to 0.75 $\mu\text{m}$ . To ground the modeling results, a set of four  $\sim\lambda/3$  silver/aluminum nitride (Ag/AlN) near-zero permittivity structures was designed, fabricated and analyzed. Their reflectance and transmittance were found to be in excellent agreement with the TMM analysis, but in poor agreement with the EMT analysis. A  $\lambda/10$  design substantially narrows the available design region (0.35 to 0.55 $\mu\text{m}$ ) but is suggested due to the agreement found between TMM and EMT across these wavelengths.

### 3.2 Introduction

The interest in ultralow refractive index materials (ULIM's), and similarly, epsilon-near-zero (ENZ) materials at optical frequencies is growing. ULIM's with near unity index have been achieved by introducing porosity while maintaining specularly [47-51]. These ULIM's are useful for achieving anti-reflection due to their low-level of impedance mismatch with free space. They are also useful for optical confinement of solid core and air core [52] optical waveguides, where the former ULIM maintains an effective index near unity and the latter index approaches zero through a near-zero permittivity design.

Metals have a naturally occurring near-zero permittivity, which appears at their plasma frequency then becomes increasingly negative as the frequency is reduced (*i.e.* as wavelength is increased) [36]. The material response at the zero crossing in the permittivity marks where the material transitions from transmissive to highly reflective, due to the increasing imaginary component of the refractive index. Zero permittivity materials can also be engineered. This first took place for microwave frequency applications decades ago through fabricating arrays of wires which resulted in a zero-permittivity crossing [53, 54]. With the introduction of metamaterials and enhanced computational capabilities, this zero-permittivity design was later analytically extended to infrared wavelengths [55, 56]. A novel method for achieving ENZ properties has recently been achieved through manipulating the geometry of a waveguide channel rather than strictly engineering material properties [57]. Most recently, an infrared ENZ design was developed through heavily doping InAsSb to modify its dispersion behavior [34].

In this chapter, the use of mixing fractions in a layered metal-dielectric structure with a zero-permittivity design goal is examined. The modeling theory for thin films and its extension to effective medium theory (EMT) through a long-wavelength approximation are first examined. Then, the design methodology of a near-zero permittivity thin-film structure using an effective medium approach is examined. The design is completed as a function of wavelength and refractive index, and leads to a plot of dielectric thickness designs which deliver a zero-permittivity crossing. These dielectric thicknesses are then constrained for model comparison of  $\lambda/2$ ,  $\lambda/3$ , and  $\lambda/10$  designs. Experimental results for a  $\sim\lambda/3$  Ag/AlN design are then used to ground the dimensionally constrained modeling.

Similar layered media approaches have been undertaken to design zero-permittivity materials at optical wavelengths [6, 7]. The analysis completed in this chapter extends the modeling approach to find where the transfer matrix method (TMM) and EMT agree to illustrate a valid design region. A  $\lambda/3$  design corroborates the TMM modeling methodology, invalidates the use of EMT for this dimension constraint, and illustrates the need to reduce dimensionality below the  $\lambda/2$  design constraint suggested among wired arrays in early metamaterials design work [55, 56]

### **3.3 Modeling**

#### ***3.3.1 Transfer Matrix Method***

The conventional method for modeling a dielectric stack is to use a TMM, where each of the constituent layers is accounted for in a two-dimensional matrix [58]. The same approach can be used for metal-dielectric stacks, with the obvious difference being

the use of complex material properties to account for losses present in the metal layers [6]. For this modeling, only normal incidence is considered, although off-normal incidence and its corresponding polarization considerations can be accounted for in this modeling approach [58]. A single material layer is

$$M_j = \begin{bmatrix} \cos(k_0 \tilde{n}_j z_j) & -\frac{i}{\tilde{n}_j} \sin(k_0 \tilde{n}_j z_j) \\ -i\tilde{n}_j \sin(k_0 \tilde{n}_j z_j) & \cos(k_0 \tilde{n}_j z_j) \end{bmatrix} \quad (3-1)$$

where  $k_0$  is the free space propagation constant,  $\tilde{n}_j$  is the complex refractive index of the  $j$ th layer, and  $z_j$  is the thickness of that layer.

To account for a stack of materials, an iterated product of the material layers is performed starting with the top layer of the material and ending with the layer just above the substrate. The product is a characteristic matrix representing the stack of thin films ( $M_{\text{stack}}$ ).

$$M_{\text{stack}} = \prod_{j=1}^N M_j. \quad (3-2)$$

The characteristic matrix is then used to determine the amplitude reflection and transmission coefficients, which are defined in terms of the four elements of  $M_{\text{stack}}$  according to

$$r = \frac{(m_{11} + m_{12}n_{\text{sub}})n_0 - (m_{21} + m_{22}n_{\text{sub}})}{(m_{11} + m_{12}n_{\text{sub}})n_0 + (m_{21} + m_{22}n_{\text{sub}})} \quad (3-3)$$

and

$$t = \frac{2n_0}{(m_{11} + m_{12}n_{\text{sub}})n_0 + (m_{21} + m_{22}n_{\text{sub}})}. \quad (3-4)$$

The calculation of the reflectance follows the traditional form for calculating the reflectance from the amplitude reflection coefficients, while the transmittance must be scaled to account for the substrate material's refractive index ( $n_{\text{sub}}$ ).

$$R = |r|^2 \quad (3-5)$$

$$T = \frac{n_{\text{sub}}}{n_0} |t|^2 \quad (3-6)$$

### 3.3.2 Effective Medium Theory

EMT is capable of leveraging the same 2-D matrix approach with the notable exception of the iterated product. In this case, the material dimensions of a single period are assumed electrically small, which allows for the solution of an *effective* permittivity and the use of a single 2-D matrix to represent the metal-dielectric stack as a homogeneous layer (as in Eqn. (3-1)) with the index and permittivity terms replaced with effective values, and the material thickness replaced with the thickness of the stack ( $z_{\text{stack}}$ ), as in Eqn. (3-7). The reflectance and transmittance are similarly found through the use of Eqn. 3-3 through 3-6.

$$M_{\text{eff}, \text{stack}} = \begin{bmatrix} \cos(k_0 \tilde{n}_{\text{eff}} z_{\text{stack}}) & -\frac{i}{\tilde{n}_{\text{eff}}} \sin(k_0 \tilde{n}_{\text{eff}} z_{\text{stack}}) \\ -i \tilde{n}_{\text{eff}} \sin(k_0 \tilde{n}_{\text{eff}} z_{\text{stack}}) & \cos(k_0 \tilde{n}_{\text{eff}} z_{\text{stack}}) \end{bmatrix} \quad (3-7)$$

## 3.4 Design

### 3.4.1 Designing for near-zero effective permittivity

The design of a near-zero effective permittivity for a layered metal-dielectric structure are described here, and the metal filling fraction behavior of silver as a function of wavelength and dielectric refractive index is examined. In the long-wavelength limit,

the effective permittivity of a thin-film structure can be represented as a weighted average [1]. This functionally allows the permittivity to be tailored within the bounds of the constituent materials' permittivities. To calculate the effective permittivity of the material under design, the parallel component of the permittivity is used, which is represented in Eqn. (3-8). Here,  $f_m$  and  $f_d$  represent the metal and dielectric filling fractions, respectively (such that  $f_m + f_d = 1$ ), and  $\epsilon_m$  and  $\epsilon_d$  are the permittivities of the metal and dielectric, respectively.

$$\epsilon_{e,par} = f_m \epsilon_m + f_d \epsilon_d \quad (3-8)$$

A near-zero permittivity is designed by pairing a metal and dielectric in a wavelength region below the plasma frequency of the metal. In this region, the permittivity of the metal becomes increasingly negative and its contribution can be cancelled through the introduction of a dielectric which inherently possesses a positive permittivity. When the proper mixing fractions are applied, a near-zero average permittivity is achieved.

When solving for near-zero permittivity, it is in the designer's best interest to solve Eqn. (3-8) for the metal filling fraction because the layer thickness is known and is generally set to a minimum value (where a continuous film can be practically attained and still remains transmissive). With the metal layer thickness known and its filling fraction known, finding the dielectric layer thickness then becomes a straight forward process. To first solve for the metal filling fraction, the effective permittivity of Eqn. (3-8) is set to zero,  $f_m + f_d = 1$  is used to eliminate the dielectric filling fraction, and algebraic manipulation leads to the functional relationship found in Eqn. (3-9) in terms of the constituent material permittivities. When the dispersion properties and a range of

dielectric permittivities are considered in the design, the functional form for the metal filling fraction becomes dependent on wavelength and refractive index (a value with physically intuitive meaning).

$$f_m(\lambda, n) = \left( 1 - \frac{\epsilon_m(\lambda)}{\epsilon_d(\lambda, n)} \right)^{-1} \quad (3-9)$$

The behavior of the metal filling fraction  $f_m(\lambda, n_d)$  is plotted in Fig. 3-1(a), where silver was used as the metal and the range of dielectric refractive indexes spanned 1.2 to 4.0. The wavelength range of 0.35 to 0.75 $\mu\text{m}$  was selected to span visible frequencies and approach the plasma frequency of silver. Using a minimum silver thickness of 20nm, the dielectric thicknesses were solved for and are plotted in Figure 3-1(b).

Figure 3-1(a) shows that  $f_m$  increases at short wavelengths and large refractive indexes. This is due to silver's low negative permittivity, which is easily offset by a small amount of the large-positive-permittivity dielectric. At longer wavelengths and lower refractive indexes,  $f_m$  diminishes due to the increasing negative silver permittivity, as it takes a great deal of low refractive index material to offset the silver.

The dielectric thickness plot corroborates the previous explanations for the metal filling fraction. At short wavelengths and large refractive indexes, only a few nanometers dielectric are required. At long wavelengths and low refractive indexes, several hundred nanometers of dielectric are required. The range of dielectric thicknesses spans 5nm to 333nm, and thereby requires constraints to be imposed to avoid encountering unwanted resonant features in transmittance and reflectance spectra. Under the appropriate constraints, the design region where thin-film analysis and EMT results agree will be shown.

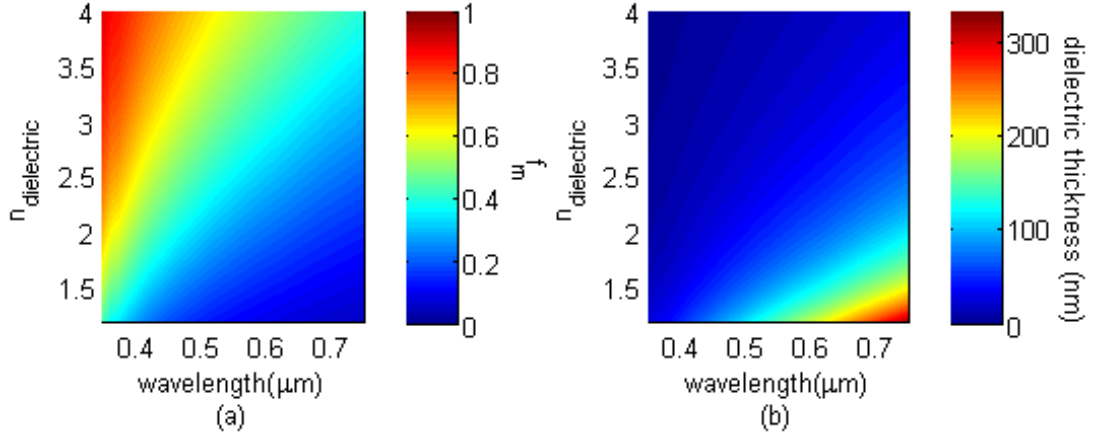


**Figure 3-1. (a) The metal filling fraction needed to achieve a near-zero permittivity design as a function of wavelength and refractive index. (b) The dielectric thickness needed to meet the near-zero permittivity design assuming a Ag layer thickness of 20nm is used.**

### 3.4.2 Constraining the design

The electrical dimension of silver is negligible across the wavelength region considered since the real part of its refractive index remains less than one. Therefore, the design is constrained based on the dielectric layer thickness. The electrical wavelength of the dielectric is simply  $\lambda_0/n_d$ , and the dielectric design values are constrained to values falling below three electrical wavelength values:  $\lambda/2$ ,  $\lambda/3$ , and  $\lambda/10$ . The  $\lambda/2$  values were considered due to early near-zero permittivity metamaterial design considerations [6, 7]. The  $\lambda/3$  values were considered based on common optical metamaterial design dimensions [5]; this is also the region near which a set of Ag/AlN near-zero permittivity design structures were developed for experimental reflectance and transmittance measurements. Finally, the  $\lambda/10$  values were considered due to their general acceptance of being considered electrically small.

Figure 3-2(a), (c), and (e) illustrate the electrical wavelength constraints for a single dielectric layer through the simple  $\lambda_0/n_d$  relationship. The dielectric design

thicknesses found in Figure 3-1(b) are then subtracted from the constrained values contained in Figure 3-2(a), (c), and (e). This produces regions of positive and negative values. The negative values refer to dielectric design thicknesses exceeding the constraint, while the positive values meet the imposed constraints (by a margin of thickness). Figure 3-2(b), (d), and (f) show these regions, with the scale reflecting the

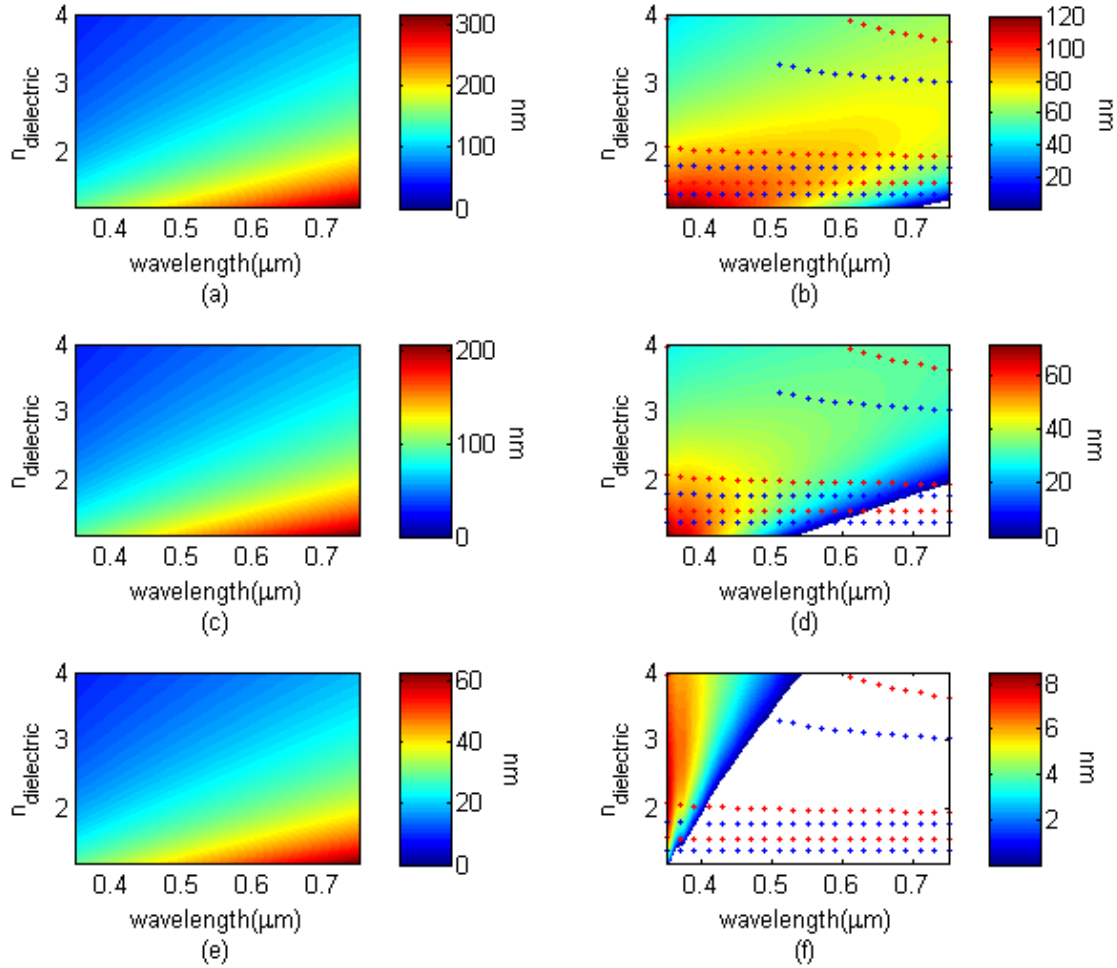


**Figure 3-2.** The left column of plots represents the *electrical* length of a dielectric as a function of refractive index and wavelength, when reduced according to (a)  $\lambda/2$ , (c)  $\lambda/3$  and (e)  $\lambda/10$  design constraints. The right column of plots represent the region in which Figure 2-3 (b) remains valid under the (b)  $\lambda/2$ , (d)  $\lambda/3$  and (f)  $\lambda/10$  design constraints, with the scale representing the margin in which the dielectric thickness meets the design constraint. The dotted lines on the right column plots represent dispersion curve for AlSb, AlAs, AlN, Al<sub>2</sub>O<sub>3</sub>, SiO<sub>2</sub> and MgF<sub>2</sub> from top to bottom.

margin of thickness by which the dielectric meets the constraints - only a few nanometers in the case of the  $\lambda/10$  design. The dotted lines refer to dispersion curves for common dielectrics; from top-to-bottom, they are AlSb, AlAs, AlN, Al<sub>2</sub>O<sub>3</sub>, SiO<sub>2</sub>, and MgF<sub>2</sub>. The next step in the analysis process is examining an actual design to determine the model-to-experiment agreement and verify the appropriate design constraint based on those results.

### 3.5 Experimental Results

#### 3.5.1 Layered Material Design

A set of four ENZ structures was designed under a  $\sim\lambda/3$  design constraint, which span one to four metal-dielectric periods. By developing this particular set of samples, the influence additional layers have on the ENZ design could be assessed; it also permitted a robust model-to-experiment verification. The materials selected for the design were silver and aluminum nitride ( $n_d = 2$ ). Silver was selected for its low loss properties at visible wavelengths and aluminum nitride was selected to eliminate oxidizing the silver layers during the deposition process. The design thickness of the silver layers was set at 20nm and the design wavelength at 630nm, which is far from silver's plasmonic resonance yet still in its low-loss wavelength regime [36]. The aluminum nitride layer thickness was determined to be 80nm, through analysis supported by Eqn. (3-8) and (3-9).

The silver/aluminum-nitride layers were deposited on an Infrasil fused silica substrate, which provided excellent material qualification results for the silver and aluminum nitride. Ellipsometry results for index of refraction ( $n_m$ ) and loss index ( $k$ ) for the silver deposition show great agreement with Palik's data [36] in Figure 3-3. The aluminum nitride was found to have a stable refractive index around 2.0 and lossless

across the wavelengths of interest, and is also shown in Figure 3-3. The deposited thicknesses of the final designs were found to be 22nm and 83nm for silver and aluminum nitride, respectively.

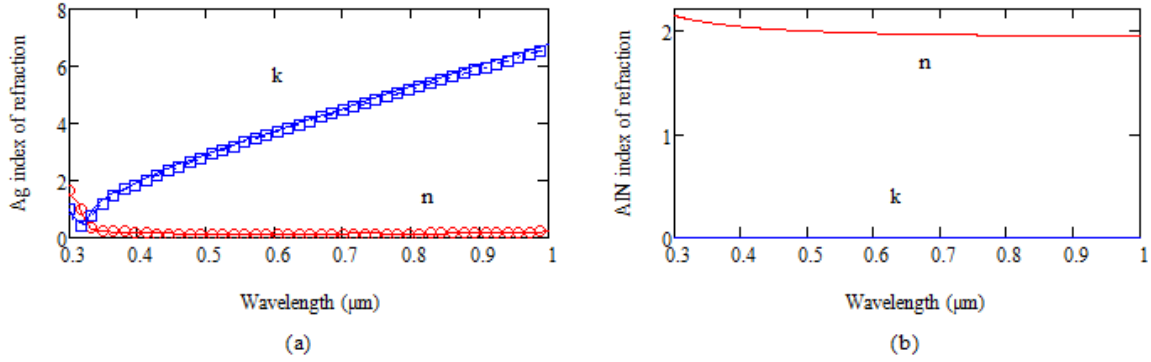


**Figure 3-3. (a) Index of refraction results from ellipsometry measurements for a 22nm Ag layer compared to Palik's data [36]. The solid lines refer to Palik's data, and the markers refer to measured values. (b) Index of refraction results from ellipsometry measurements on 83nm of AlN.**

### 3.5.2 Transfer Matrix Method

After finding the material thicknesses through ellipsometry, reflectance and transmittance measurements were collected under near-normal incidence conditions using a Perkin Elmer Lambda 950 spectrophotometer and a 150mm integrating sphere accessory. The ellipsometry-retrieved thicknesses were used in the thin-film analysis modeling described in Section 3.1 for comparison with the measured reflectance and transmittance experimental results. The comparisons are shown in Figure 3-4 with the number of periods increasing from one ( $p=1$ ) to four ( $p=4$ ) in the plots from top to bottom. Excellent agreement exists between the thin-film analysis modeling and the measured reflectance and transmittance. However, these results are not consistent with expectations for an electrically small, near-zero permittivity design. The wavelength of the incident light is still on the order of the dielectric thickness and the phase information

from individual material layers is definitely required to attain accurate experimental predictions.

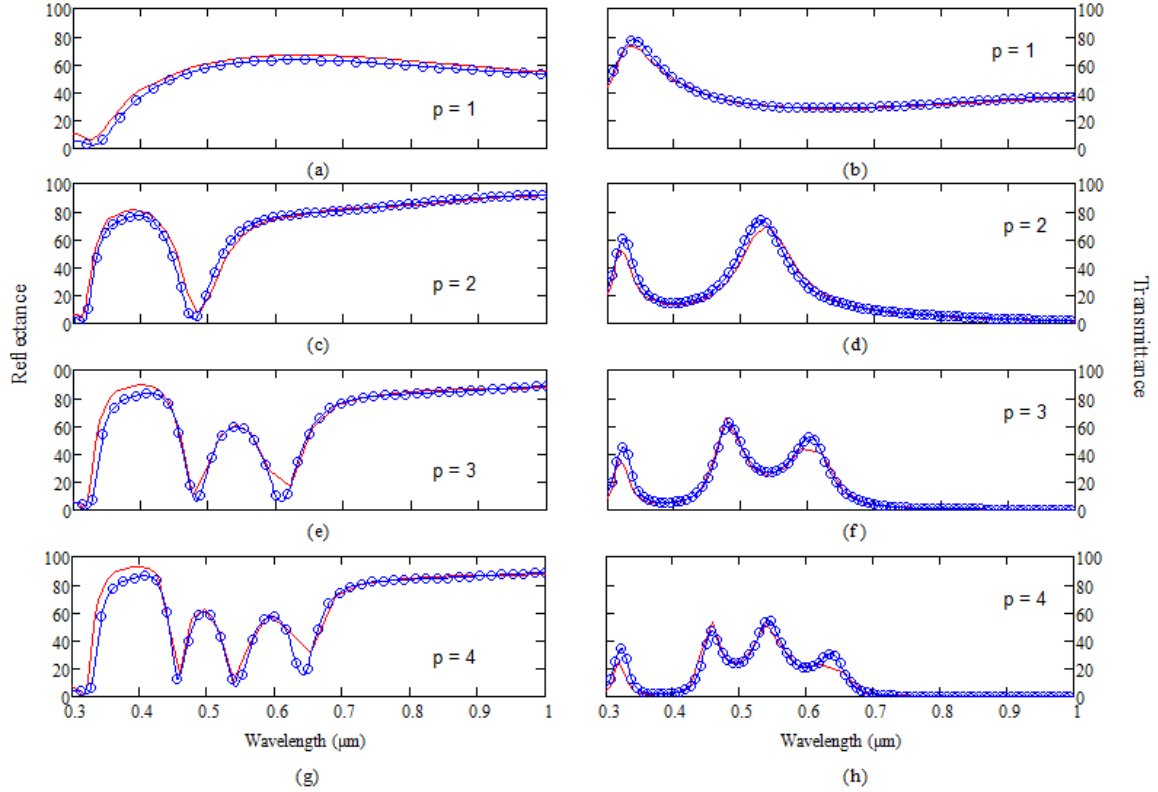


**Figure 3-4. Experimental ('o' marked lines) reflectance (left) and transmittance (right) results compared to transfer matrix method modeling (solid lines) for the single- ( $p=1$ ), two-, three-, and four-period ( $p=4$ ) sample. The material thicknesses used were 22nm and 83nm for Ag and AlN respectively.**

### 3.5.3 Effective Medium Theory

The experimental results compared to the effective-medium predictive results are not shown, but there is clearly not agreement between the two. Figure 3-5 shows the predicted reflectance and transmittance results for all four periodic structures under effective medium modeling. The transition from high transmittance to high reflectance is predicted to occur in the 630nm regime. Furthermore, as the number of periods is increased, the transmittance continues to diminish, which is expected due to the

increasing metal contribution. Based on these modeling results, further dimensional constraints are necessary to yield agreement between the EMT modeling and thin-film modeling.

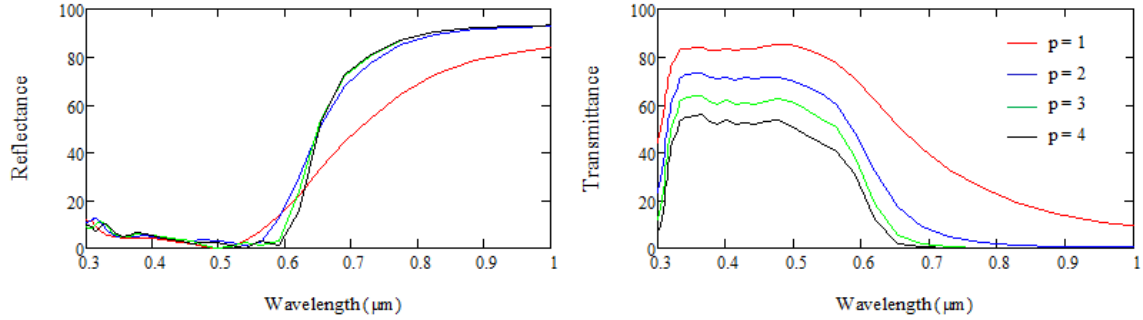


**Figure 3-5. EMT modeling predictions for a single- to four-period near-zero permittivity design. The material thicknesses used were 22nm and 83nm for Ag and AlN, respectively.**

#### ***3.5.4 Model-to-Model Agreement***

The predictive power of the thin-film analysis technique is apparent from the results shown in Section 3.5.2 and a design constraint in excess of  $\lambda/3$  is needed to achieve agreement between the TMM and EMT modeling. For this reason, comparative analysis between the two models was performed under a  $\lambda/10$  constraint. It was here that the best model-to-model agreement was observed. The perimeter of the dielectric thicknesses plotted for the  $\lambda/10$  design in Figure 3-2 was used as a means of verification, along with the values corresponding to a  $0.4\mu\text{m}$  design wavelength. These results are illustrated in Figure 3-6. While good agreement between the models exists for the  $0.4\mu\text{m}$  wavelength designs and along the left hand side of the perimeter (*i.e.* for a wavelength of  $0.35\mu\text{m}$ , with results found in Appendix A), only a reasonable level of agreement between the models exists along the diagonal edge of the perimeter, with agreement decreasing as refractive index increases. This is not a surprising result since EMT should

be used for designs where the long-wavelength limit can be assumed and the region with the worst model-to-model agreement is right at this limit.

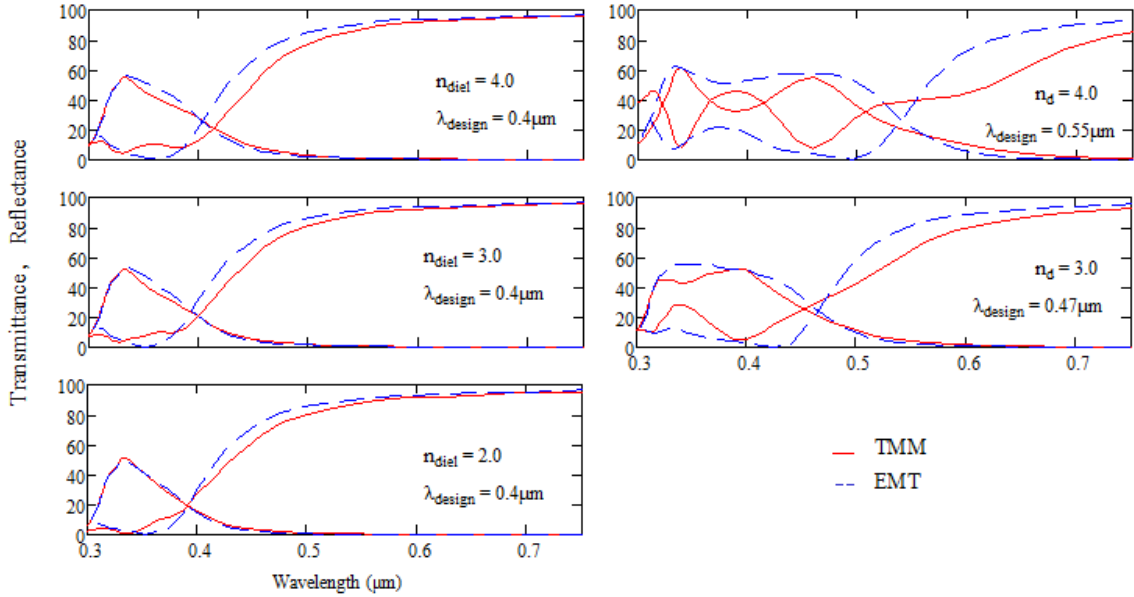


**Figure 3-6.  $\lambda/10$  model-to-model comparison for a four period design using 20nm silver layer thickness and the dielectric thicknesses prescribed by EMT analysis.**

### 3.6 Discussion

The accuracy of the  $\lambda/3$  model-to-experimental results provides a clear indication of the predictive capability of TMM to accurately model the thin films. It captures the resonant behavior of the material as additional metal-dielectric periods are added, and when the dimensions are electrically small, the layer-imposed resonances are reduced. When reviewing the transmission behavior of the  $\lambda/3$  samples, the plasmonic resonance of the silver layer in the ultraviolet remained stable among all four samples and diminished in amplitude with increasing layers, while additional resonances due to the electrically large layers of aluminum nitride situated between the highly reflective silver films grew in number as periods were added. EMT predicted broad transmission behavior below the zero permittivity crossing and reflective behavior above it. It was not until

dimensional constraints of  $\lambda/10$  were imposed on the design that EMT behavior generally followed that of TMM.

### 3.7 Conclusion

A set of four  $\sim\lambda/3$  silver/aluminum nitride (Ag/AlN) near-zero permittivity structures was designed, fabricated and analyzed. Their reflectance and transmittance were found to be in excellent agreement with the TMM analysis, but in poor agreement with the EMT analysis [8, 35]. The design was theoretically extended to include refractive indexes in the range of 1.2 to 4.0 and a wavelength design range of 0.35 to 0.75 $\mu\text{m}$ . Design constraints were applied to reach agreement between TMM and EMT models, and it was a  $\lambda/10$  constraint applied to the dielectric thicknesses that was found to yield TMM and EMT model agreement. The  $\lambda/10$  design substantially narrows the available design region (0.35 to 0.55 $\mu\text{m}$ ) but is suggested due to the agreement found between TMM and EMT across these wavelengths [8].

#### IV. OPTIMIZING A DUAL ROTATING RETARDER FOR A TUNABLE MUELLER MATRIX POLARIMETER-SCATTEROMETER

This chapter covers the dual-rotating-retarder (DRR) optimization methodology used in the development of the tunable mid-wave infrared (MWIR) Mueller matrix (Mm) polarimeter-scatterometer. The “Mm” term precedes polarimeter-scatterometer to infer the polarimetric system used is a DRR [46]. The content of this chapter has been submitted for publication in *Measurement Science and Technology Journal* in November 2012 [30]. The primary research contributions include: developing a method to predict how well a particular DRR configuration will perform as a function of measurement number; determining the Fourier retarder rotation scheme ( $5\omega:1\omega$ ) is optimal when oversampling is conducted; and leads into Chapter 5, where the first Mm scatterometer having an optimal  $1/3$  wavelength ( $\lambda/3$ ) retarder configuration was developed.

##### 4.1 Executive Summary of Research

The value of Mueller-matrix (Mm) scatterometers lies in their ability to fully characterize the polarimetric properties of samples. To extend their use to infrared (IR) optical metamaterials requires tunable lasers and an achromatic dual rotating retarder (DRR). The optimization methods used to develop the first *tunable* IR Mm scatterometer, which uses an achromatic  $\sim\lambda/3$  retardance-configured DRR, are reported in this chapter. The optimization process used is rooted in applying random error analysis to three different DRR retardance configurations ( $\lambda/5$ ,  $\lambda/4$ , and  $\lambda/3$ ) with three different retarder rotation ratios ( $\theta_A:\theta_G = 34:26$ ,  $25:5$  and  $37.5:7.5$ ) and a variable number of intensity measurements. The product of the error analysis was the level of error that could be

expected from a free-space Mm extraction when physical (retardance) and operational (retarder rotation ratio and number of intensity measurements) specifications of the DRR are made. The DRR specifications found optimal were a  $\lambda/3$  retardance configuration and a Fourier rotation ratio, with the number of measurements to collect dependent on the level of error acceptable to the user. Experimental results corroborate the error analysis findings with the achromatic  $\sim\lambda/3$  retardance-configured DRR consistently reaching 1% error in the free-space Mm extractions.

## 4.2 Introduction

Mueller-matrix (Mm) scatterometers are of increasing interest for their ability to determine the full-polarimetric behavior of materials/samples under test [59-65]. The polarimetric engine of these instruments is a dual rotating retarder (DRR), and, for low-error Mm extractions to be achieved, the retarder retardances should be on the order of  $\lambda/4$  to  $\lambda/3$  and a calibration method should be used to remove systematic errors [39, 40, 66, 67]. High-quality optics and a robust alignment procedure are assumed when using a DRR.

The retardance specification,  $\lambda/4$  to  $\lambda/3$ , was made, in general, because of the enhanced error performance that occurs when going from  $\lambda/4$  to  $\lambda/3$  and the poor error performance for retardances less than  $\lambda/4$ . These performance features may be inferred by condition number analysis [43] but become readily apparent under the random error analysis applied in this chapter. Condition number analysis was used as a starting point in the tunable infrared (IR) DRR optimization process. It was used to find low condition number retarder rotation ratios when matched with  $\lambda/5$ ,  $\lambda/4$  and  $\lambda/3$  retardance

configurations. The rotation ratios were then tested in the specified retardance configurations for robustness against random error. The Fourier rotation ratios tested were found to be optimal, and the error performance was significantly enhanced by using  $\lambda/3$  retarders rather than  $\lambda/4$  – errors in the extracted Mm were halved.

The outcome of the random error analysis was measured in the Mm error performance for each configuration with an increasing number of intensity measurements (which are referred to with the sub-script  $q$  throughout this chapter). This analysis technique was developed because of the ambiguous nature of condition number. An intuitive figure with which to optimize the instrument was needed, and it was determined that figure should be cast into the same units used to observe the calibration performance of the instrument – percentage of error in the free-space Mm extraction. By casting the analysis into Mm error percentage, the performance enhancement due to increasing retardance from  $\lambda/4$  to  $\lambda/3$  became easier to evaluate. Furthermore, decisions on where to terminate the measurement became clearer. While it is well-known that the  $\lambda/3$  retardance condition is predicted to be the optimal configuration [42, 43], it was explicitly tested here because an existing calibration technique capable of handling the use of  $\lambda/3$  retarders was found [40].

The direct use of  $\lambda/3$  retarders with Chenault's calibration technique [40] to achieve an optimal DRR configuration has not been attempted. This calibration technique was found to be robust against small retardance deviations with the DRR configured for  $3.39\mu\text{m}$  and  $\lambda/4$  retarders and was found equally valid for the achromatic  $\lambda/3$  retarders in the tunable IR instrument.

### 4.3 Theory

#### 4.3.1 Background

There are two approaches to conducting Mm analysis with DRRs. The first approach is the measurement matrix method, which was optimized by Smith [43]. Here, the retarder rotation ratio having the lowest condition number is suggested for conducting the Mm measurement. Determining the number of measurements to collect is also facilitated through condition number analysis. The second approach is the Fourier method [41] which allows the user to select from a set of rotation increments satisfying the  $5\omega:1\omega$  (analyzer retarder:generator retarder) rotation ratio, but the generator retarder must incur a half or full rotation to complete the Mm measurement. This establishes the number of measurements required to complete a Mm measurement.

The fundamental mathematical relationship for each of these methods is the same. A set of intensity measurements is collected with a 4-element Stokes vector representing the polarization state generator (PSG) stage and a 4-element row-vector representing the polarization state analyzer (PSA) stage. Between the two matrices resides the Mm of the sample to be analyzed. This is shown in Eqn. (4-1), where the  $g$  column-vector represents the PSG, the  $a$  row-vector represents the PSA and  $q$  is the measurement number [46].

$$I_q = \begin{bmatrix} a_{q,1} & a_{q,2} & a_{q,3} & a_{q,4} \end{bmatrix} * \begin{bmatrix} m_{11} & m_{12} & m_{13} & m_{14} \\ m_{21} & m_{22} & m_{23} & m_{24} \\ m_{31} & m_{32} & m_{33} & m_{34} \\ m_{41} & m_{42} & m_{43} & m_{44} \end{bmatrix} * \begin{bmatrix} g_{1,q} \\ g_{2,q} \\ g_{3,q} \\ g_{4,q} \end{bmatrix} \quad (4-1)$$

Every matrix equation can be consolidated into a summation of elements, as shown in Eqn. (4-2). This is used as leverage to separate the measurement variables from the Mm of the sample in both the measurement matrix and the Fourier method.

$$I_q = \sum_{j=1}^4 \sum_{i=1}^4 a_{q,i} * m_{i,j} * g_{j,q} \quad (4-2)$$

#### 4.3.2 Measurement Matrix Method

The measurement matrix method is grounded in linear algebra where the impetus is to mathematically isolate the Mm of the sample. This is accomplished by first reorganizing the summation from Eqn. (4-2) into the following form [46].

$$I_q = \sum_{j=1}^4 \sum_{i=1}^4 a_{q,i} g_{j,q} m_{i,j} = \sum_{j=1}^4 \sum_{i=1}^4 w_{q,i,j} m_{i,j} \quad (4-3)$$

From this, the W-matrix emerges, formulated by collecting the  $a_{q,i}$  and  $g_{j,q}$  elements. When the W-matrix is multiplied by a vectorized Mm of the sample, the intensity measurement can be constructed.

$$I_q = \begin{bmatrix} w_{q,11} & w_{q,12} & w_{q,13} & w_{q,14} & w_{q,21} & \cdots & w_{q,44} \end{bmatrix} \begin{bmatrix} m_{11} \\ m_{12} \\ m_{13} \\ \vdots \\ m_{44} \end{bmatrix}. \quad (4-4)$$

Simplifying this further, the measured intensities are seen to be a collection of row operations performed by the measurement matrix (w-matrix) on the vectorized Mm of the sample.

$$I_q = WM \quad (4-5)$$

The Mm can simply be solved as

$$M = W^{-1}I_q \quad (4-6)$$

where  $W^{-1}$  is the inverse or pseudoinverse, depending on whether the measurement space was oversampled or not.

Although not directly shown, the W-matrix is a function of retardances,  $\delta_G$  and  $\delta_A$ , and the angular rotations,  $\theta_G$  and  $\theta_A$ , of the retarders. The row-dimension of the W-matrix is dependent on the number of intensity measurements collected,  $q$ . Each of these variables is used in the condition number analysis process.

#### ***4.3.3 Condition Number Analysis.***

To achieve the least error in the extracted Mueller matrix, the W-matrix must be well-conditioned. The condition number of the W-matrix infers its level of invertibility, with a value of one indicating a completely invertible matrix and infinity indicating a singular matrix. The condition number of the W-matrix is found according to

$$cond(W) = \|W\| \|W_{pseudo}^{-1}\|, \quad (4-7)$$

where the infinity norm is used for the W-matrix and its inverse (or pseudo inverse when oversampling is conducted) [43].

The traditional way to find the optimum retarder rotation ratio is to generate a condition number plot [43] where the measurement number,  $q$ , and retardance values,  $\delta_G$  and  $\delta_A$ , are kept constant, but the angular rotations of the retarders,  $\theta_G$  and  $\theta_A$ , are allowed to vary. The global minimum (if one exists) represents the optimum retarder rotation ratio. Three retardance cases were encountered during the development of the tunable IR Mm scatterometer ( $\delta_G = \delta_A = \lambda/5$ ,  $\lambda/4$  and  $\lambda/3$ ) and those values are used throughout the analysis. The condition number plots found in Figure 4-1 represent the

analyzed retardance extremes ( $\lambda/5$  on the left and  $\lambda/3$  on the right) when 48 measurements are collected, and the angular rotations of the retarders ( $\theta_G$  on the x-axis and  $\theta_A$  on the y-axis) were allowed to vary from 0.2 to  $90^\circ$ . The  $\lambda/4$  case was not included because there was not a large, perceivable difference between the  $\lambda/4$  and  $\lambda/3$  plots. The deep red regions refer to high condition numbers (singularities), while the blue regions refer to low condition numbers. The difference in condition number between the blue regions of the two plots is approximately an order of magnitude. Once a retarder rotation ratio is settled upon, the optimum number of measurements to collect can be examined by holding  $\theta_G$  and  $\theta_A$ , as well as  $\delta_G$  and  $\delta_A$ , constant and allowing  $q$  to vary.

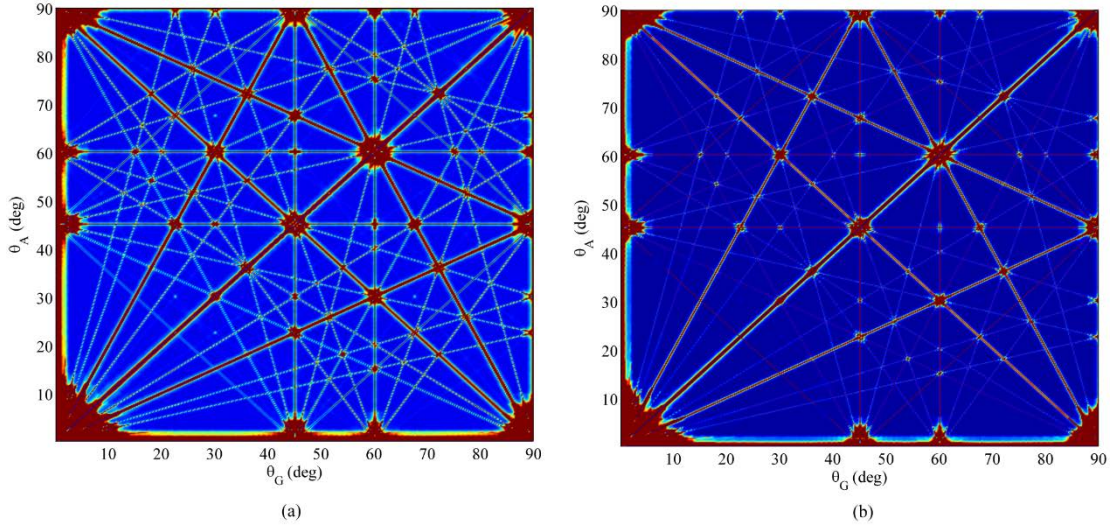


**Figure 4-1. Condition number plot for DRR under a 48-measurement collection configured with a  $\lambda/5$  (a) and  $\lambda/3$  (b) retarder. The x-axis refers to angular increments applied to the generator retarder, and the y-axis analyzer retarder increments.**

#### 4.3.4 Fourier Method

The constraints on the Fourier method are more stringent. It requires  $\lambda/4$  retarders, limits the retarder rotation ratio to  $5\omega:1\omega$ , and necessitates that the PSG retarder incurs a

half or full  $360^\circ$  rotation. The first limitation is relaxed with the assistance of Chenault's calibration technique [40], which allows the Fourier ratio to be extended to include the use of  $\lambda/3$  retarders and reach the optimal retardance for a DRR [42, 43].

The basis of the Fourier method for DRR operation refers back to Eqn. (4-2) and (4-3). The difference is now that the  $w$ -variable only takes on forms compatible with the  $5\omega:1\omega$  rotation ratio and a  $q$ -dimension that forces the first retarder to complete a half or full rotation cycle over the measurement process [40]. The uniqueness of this ratio is that the  $M_m$  is encoded on the Fourier coefficients of the measured intensity signal. Specifically, they are encoded on twelve harmonics contained in the measured signal. This allows the signal,  $I_q$ , to be specified as a Fourier series according to [40]

$$I_q = a_0 + \sum_{j=1}^{12} (a_j \cos(2j\theta_q) + b_j \sin(2j\theta_q)). \quad (4-8)$$

This leads to a set of equations where the  $M_m$  elements can be uniquely determined as a function of the Fourier coefficients [40, 46]. Corrections to the  $M_m$  elements are needed when systematic errors are present.

#### ***4.3.5 Calibration Method***

Chenault's calibration technique [40] was an extension of Goldstein's [39]. It relies on specifying retardance errors in the PSG ( $\delta_1$ ) and PSA retarders ( $\delta_2$ ), and alignment errors in the PSG ( $\epsilon_3$ ) and PSA retarders ( $\epsilon_4$ ) and analyzer ( $\epsilon_5$ ). The error terms can be found by conducting a free-space measurement. They are then used to correct systematic errors in succeeding measurements. The strength of this calibration method is in its span of corrections. It is capable of correcting measurements with retardance deviations within  $\lambda/8$  of the nominal  $\lambda/4$  and misalignments up to  $22.5^\circ$  [40].

When working with this calibration technique, the retardance and alignment errors were used to update the W-matrix used in the measurement matrix. This allowed the error of the free-space measurement to be tracked as a function of the intensity measurement. This type of analysis is not directly available to the Fourier method, since Mm results are only available at the conclusion of a full or half rotation of the PSG retarder. Updating the W-matrix with the values obtained from the calibration analysis can also be used to analyze non-Fourier rotation ratios tested. However, it is expected that some systematic error will remain unaccounted for due to the presence of beam wander. These effects are immune to the Fourier rotation ratios so long as a full  $360^\circ$  rotation of the PSG retarder is applied [40]. An update of the W-matrix using the retardance and alignment deviations found from the calibration measurement is used in the experimental analysis in Section 4.4.4 to track the Mm error measurement by measurement for the tested configurations.

#### **4.4 Error Analysis**

Conducting an error analysis on a particular DRR configuration is the most intuitive/effective way to determine its robustness against random errors. Condition number analysis is a good starting point. It provides a numerical result in the form of a condition number for a particular DRR setup. However, the correspondence between condition number and the error limitation of the chosen measurement parameters is not immediately clear. This makes it difficult to make an informed decision when selecting the retarder rotation ratio, retardances and the number of intensity measurements to collect.

Error analysis was performed by introducing random errors to numerically created ideal free-space intensity measurements. The deviation of the random error was kept constant while the parameters of the measurements were varied. By comparing the changing parameter values to the changing error in the resulting Mm's, it was possible to equate parameter selection to the error limitation of the system. The goal of this analysis was to determine the best retarder rotation ratio to use and identify the performance enhancement achieved by increasing the retardance.

#### ***4.4.1 Optimal Retarder Rotation Ratios***

With the retarder restrictions established ( $\lambda/5$ ,  $\lambda/4$  and  $\lambda/3$ ), condition number analysis was used to find the optimal retarder rotation ratios to consider. Once found, the ratios would be kept constant, while the retardance of the DRR configuration was varied. The already-determined optimal rotation ratio found for 16 measurement case, 34:26, [43] and two Fourier rotation ratios, 25:5 and 37.5:7.5, which were consistently found among the lowest condition numbers with condition number analysis were used in the optimization analysis. The condition number plots for each of the retardance cases are shown in Figure 4-2.

The condition number findings are significant. They showed drastic changes for the Fourier rotation ratios at the 17-measurement and 28-measurement marks for the 37.5:7.5 and 25:5 rotation ratios, respectively. The condition number performance for each of the Fourier rotation ratios quickly surpassed the 34:26 rotation ratio performance. Of additional interest is the convergence of the condition numbers of all three rotation ratios as the retardance is increased. This analysis alone suggests the rotation ratios might

be irrelevant for oversampling with  $\lambda/3$  retarders, but should definitely be considered, as should the number of measurements, when operating a DRR with  $\lambda/4$  or  $\lambda/5$  retarders.

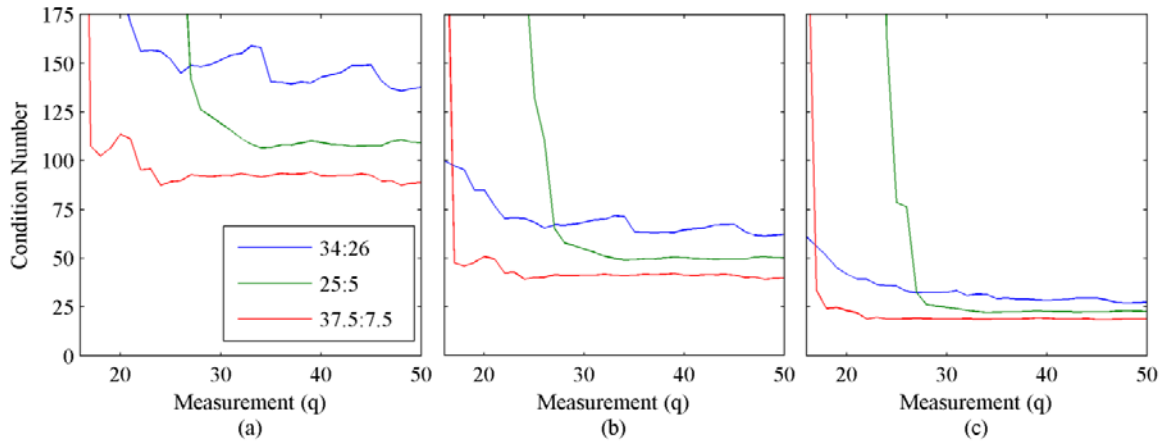


**Figure 4-2. Condition number plot for the retardance cases tested (a)  $\lambda/5$  (b)  $\lambda/4$  and (c)  $\lambda/3$  for the retarder rotation ratios 34:26, 37.5:7.5 and 25:5.**

#### ***4.4.2 Creating ideal, free-space intensity signals***

An ideal W-matrix (ideal polarizers, ideal retarders and perfect alignment) was created for each test case, and then multiplied by the identity matrix to obtain the ideal, free-space intensity signals. A snapshot of the free-space intensity signals for the 34:26, 25:5 and 37.5:7.5 retarder rotation ratios are shown in Figure 4-3, which show the expected intensity waveforms for the three retardance conditions. These waveforms were produced, so small, random errors could be introduced to them – to replicate the introduction of random errors in the experimental measurement process.

#### ***4.4.3 Introducing random noise***

All instruments suffer from the influences of random noise. In this case, the level of random noise can be tested by examining the differences in the intensity measurements from run to run. This was determined from a series of eight free-space measurements and the aid of the following equation

$$\text{Average Measured Intensity Error}(\%) = \frac{\sum_q \frac{I_{1,q} - I_{p,q}}{I_{1,q}}}{q} 100\%, \quad (4-9)$$

where  $q$  represents the intensity measurement number and  $p$  refers to the Mm measurement series. The first measurement ( $I_{1,q}$ ) was used as the reference measurement, from which average intensity deviations were determined from the seven measurements

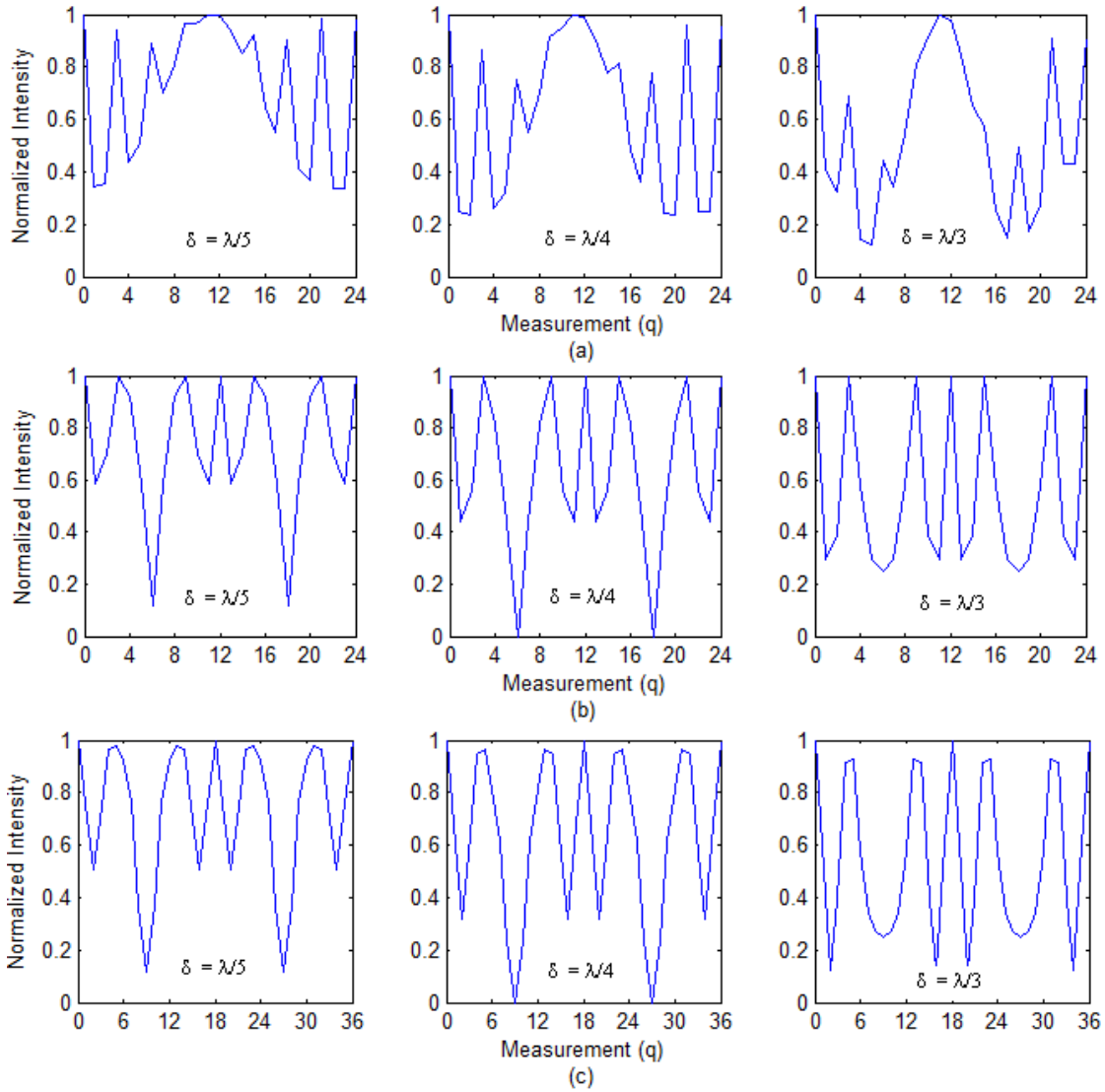


**Figure 4-3. Ideal free-space intensity signal under three different DRR retardance conditions ( $\lambda/5$ ,  $\lambda/4$  and  $\lambda/3$ ) when the retarders are rotated under a ratio of (a) 34:26, (b) 37.5:7.5 and (c) 25:5.**

that followed. The range of intensity deviations spanned 0.4% to 1.2%. A mid-range value of 0.8% random error in the intensity measurement was used for the analysis to remain in a representative range of the instrument.

The *random* function in MATLAB® allowed me to introduce random errors to the ideal, free-space intensity signals described in Section 4.4.2. The syntax for the random function is *random('distribution type', μ, σ, m, n)*, where μ represents the mean, σ represents the standard deviation, m is the row size, and n is the column size of the generated random error matrix. A *normal* distribution type was used. The mean (μ) was set to one. The standard deviation (σ) was set to 0.01 because it led to errors in the intensity signal that were consistent with the experimental set-up. Random errors were introduced to the ideal free-space intensity signal and then the level of error in the modeled intensity according to Eqn. (4-10). These operations were conducted 1,000 times and then averaged. The standard deviation value was adjusted until 0.8% was reached, replicating conditions similar to our experimental results.

$$\text{Average Modeled Intensity Error(\%)} = \frac{\left| \sum_{i=1}^q \frac{I_{Ideal,i} - I_{Idealw/noise,i}}{I_{Ideal,i}} \right|}{q} 100\% \quad (4-10)$$

To cast this analysis into a Mm error performance for each configuration and track it on a measurement-by-measurement basis, a Mm extraction was performed against the noisy intensity signal during each iteration of the loop. The error in the Mm extraction was determined during each loop iteration according to

$$Mm\ Error(\%) = \frac{\|M_{free-space} - M_{extracted}\|}{\|M_{free-space}\|} 100\%, \quad (4-11)$$

where the Mm for free-space was the identity matrix and the Mm for the measurement represents the extracted Mm during each loop iteration. The Mm error for all the 1,000 iterations was found at the conclusion of the loop and is represented in the final results plotted in Figure 4-4 for each of the tested configurations.

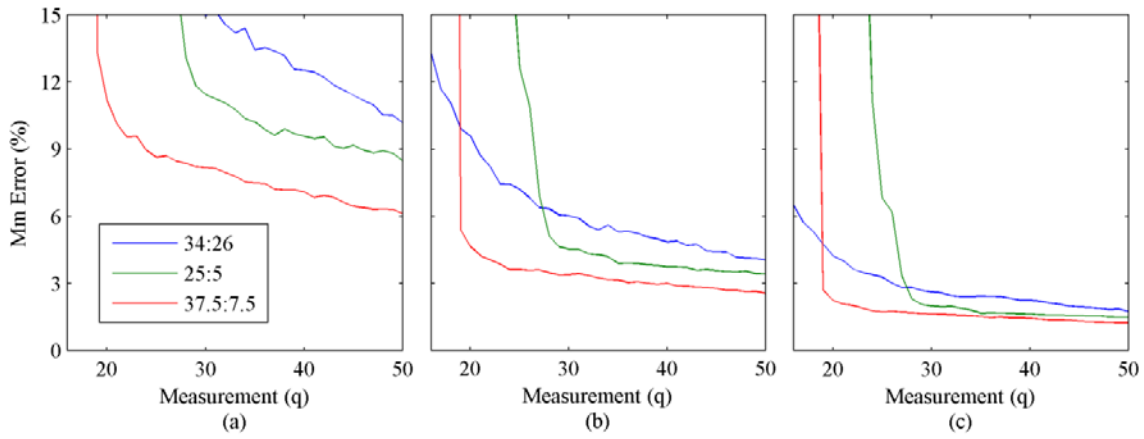


**Figure 4-4. Expected error in the free-space Mm extraction for the rotation ratios,  $\theta_A:\theta_G = 34:26$  (blue),  $25:5$  (green) and  $37.5:7.5$  (red) using the three retardance restrictions (a)  $\delta=\lambda/5$ , (b)  $\lambda/4$  and (c)  $\lambda/3$  and varying the number of intensity measurements (q) when additive random errors were introduced to ideal modeled intensity measurements for the DRR configuration represented.**

The error analysis findings were also significant. They illustrate behaviors similar to the condition number plots. The 37.5:7.5 Fourier rotation ratio performance exceeds the 34:26 optimal rotation ratio at the 19-measurement point, two measurements later than this occurred in the condition number plots. The 25:5 Fourier rotation ratio performance exceeds the 34:26 rotation ratio at 28 measurements, the same measurement point predicted by the condition number analysis. Trends with increasing measurement number are even more significant now, however. There are slopes in the Mm error plots,

despite plateaus reached in the condition number plots of Figure 4-2. This illustrates the need to perform measurements in excess of the number predicted from finding a stable condition number. Additionally, the slope of the Mm error plots diminishes with increasing retardance, with the overall minimum achievable error found in the  $\lambda/3$  retardance configuration and the 37.5:7.5 Fourier rotation ratio. This is not necessarily surprising, but what is strongly evident from this error analysis is that retardances less than the commonly used  $\lambda/4$  are increasingly susceptible to high errors in the Mm extractions despite applying optimized rotation ratios and increasing the number of intensity measurements. Thus, retardances less than  $\lambda/4$  should generally be avoided. Finally, the error performance of the  $\lambda/3$  retardance configuration generally improved by a factor of 2 over the  $\lambda/4$  retardance configuration.

#### ***4.4.4 Experimental Results***

With the DRR configured with  $\sim\lambda/3$  retarders (actually  $110^\circ$  at the  $5.0\mu\text{m}$  wavelength tested), two calibration measurements were made using the 25:5 and 37.5:7.5 rotation ratios. The systematic errors for the two measurements ( $\delta_1, \delta_2, \epsilon_3, \epsilon_4, \epsilon_5$ ) extracted from these measurements were in agreement with one another and were used to update the W-matrix for Mm extractions using the measurement matrix method. This technique permitted the Mm error for the three rotation configurations to be experimentally compared.

Five free-space Mm measurements were collected on each of the three rotation ratios (34:26, 25:5 and 37.7:7.5) following the calibration measurements described above. The intensity measurements were averaged, and the free-space Mm was extracted from

the averaged intensity measurement. The average errors were determined as a function of measurement number using the measurement matrix method with the updated W-matrix in order to compare experimental results with the modeled results. Each is shown in Figure 4-5, where the modeled results are represented by the solid curves and the experimental values by the line with the ‘o’ markers.

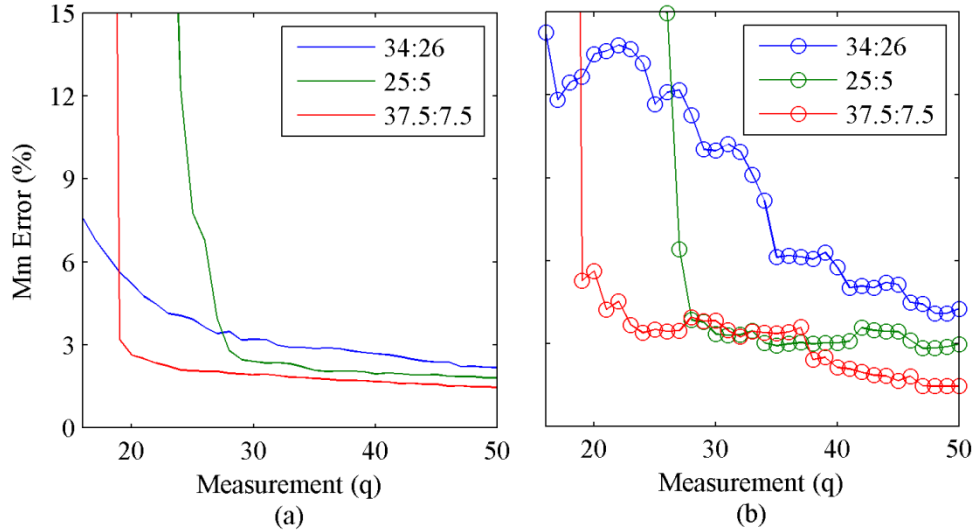


**Figure 4-5. Comparison of (a) modeled error in the free-space Mm extraction with the (b) experimental error for the instrument configured with  $\sim\lambda/3$  retarders in the DRR for three rotation ratio configurations ( $\theta_A:\theta_G = 34:26, 25:5$  and  $37.5:7.5$ ).**

Overall, the experimental and modeled 37.5:7.5 and 25:5 rotation-ratio results agree well, while the 34:26 rotation-ratio experimental results do not achieve as low of errors as predicted by the model. Intensity measurements in excess of 50 were collected. The reduction in error continued for the 34:26 case, reaching 3.3% by measurement 58. The 25:5 rotation ratio followed similar trends, where 1.1% error was achieved by measurement 73. As mentioned in Section 4.3.5, the non-Fourier rotation ratio could have systematic errors unaccounted for – due to beam wander. The Fourier rotation ratios remain immune to these effects because the PSG retarder was rotated a full  $360^\circ$  [40]

during the calibration measurement and succeeding free-space measurements. Despite the differences, it is clear that the 37.5:7.5 rotation configuration is the preferred measurement arrangement to minimize the error in the extraction and to minimize the number of measurements required to extract the Mueller matrix.

#### 4.5 Discussion

From the analysis steps used to develop a tunable IR Mm scatterometer, the two primary DRR measurement techniques were thoroughly reviewed along with the available calibration methodologies. Early experimental work showed that low retardance ( $\lambda/5$ ), low measurement numbers ( $q < 30$ ), the measurement matrix method of operation at  $\theta_G:\theta_A = 34:26$ , and the lack of a robust calibration technique led to large errors in free-space Mm extractions. These results led to the examination of condition number performance in greater detail and a method to translate condition number to a familiar figure (percentage of error in the free-space Mm extraction) was realized. This analysis was found to follow the condition number results when a random error on the order of 0.8% of the measured signal was applied to an ideal free-space intensity signal. The anticipated Mueller errors were 3%, 2% and 1.5% for a DRR with  $110^\circ$  retarders, 50 measurements collected, and retarder rotation conditions of 34:26, 25:5 and 37.5:7.5, respectively. Experimental results generally followed the analytical trends for the Fourier compatible rotations, but the experimental data from the 34:26 rotation configuration was found to be higher than the modeled predictions.

The use of  $\lambda/3$  retarders in the final design was a direct impact of the availability of a calibration technique capable of accommodating retardance deviations in excess of

30° [40], with the added benefit of optimizing the instrument and reducing the error in the Mm extractions. The Fourier rotation ratios were found to be a favorable configuration when performing condition number analysis of oversampled measurements. Each of these was considered a key finding of this work, and led to the successful development of a  $\sim\lambda/3$ -retardance-configured tunable IR Mm scatterometer.

#### 4.6 Conclusion

By evaluating the available range for Chenault's calibration technique [40], it was determined that a  $\lambda/3$  design was possible. By applying condition number analysis and random error analysis to free-space intensity signals represented by three different retardance configurations ( $\lambda/5$ ,  $\lambda/4$  and  $\lambda/3$ ) and three optimal rotation increments (34:26, 37.5:7.5, and 25:5), the Fourier method of DRR operations with  $\lambda/3$  retarders was determined to be the optimal DRR design configuration [28-30]. A tunable IR Mm polarimeter-scatterometer configured with an achromatic  $\sim\lambda/3$ -retardance-configured DRR was ultimately designed, which now achieves low-error free-space Mm extractions [30]. The completion of these optimization steps led to the development of the Mm polarimeter-scatterometer described in the next chapter.

## **V. DEVELOPMENT OF A TUNABLE MID-WAVE INFRARED MUELLER MATRIX POLARIMETER-SCATTEROMETER**

This chapter covers the development of the Mueller matrix (Mm) polarimeter-scatterometer, which was completed following the findings from the dual rotating retarder (DRR) optimization steps discussed in the previous chapter. The primary research steps covered in this chapter include: introducing tunable infrared (IR) external-cavity quantum cascade lasers (EC-QCLs) to an existing complete angle scatter instrument (CASI®); establishing retarder design criteria for the implementation of an achromatic dual rotating retarder (DRR) compatible with the EC-QCLs; confirming the operational performance of the instrument with free-space calibration runs; and collecting measurements on an IR metamaterial to validate the design intent. The results of this research are in draft form with a planned submission to *Review of Scientific Instruments* [31] and represents an instrument that is unique on a world-wide scale.

### **5.1 Executive Summary of Research**

Optical metamaterials often have narrow-band performance features. At infrared (IR) wavelengths, these features have only been observable with broad-band instruments at specular angles and under a limited polarimetric evaluation due to the constraints of existing instruments. A wavelength-tunable IR Mueller-matrix (Mm) polarimeter-scatterometer which can tune on and off of narrow-band regions of interest and perform a full polarimetric and directional evaluation of IR metamaterials was developed. The instrument is capable of performing these investigations at specular angles (acting as a

Mm polarimeter) and off-specular (acting as a Mm scatterometer), and opens the door to fully evaluating optical metamaterials at IR wavelengths.

## 5.2 Introduction

Theoretical predictions of optical metamaterials show that the effective material parameters of interest, typically electric permittivity and magnetic permeability, will often depend on the incident angle and polarization of the incident radiation [9]. Also, the attribution of optical phenomena observed or predicted for these materials, *e.g.*, to Bragg resonance as opposed to constitutive, homogeneous (effective) material parameters, based on inclusion size and periodicity may not be clear-cut [4, 8]. Finally, these optical phenomena, often based on Bragg or plasmonic resonances, are often narrow-band in nature [10, 11]. An instrument that is capable of measuring infrared (IR) metamaterial samples and providing a unique data set which, upon analysis, can lend significant insight into each of these issues [68, 69].

The narrow-band performance features of optical metamaterials are most readily found using a broadband instrument. A spectrometer can provide reflectance and transmittance data for samples at normal or fixed, specular incident angles. When increasing the measurement space to include polarization-sensitive measurements, a variable-angle spectroscopic ellipsometer (VASE) can provide these data at varying specular incident angles. The VASE can provide full, polarimetric analysis at visible and near infrared (NIR), but in the infrared (IR) the IR-VASE can only provide a limited polarimetric evaluation – it is capable of conducting co- and cross-polarization (ss, pp, sp, ps) measurements and partial Mueller-matrix (Mm) extractions. For full polarimetric

characterization of samples at IR wavelengths at both specular and off-specular angles (both in and out of the plane of incidence), an IR Mm polarimeter-scatterometer is needed. This type of instrument was developed by using tunable external-cavity quantum-cascade lasers (EC-QCLs), and it is now being used to evaluate the behavior of optical metamaterials.

Scatterometers were once restricted to a small number of fixed-IR-wavelength laser sources, but wavelength-tunable EC-QCLs have extended the range of wavelengths offered to polarimeters and scatterometers. A series of tunable Daylight Solutions® EC-QCLs were selected to span a nearly continuous range of mid-wave IR (MWIR, 4.37-6.54 $\mu\text{m}$ ) and long-wave IR (LWIR, 7.41-9.71 $\mu\text{m}$ ) wavelengths, which were added to the existing 3.39 $\mu\text{m}$  HeNe laser and 10.6 $\mu\text{m}$  CO<sub>2</sub> laser in a Schmitt Measurement Systems (SMS) Complete Angle Scatter Instrument (CASI®). Extensive hardware and software upgrades were also implemented to introduce an achromatic dual rotating retarder (DRR) polarimeter and accompanying rotation stages to the instrument. The end product is a tunable IR Mm polarimeter-scatterometer, which can be tuned into and out of narrow-band performance regions of optical metamaterials, allowing for the investigation of their full range of directional scalar and polarimetric behaviors.

## **5.3 Instrument**

### ***5.3.1 Physical Layout***

The CASI® already had an existing and suitable beam train for the introduction of the EC-QCLs. Slight modifications were made so the EC-QCLs could be introduced and easily aligned, which included the first turning mirror (TM) and beam combiner (BC)

shown schematically in Figure 5-1. The beam combiner was used to place a visible alignment source in the beam path, and the turning mirror was used to couple an EC-QCL into the beam path. More importantly, the turning mirror provides the means to bring the EC-QCL into co-alignment with the system following the visible source alignment.

The co-alignment process is facilitated by power adjustments to the EC-QCL. This allows thermal paper to be used to trace the IR beam through the system from source to the detector, which is shuttered until a proper power level is restored. The end result of the alignment process is the ability to visually verify the location of the IR source for sample placement on the goniometer, and it provides the ability to adjust/determine the rotational center of the sample after mounting it.

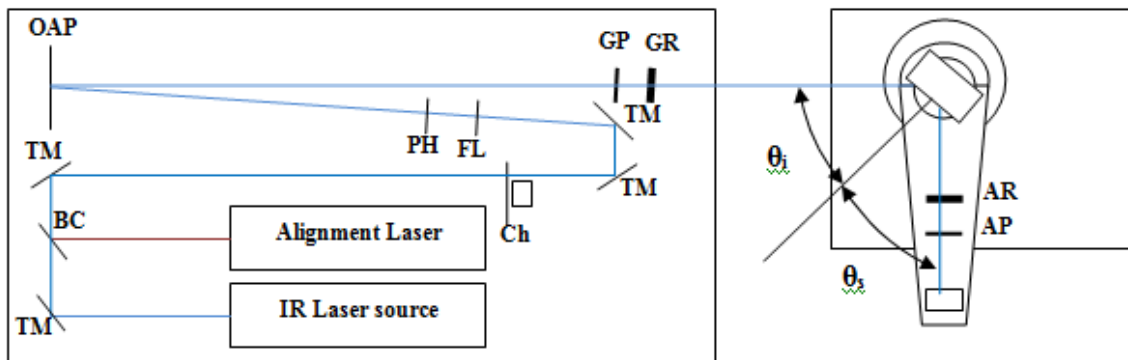


**Figure 5-1. Physical layout of the Mueller matrix scatterometer using the following labeling conventions: TM – turning mirror; BC – beam combiner; Ch – chopper; PH – pinhole; FL – focusing lens; OAP – off-axis parabolic mirror; GP – generator-stage polarizer; GR – generator-stage retarder; AR – analyzer-stage retarder; AP – analyzer-stage polarizer.**

### 5.3.2 EC-QCLs

A set of six EC-QCLs was selected to provide a continuous span of MWIR wavelengths from 4.37 to 6.54 $\mu\text{m}$  and LWIR wavelengths from 7.41 to 9.71 $\mu\text{m}$ . Table 5-1 shows the tunable range of each EC-QCL, their peak wavelengths and their peak

powers. Unlike gas lasers, the power of the EC-QCLs is adjustable, which is effective for alignment, overall improvement of signal detection and achieving the highest dynamic range of the instrument. The output powers of the 3.39 $\mu\text{m}$  HeNe and 10.6 $\mu\text{m}$  CO<sub>2</sub> lasers are 3.7mW and 14.6 W, respectively.

**Table 5-1. EC-QCLs selected for the Mm polarimeter-scatterometer**

EC-QCL wavelength range ( $\mu\text{m}$ )	Peak $\lambda$ ( $\mu\text{m}$ )	Peak Power (mW)
4.35-4.55	4.5	220
4.74-5.15	4.9	160
5.16-5.67	5.3	330
5.76-6.54	6.1	280
7.40-8.23	7.8	340
8.06-9.71	8.8	5

The wavelength tuning ranges of the sources were tested using a Bristol 721B spectrum analyzer and found to have excellent wavelength stability with bias. The sample set of results shown in Table 5-2 demonstrates that the tuned-to-measured wavelength deviation is correlated to the tuned wavelength rather than being strongly dependent on the applied bias current. In general, the EC-QCL wavelength is able to be set to six significant digits with relative uncertainty of less than 0.2%, and laser line-widths are less than 30MHz CW and 30 GHz pulsed.

**Table 5-2. EC-QCL wavelength stability performance under different bias conditions**

EC-QCL tuned wavelength ( $\mu\text{m}$ )	Measured wavelength ( $\mu\text{m}$ )	Deviation ( $\mu\text{m}$ )
5.76362 (500mA)	5.75113	0.01249
5.84300 (450mA)	5.83217	0.01083
6.08300 (400mA)	6.07669	0.00631
6.53586 (450mA)	6.53673	-0.00087
6.53586 (500mA)	6.53673	-0.00087

Automated wavelength tuning of the EC-QCLs is not a particular capability of the instrument at this time. Scatterometers require stringent alignment. The EC-QCLs grating-tune the wavelength, which creates enough beam walk that, when translated over the length of the optical path, adjustments to the alignment are required.

### ***5.3.3 Achromatic Dual Rotating Retarder Polarimeter***

The most complex element of this instrument is the achromatic dual rotating retarder (DRR). Extensive up-front analysis was conducted to determine the best retarder rotation configurations and the optimal retardance configuration [28-30], both of which leverage an existing calibration method [40]. Low-error, Mm extractions are only possible with a robust calibration methodology. It was concluded that the (5 $\omega$ :1 $\omega$ ) Fourier rotation scheme [41] was optimal by applying condition number and error analysis [30]. The Fourier rotation scheme traditionally uses  $\lambda/4$  retarders, but it was found that Chenault's calibration methodology [40] could also be used for the optimal  $\lambda/3$  retardance configuration [42, 43].

Achromatic, nominally  $\lambda/3$ , CdS/CdSe wave-plates were obtained from Gooch and Housego LLC for both the 4.3-6.5 $\mu\text{m}$  and 7.4-10.6 $\mu\text{m}$  wavebands. The predicted retardance for the waveplates is shown in Figure 5-2. Actual retardance values range from 109-116°. Four high-precision Aerotech, Inc. AGR-50 rotary stages were added and electronically integrated to the CASI instrument to achieve the DRR configuration. The AGR-50 has an internal 50:1 angular reduction ratio giving a calculated, repeatable step size of 0.016° when driven by a 0.8° increment stepper motor [68, 69]. This is well within the 0.3° accuracy recommended by Goldstein [46].

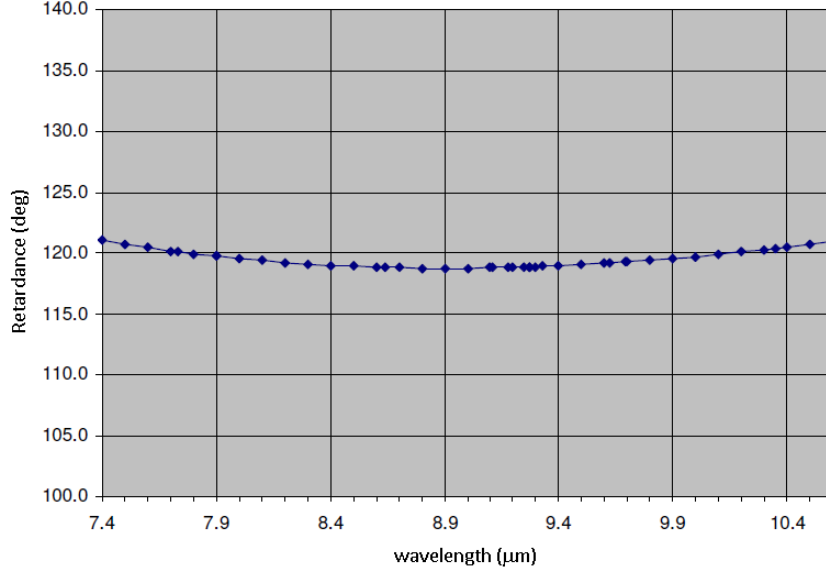


**Figure 5-2. Predicted retardance for the achromatic waveplate designed for 7.4-10.6μm. Similar retardance behavior is expected for the 4.3-6.5μm achromatic waveplates.**

Using the Fourier rotation schemes (25:5 and 37.5:7.5), free-space Mueller matrix extractions at 1% error or less are consistently achieved. An example free-space Mm extraction is

$$M_{free-space} = \begin{bmatrix} 1.0000 & 0.0010 & 0.0016 & -0.0019 \\ -0.0003 & 0.9978 & -0.0053 & 0.0012 \\ -0.0002 & 0.0065 & 0.9951 & 0.0010 \\ -0.0027 & -0.0016 & -0.0051 & 0.9969 \end{bmatrix}. \quad (5-1)$$

## 5.4 Mm Polarimeter-Scatterometer

Conversion of the commercial SMS CASI® into a Mm polarimeter-scatterometer included extensive hardware and software modifications. Electronic drivers for the Aerotech stages of the DRR were installed and interfaced with the existing instrument software. Software modifications were also made to produce a seamless transition from scalar directional scans to polarimetric scans [68, 69]. A method to operate the instrument

as a polarimeter by conducting Mm measurements of a sample at specular angles as the sample is rotated through a series of incident angles was implemented.

To illustrate the capabilities of the instrument, Mm results from a novel optical metamaterial, which is a spectrally, directionally and polarimetrically selective absorber [33], are shown with the instrument behaving as a Mm polarimeter and a Mm scatterometer. With the instrument tuned to 5.0 $\mu\text{m}$ , the impetus for building this instrument is clearly demonstrated – to investigate the polarimetric content of resonant and off-resonant narrow-band features of optical metamaterials at specular and off-specular angles of interest.

#### ***5.4.1 Mm Polarimeter Experimental Results***

The CASI® Mm polarimeter was first set to collect specular reflectance over a solid angle of 27msr<sup>-1</sup> (*i.e.* diameter aperture at 0.5 m distance) at incident angles 15-65°, with 1° increments collected near the resonant condition 20-30° and 5° increments outside this region. Figure 5-3 shows the Mm results in the traditional 4x4 Mm format but where each element is now a plot of the behavior of that element as a function of incident/reflectance angle. The  $m_{00}$  element shows the first measurement collected at each incident angle, and thus can generally be interpreted as a co-polarization (pp) Bi-Directional Reflectance Distribution Function (BRDF) value. In this case, the presence of a resonant feature in this optical metamaterials at 5 $\mu\text{m}$  and an incident angle of 25° is first observed in the  $m_{00}$  element. The resonant feature which is incident angle dependent in this material is clearly observed throughout the Mm elements and is only accessible with the wavelength tunability of this instrument.

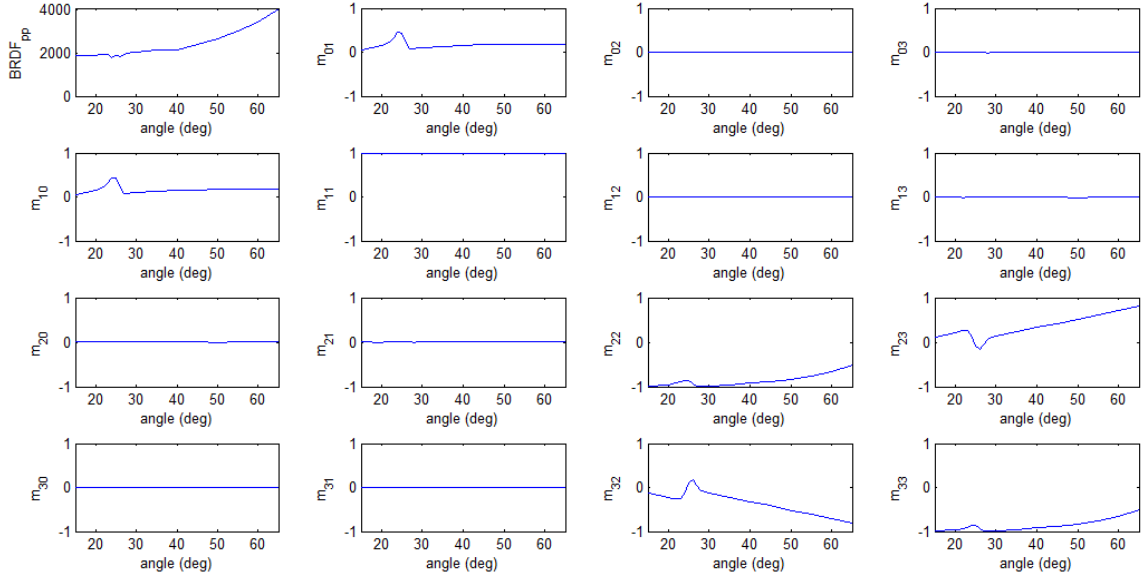


**Figure 5-3. Mm specular reflectance plot for a novel optical metamaterial sample [33] at 5.0 $\mu\text{m}$  when the instrument was operating as a Mm polarimeter. I.e. in specular mode such that the angles represent both incident and reflected angle.**

#### *5.4.2 Mm Scatterometer Experimental Results*

The same optical metamaterial [33] was examined with the CASI® Mm scatterometer set at incident angles of 25°, the resonant condition observed for this sample in Fig. 5-3, and at 60°, which represents an off-resonant condition. Figures 5-4 and 5-5 represent these measurements, respectively. As a scatterometer, the instrument collects Mm BRDF, so the angles shown for each Mueller element represent the in-plane reflectance angle for that particular incident angle. At the specular angle (represented by 0° in each of these figures), the same information shown in Figure 5-3 at 25° is shown again here. Away from specular, diffraction orders can be observed, indicating that this sample was fabricated in “tiles” approximately 140 $\mu\text{m}$  in size (the mask size of this particular electron-beam lithography process) and “tiled” together in a square lattice to form the larger sample. The polarization content of the light scattered by this sample is

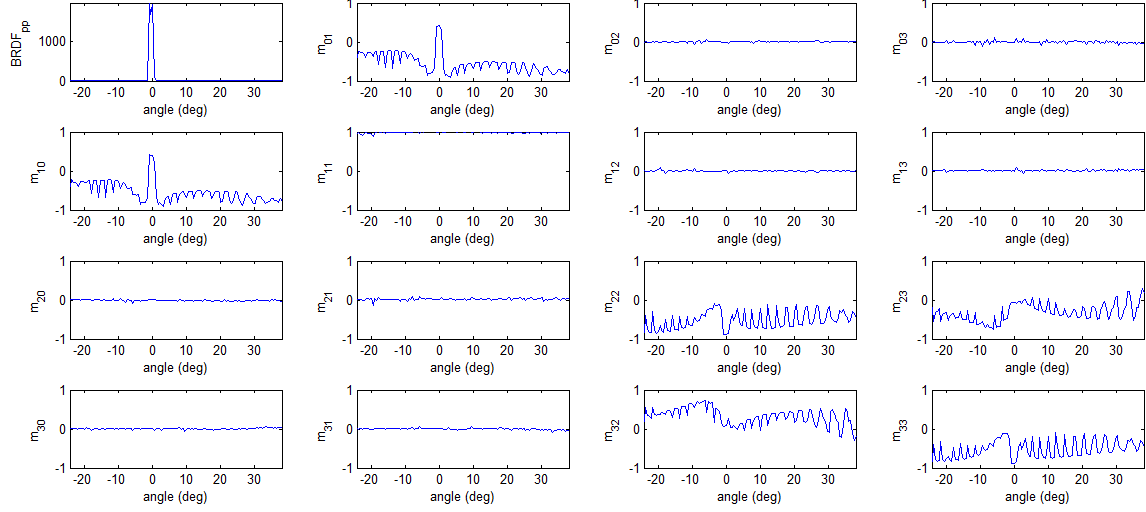


**Figure 5-4. Mm BRDF of a novel optical metamaterial sample [33] at 5.0  $\mu\text{m}$  and 25° incident angle. The resonant feature of Figure 5-3 is repeated here. The periodic structure is diffraction orders generated by the periodic nature of the sample.**

superimposed on this diffraction pattern. In Figure 5-5, the information in Figure 5-3 at 60° (where the resonant feature is absent) is again shown here at 0° (*i.e.* specular). Likewise, diffraction orders similar to those of Figure 5-4 and the superposition of polarimetric information on these orders are again observed here.

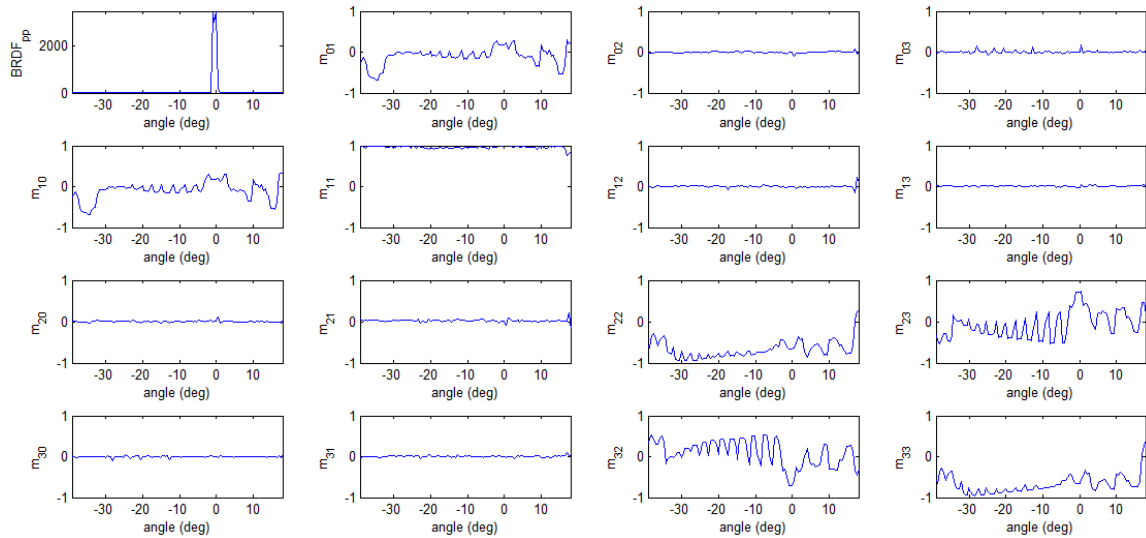


**Figure 5-5. Mm BRDF of a novel optical metamaterial sample [33] at 5.0  $\mu\text{m}$  and 60° incident angle, illustrating the off-resonant condition. The diffraction orders seen in Figure 5-4 are again found here.**

## 5.5 Discussion and Conclusion

Analyses of directional and polarimetric characteristics of narrow-band features found among optical metamaterials at IR wavelengths have been limited by limited data observable through the use of broad-band instruments only at specular angles and under limited polarimetric conditions. With the introduction of the tunable IR Mm polarimeter-scatterometer, narrow-band features found among optical metamaterials can be more fully explored, both at specular and off-specular (both in and out of the plane of incidence). Significant up-front analysis allowed this instrument to be designed and built in the optimal DRR configuration, which was discussed in the previous chapter [28-30]. The free-space results shown in this chapter demonstrate terrific calibration performance. The example results for an optical metamaterial sample illustrated the ability of this instrument to provide unique spectral, polarimetric and directional information on these samples.

This instrument was developed to deliver an unmatched ability to collect and analyze the behavior of IR optical metamaterials. This chapter demonstrated the collection abilities of the instrument. The analytical techniques to apply to the measured results are the focus of the next chapter.

## VI. EVALUATION OF A NOVEL OPTICAL METAMATERIAL ABSORBER

This chapter covers the novel measurements collected on an infrared (IR) metamaterial absorber (MMA) [33], using the tunable IR Mueller matrix (Mm) polarimeter-scatterometer described in Chapter 5. Modeling and subsequent polarimetric analysis was performed on the Mm extracted for the MMA. The findings from these analyses are covered in this chapter and demonstrate original, unpublished work with a planned submission to *Applied Physics Letters*.

### 6.1 Executive Summary of Research

Resonant MMAs are of interest for their selective impedance matching abilities to free-space. The periodic surface structures and non-transmissive backplane, which are separated by a dielectric layer, are responsible for their novel resonant absorbing characteristics [17]. While these resonances are designed features, surface wave resonances have also been found in these structures outside of the intended design regions. These resonances can have incident angle and polarization dependencies, which are observable with complete polarimeters where their polarimetric behaviors are captured in the form of a Mueller matrix (Mm). When in this form, example polarimetric behavior of the material can be examined with the introduction of Stokes-defined polarization states for either a Stokes vector analysis or a Poincaré sphere representation of the reflected state(s) – each was conducted as a part of this research. Mm modeling is also available and can be used to extract polarization-relevant information which is responsible for unique polarization signatures.

The Mm model of a Fresnel reflector having a complex refractive index is well-known [37], and manifests a unique Mm signature consisting of polarization magnitude and retardance features. They resemble polarizer-like features in the Mm elements,  $m_{00}$ ,  $m_{01}$ ,  $m_{10}$  and  $m_{11}$ , and retardance features in the Mm elements,  $m_{22}$ ,  $m_{23}$ ,  $m_{32}$  and  $m_{33}$ . The Mm extracted for the MMA was found to follow these characteristics, had low depolarization and a distinct polarization resonance. The resonant feature was found not to follow basic Fresnel reflectance models, even when modeling constraints were relaxed to uniaxial anisotropy ( $n_x = n_y \neq n_z$ ) and biaxial anisotropy ( $n_x \neq n_y \neq n_z$ ) conditions. The extracted reflectance magnitude and phase behavior is real; however, the MMA does not behave as an effective medium.

## 6.2 Introduction

A resonant, spectrally selective MMA was studied [33]. To examine polarization spectral and incident angle dependencies, a broad-band infrared variable angle spectroscopic ellipsometer (IR-VASE) was first used to collect p-polarization (p-pol) and s-polarization (s-pol) reflectance spectra. The MMA was designed to resonantly absorb optical radiation in regions centered around  $\sim 6.3 \mu\text{m}$  and  $\sim 8.2 \mu\text{m}$ . These resonant absorption valleys were reconfirmed, but a strong, surface plasmon polariton (SPP) resonance intersecting  $5.0 \mu\text{m}$  and  $25^\circ$  incident angle was also observed. To the best of my knowledge, a full polarimetric evaluation of an SPP mode remains unreported at this time.

The Mm polarimeter [31] was tuned to  $5.0 \mu\text{m}$  for the collection of the Mm of this sample. The collected Mm was first confirmed physically realizable. Then, it was

analyzed according to a Mm reflectance model, where the behavior of the reflectances ( $R_s$  and  $R_p$ ) as well as the phase behavior between the s-pol and p-pol states is determined. From these extractions, it remains convincing that effective complex refractive index values for this material are not expected. Although the extracted Mm shows evidence of Fresnel reflectance behavior of a material having a complex refractive index for the s-pol reflectance ( $R_s$ ), it remains clear that the periodic nature of the material produces resonant reflectance magnitude and phase characteristics which are not reproducible even when the model is relaxed to biaxial conditions. Following the Fresnel analysis, example behaviors of the sample against canonical polarization states (linear horizontal, linear  $45^\circ$  and right hand circular) are reviewed. The chapter closes with the ellipticity ( $\chi$ ) and orientation ( $\psi$ ) calculations of the reflected polarization states (linear  $+45$  and right hand circular) for a Poincaré sphere interpretation.

### **6.3 IR VASE Measurements**

With the IR-VASE, both p-pol and s-pol measurements can be collected for a sample over a range of incident angles from  $25^\circ$  to near grazing. Complex refractive index data can be retrieved for layered samples, when the thicknesses of the individual layers are known. Similarly, the material thicknesses can be determined in the instance the complex refractive index data of the sample is known [70]. Neither of these options remains available for non-homogeneous materials because well-known models linking the structure of the sample to the complex reflectance spectra do not exist [70]. Thus, this instrument was leveraged in this research to find a polarimetric region of interest, where

the Mm polarimeter could be used to recover the full-polarimetric details of a metamaterial sample.

An SPP mode centered at  $5.0\mu\text{m}$  and  $25^\circ$  incident angle was found for the novel MMA sample [33]. The IR-VASE p-pol and s-pol spectra are shown in Figure 6-1, where the p-pol spectrum is on the left and s-pol spectrum is on the right. The measurement angles span those which are observable with the Mm polarimeter, with the exception of the lower incident angle. The IR-VASE can only reach  $25^\circ$ , but the Mm polarimeter can reach  $15^\circ$ . Thus, the polarimetric state of the sample could be observed with the Mm polarimeter for incident angles  $15$ - $25^\circ$ , near the SPP mode at  $25^\circ$  and at angles greater than  $25^\circ$ .

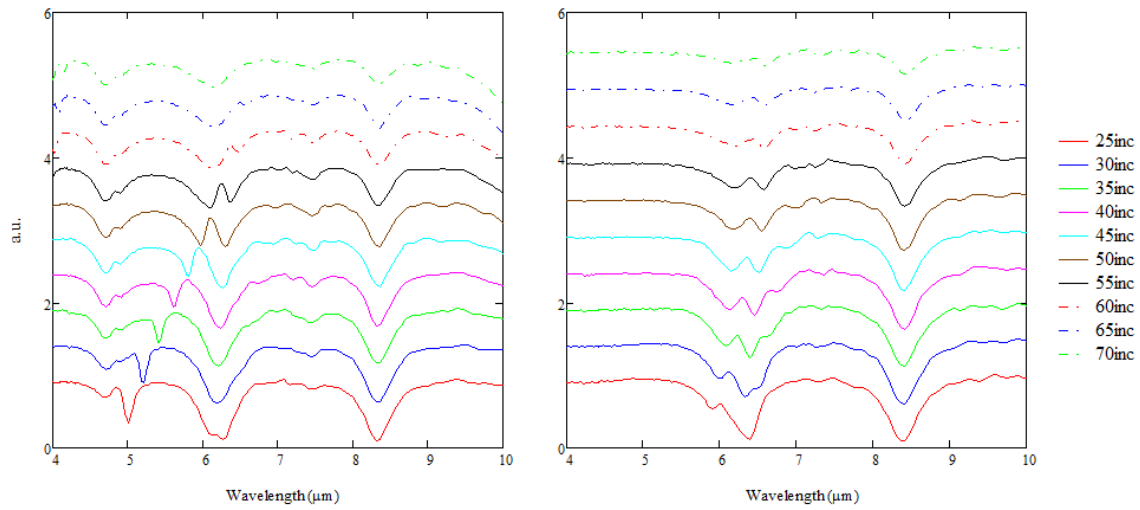


**Figure 6-1. (left) P-pol and (right) s-pol reflectance measurements taken of the MMA with increasing incident angle using the IR-VASE**

The IR-VASE measurements show two absorption resonances which are stationary with respect to incident angle at  $\sim 6.3\mu\text{m}$  and  $\sim 8.2\mu\text{m}$ , and two resonances whose resonant wavelengths are incident angle dependent. The mechanism responsible for the incident angle dependent absorption resonance in the s-pol spectra remains

undetermined at this time. The absorption resonance in the p-pol plot is due to an SPP mode, which can be found from solving

$$\bar{k}_{SPP} = \bar{k}_x \pm j\bar{g}_x, \quad (6-1)$$

where  $k_x$  refers to the in-plane propagation vector ( $|\bar{k}_x| = k_0 \sin(\theta_i)$ ), with  $k_0$  referring to the free-space propagation constant, and  $\bar{g}_x$  refers to the grating vector ( $|\bar{g}_x| = 2\pi / a$ , with  $a$  referring to the periodic spacing between the surface features) [71, 72]. The mode order is specified by  $j$ . The first order ( $j = 1$ ) SPP resonance is encountered when Eqn. (6-1) is satisfied and can be rewritten as

$$\frac{2\pi\tilde{n}_{SPP}}{\lambda_0} = \frac{2\pi}{\lambda_0} \sin \theta_i \pm \frac{2\pi}{a}. \quad (6-2)$$

This equation is solved for  $\lambda_0$  and plotted as a function of incident angle in Figure 6-2 to show the incident angle behavior of the predicted SPP resonance. The material properties in  $\tilde{n}_{SPP}$  for the MMA (Au and the dielectric spacer) were specified at  $5.0\mu\text{m}$  [71, 72].

$$\tilde{n}_{SPP} = \sqrt{\frac{\epsilon_{Au}\epsilon_{spacer}}{\epsilon_{Au} + \epsilon_{spacer}}} \quad (6-3)$$

The periodic spacing was  $a = 3.2\mu\text{m}$ . An expected SPP resonance was found at  $5.2\mu\text{m}$  at a  $25^\circ$  incident angle, which is close to the experimentally observed resonance occurring at  $5.0\mu\text{m}$  and  $25^\circ$ .

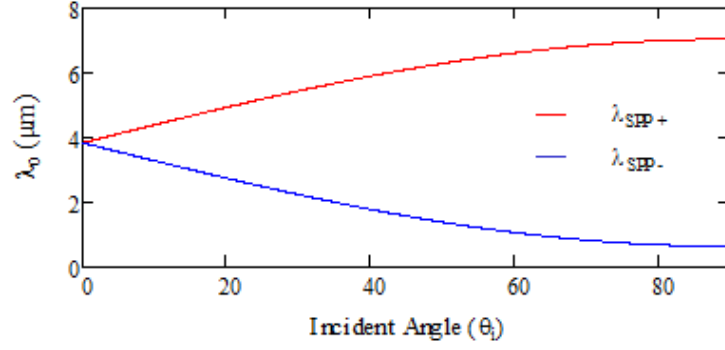


**Figure 6-2.** Surface plasmon polariton resonance calculated for the MMA, using the material properties of Au at 5.0μm ( $\tilde{n} = 3.7 + i30.5$ ) [34] and the dielectric ( $\tilde{n} = 2.06 + i0.12$ ) [17], while the periodic spacing  $a = 3.2\mu\text{m}$ .

#### 6.4 Mm Polarimeter Measurements

The Mm polarimeter was configured to collect specular reflectance measurements at 5.0μm for incident angles from 15 to 65°. Increments of 1° were used from 20 to 30° and increments of 5° were used outside of the resonant feature. Figure 6-3 shows the extracted specular reflectance Mm for the MMA. There is clear evidence of the SPP resonance, peaking in the vicinity of 25°.

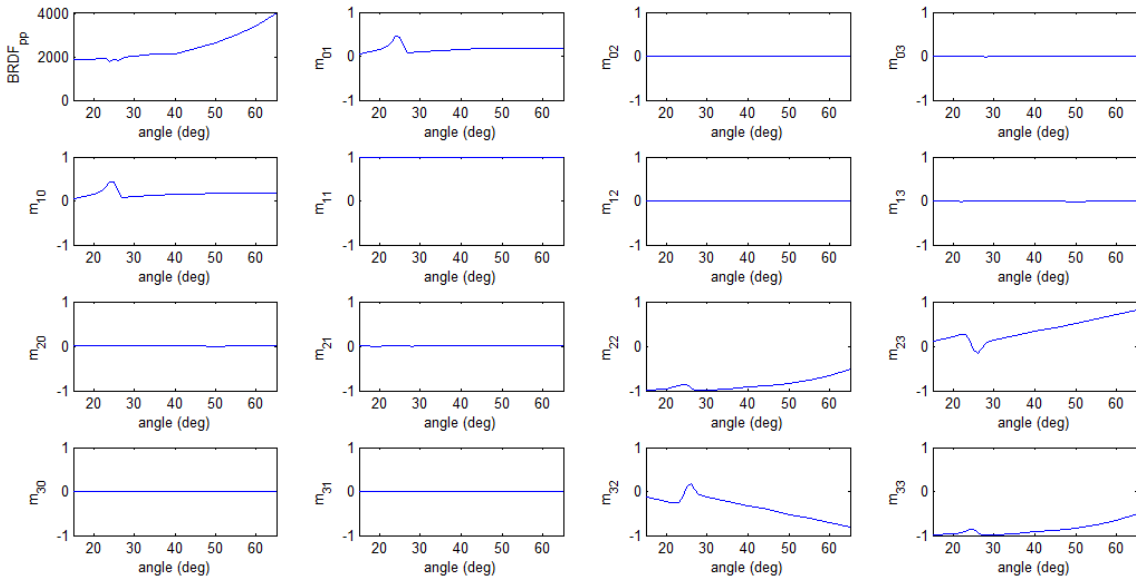


**Figure 6-3.** Normalized specular reflectance Mm plot for the MMA at 5.0μm.

The behavior of the  $M_m$  illustrates both polarizer and retarder tendencies, where the polarizer tendencies are found in the  $m_{00}$ ,  $m_{01}$ ,  $m_{10}$  and  $m_{10}$  terms, and the retarder tendencies are found in the  $m_{22}$ ,  $m_{23}$ ,  $m_{32}$  and  $m_{32}$  terms.

### 6.5 Determining the $M_m$ is physically realizable

Before performing modeling analysis with the extracted specular reflectance  $M_m$  for the MMA sample, it had to first be determined physically realizable. The trace of the  $M_m$  multiplied by its transpose must adhere to following inequality [46].

$$Tr(\mathbf{M}\mathbf{M}^T) = \sum_{i,j=0}^3 m_{ij}^2 \leq 4m_{00}^2, \quad (6-4)$$

where  $\mathbf{M}$  refers to the extracted  $M_m$  of the sample and  $\mathbf{M}^T$  is its transpose. The equality applies to a non-depolarizing sample, while the inequality infers the presence of depolarization. Verifying this equality ensures the degree of polarization requirement of the outgoing Stokes vector is met, where the degree of polarization of a Stokes vector is [46]

$$DOP = \frac{\sqrt{S_1^2 + S_2^2 + S_3^2}}{S_0} \leq 1. \quad (6-5)$$

The extracted  $M_m$  for the MMA was found to be physically realizable, with only minor depolarization, which was primarily present at the resonant peak. This is shown in Figure 6-4. The values outside of the resonance were 0.98 to 0.99 and the lowest value in the resonant region was 0.96. Overall, the sample was found to be very polarization preserving and its  $M_m$  physically realizable.

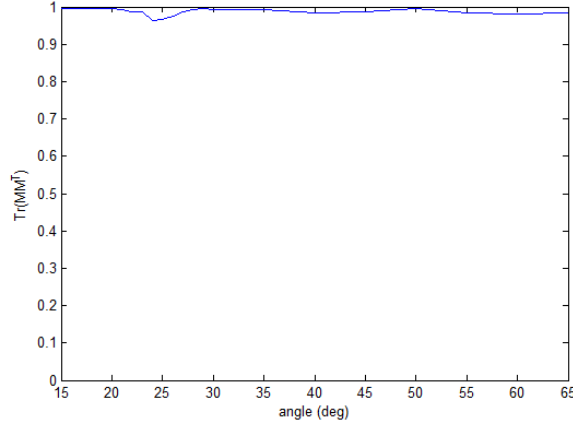


**Figure 6-4. The trace of  $MM^T$  for the extracted specular reflectance  $M_m$  for the MMA at  $5.0\mu m$ .**

### 6.6 Mm Reflectance Model

A Mm reflectance model exists [38] and can be used to describe the Mm behavior of materials having a complex refractive index with the aid of the a Fresnel reflectance equations. This model was used to confirm the Mm behavior of a gold mirror during the early experimental work with the Mm polarimeter – the results of which can be found in Appendix B and yielded great agreement with the model despite the measurements being performed in a wavelength region ( $3.39\mu m$  and  $5.0\mu m$ ) where gold has a diminishing polarimetric signature (at infrared wavelengths metals begin to behave as perfect reflectors across nearly all incident angles). The model remains valid for materials having only a real component to their refractive index (*i.e.* lossless dielectrics); it just becomes simplified. Furthermore, the model remains valid when the material is not a Fresnel reflector – it can be reconstructed if the s-pol and p-pol reflectances and their phase difference ( $\delta_p - \delta_s$ ) are known.

A Mm reflectance model is investigated here to understand the polarimetric behavior of the MMA. What will be seen in this section is that two sets of modeling

considerations must be examined to extract information from the measured Mm, that is, the un-normalized Mm (raw measurements which are in a Fourier described BRDF space) and the normalized Mm, for which results are cast into Mueller space having a range from -1 to +1.

### 6.6.1 Un-normalized Mm Reflectance Model

The un-normalized Mm of a general reflector has the following form [38]

$$M_R = \frac{1}{2} \begin{bmatrix} R_s + R_p & R_s - R_p & 0 & 0 \\ R_s - R_p & R_s + R_p & 0 & 0 \\ 0 & 0 & -2\sqrt{R_s R_p} \cos(\delta_p - \delta_s) & -2\sqrt{R_s R_p} \sin(\delta_p - \delta_s) \\ 0 & 0 & 2\sqrt{R_s R_p} \sin(\delta_p - \delta_s) & -2\sqrt{R_s R_p} \cos(\delta_p - \delta_s) \end{bmatrix}. \quad (6-6)$$

where  $R_s$  and  $R_p$  can refer to the Fresnel reflectances for s-pol and p-pol light, and  $\delta_s$  and  $\delta_p$  refer to the phases gained upon reflection for the s-pol and p-pol light, which come from the following Fresnel amplitude equations [70].

$$r_s = \frac{n_0 \cos(\theta_i) - \tilde{n} \sqrt{1 - \left( \frac{n_0 \sin(\theta_i)}{\tilde{n}} \right)^2}}{n_0 \cos(\theta_i) + \tilde{n} \sqrt{1 - \left( \frac{n_0 \sin(\theta_i)}{\tilde{n}} \right)^2}} = |r_s| e^{-i\delta_s} \quad (6-7)$$

$$r_p = \frac{n_0 \sqrt{1 - \left( \frac{n_0 \sin(\theta_i)}{\tilde{n}} \right)^2} - \tilde{n} \cos(\theta_i)}{n_0 \sqrt{1 - \left( \frac{n_0 \sin(\theta_i)}{\tilde{n}} \right)^2} + \tilde{n} \cos(\theta_i)} = |r_p| e^{-i\delta_p} \quad (6-8)$$

It is here that we see if a complex refractive index ( $\tilde{n} = n - ik$ ) exists, there will be a unique phase for both the s-pol and p-pol light, whose effects will show up in the  $m_{22}$ ,  $m_{23}$ ,  $m_{32}$  and  $m_{33}$  terms. In the instance the refractive index is purely real (*i.e.* dielectric,  $\tilde{n} = n$ ) and under external reflection, the phase difference between the s-pol and p-pol reflectances are  $0^\circ$  or  $180^\circ$ . In this case, the  $m_{23}$  and  $m_{32}$  terms evaluate to zero, and the

Mm takes on the form of a polarizer [46]. On a final note, the Fresnel intensity reflectances ( $R_s$  and  $R_p$ ) can be found from

$$R_s = |r_s|^2 \quad (6-9)$$

and

$$R_p = |r_p|^2. \quad (6-10)$$

From this model, the following relationships among the elements of the un-normalized Mm can be used to obtain the behavior of the s-pol and p-pol reflectances.

$$R_s = m_{11} - m_{01} \quad (6-11)$$

$$R_p = m_{01} - m_{11} \quad (6-12)$$

These reflectances were extracted from the measured data and then scaled to agree with the  $25^\circ$  reflectance data collected from the IR-VASE measurements. Great agreement between the two sets of results can be seen in Figure 6-5. Scaling was required because this data was in BRDF space ( $\text{sr}^{-1}$ ), and the polarimetric measurements were collected with an over-sized aperture since rotating optical elements are in the beam train. In short, this means direct access to the  $R_s$  and  $R_p$  measurements are not available but the overall

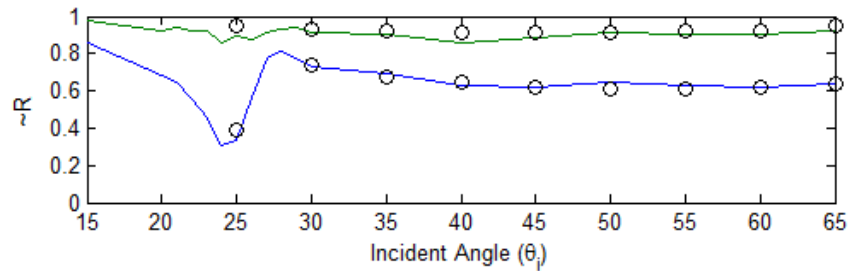


**Figure 6-5.  $R_s$  (green) and  $R_p$  (blue) reflectance behaviors determined from un-normalized Mm data for the MMA at  $5.0\mu\text{m}$ . Markers represent reflectance data from the IR-VASE measurement.**

behavior can be. What is immediately evident is that the  $R_p$  behavior is not indicative of an *effective* complex refractive index for an isotropic material. Later it will be shown that the  $R_s$  behavior generally follows the behavior of gold at infrared wavelengths.

### 6.6.2 Normalized Mm Reflectance Model

Since the measurements were collected in BRDF space, the Mm requires normalization. This is facilitated by dividing all the Mm elements by the measured  $m_{00}$  or  $m_{11}$  term, which are identical. This scales the Mm to values relevant to Mm's (-1 to +1). It is the normalized form of the Mm that is reported in literature and is the form of the Mm reported in Figure 6-3 for the MMA. Note the form of  $m_{00}$  has been changed in the representation of Figure 6-3 (it is the  $BRDF_{pp}$ ). The normalized Mm reflectance model is of the following form.

$$M_{R\_nmeas} = \begin{bmatrix} \frac{R_s + R_p}{R_s + R_p} & \frac{R_s - R_p}{R_s + R_p} & 0 & 0 \\ \frac{R_s - R_p}{R_s + R_p} & \frac{R_s + R_p}{R_s + R_p} & 0 & 0 \\ 0 & 0 & \frac{-2\sqrt{R_s R_p} \cos(\delta_p - \delta_s)}{R_s + R_p} & \frac{-2\sqrt{R_s R_p} \sin(\delta_p - \delta_s)}{R_s + R_p} \\ 0 & 0 & \frac{2\sqrt{R_s R_p} \sin(\delta_p - \delta_s)}{R_s + R_p} & \frac{-2\sqrt{R_s R_p} \cos(\delta_p - \delta_s)}{R_s + R_p} \end{bmatrix}. \quad (6-13)$$

When normalized, direct access to the  $R_s$  and  $R_p$  is no longer available; however, a ratio of the reflectances can be established from a series of operations performed with the Mm elements.

$$m_{00\_nmeas} + m_{01\_nmeas} = \frac{2R_s}{R_s + R_p} \quad (6-14)$$

$$m_{00\_nmeas} - m_{01\_nmeas} = \frac{2R_p}{R_s + R_p} \quad (6-15)$$

$$\frac{m_{00\_nmeas} - m_{01\_nmeas}}{m_{00\_nmeas} + m_{01\_nmeas}} = \frac{R_p}{R_s} \quad (6-16)$$

Eqn. (6-16) is plotted in Figure 6-6 (top plot) and could be used in an attempt to find the complex refractive index of the MMA if the functional form of the reflectances is known.

Also shown in Figure 6-6 is the phase difference between the p-pol and s-pol states. This can be found from using either the un-normalized or the normalized Mm according to,

$$\delta_p - \delta_s = \tan^{-1} \left( \frac{m_{23}}{m_{22}} \right). \quad (6-17)$$

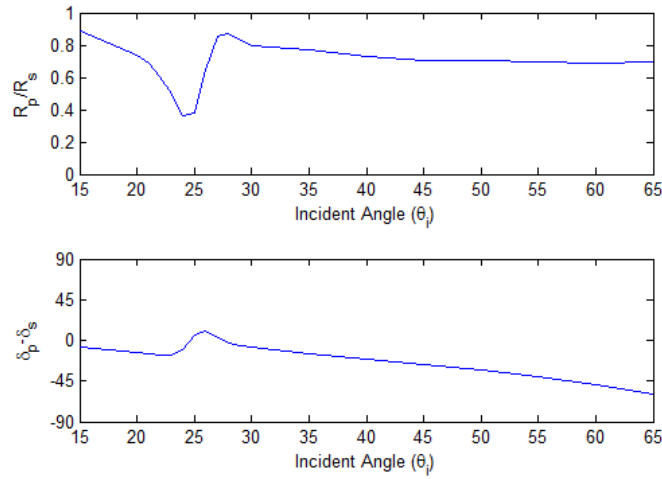


**Figure 6-6. Ratio of the reflectances (top) and phase difference between the p-pol and s-pol reflectances (bottom).**

### 6.6.3 Fresnel Reflectance Comparisons

Qualitative comparisons between three Fresnel reflectance models (isotropic, uniaxial anisotropic, or biaxial anisotropic) are made here to investigate the polarimetric behavior of the MMA, in particular, the exotic  $R_p$  behavior.

**Isotropic:** Example Fresnel reflectance and phase behavior of gold (the patterned metal on the surface of the MMA) is shown in Figure 6-7 for two different wavelengths ( $0.2\mu\text{m}$  and  $5.0\mu\text{m}$ ). These two wavelengths were selected to show the disparity in the character of gold in the ultraviolet (near its plasma frequency) and at the wavelength at which the MMA sample was examined. In each case, it can be seen that a loss index ( $\kappa$ ) prevents the  $R_p$  curve from reducing to zero (*i.e.* there is no Brewster angle for a material having a complex refractive index) but there is a general Fresnel reflectance character to each of the polarization states. What can also be seen is that a large loss index encourages high reflectivity from both the s-pol and p-pol states and diminishes the discrimination between them (until high incident angles are reached). This material property also leads to a lack of phase discrimination between the two polarization states. The phase behavior generally follows the discrimination between of the two polarization states. The  $R_s$  reflectance curve of the MMA looks similar to the  $R_s$  reflectance curve for gold at infrared frequencies. However, the  $R_p$  Fresnel reflectance curve does not follow the behavior of gold in the infrared. Overall, it can be expected that an isotropic model will not predict the MMA's  $R_p$  behavior.

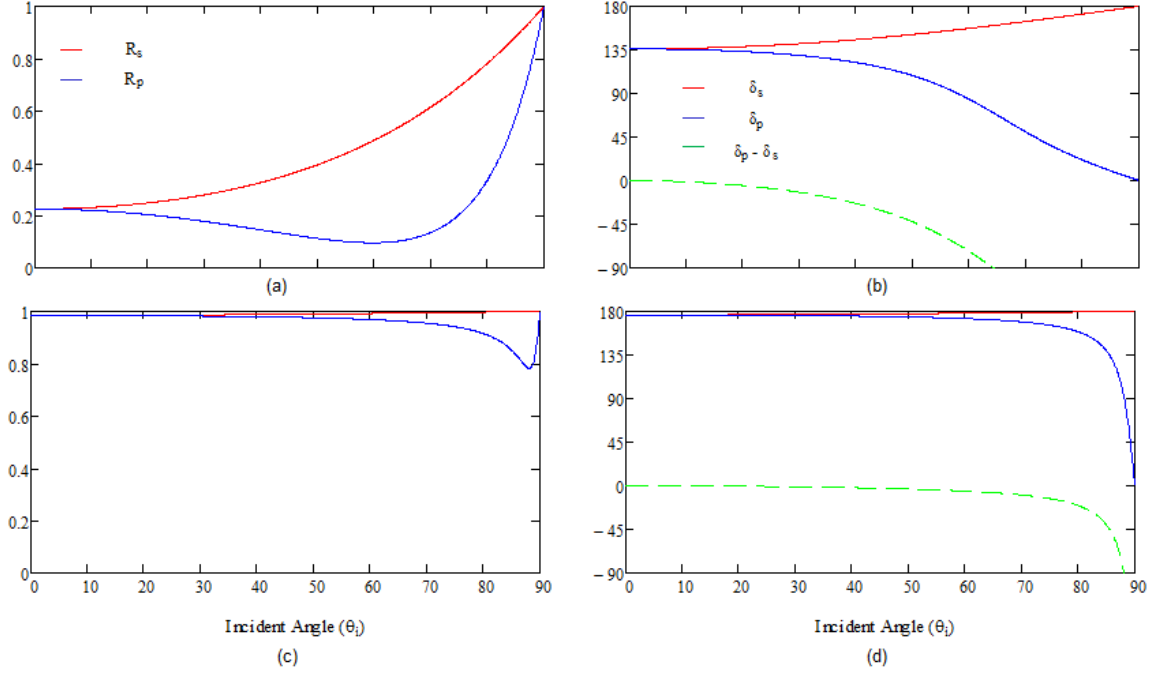


**Figure 6-7. Modeled Fresnel reflectance and phase curves for gold (surface material of MMA) at  $0.2\mu\text{m}$  (a) and (b) ( $\tilde{n} = 1.427 + i1.215$ ) and  $5.0\mu\text{m}$  (c) and (d) ( $\tilde{n} = 3.7 + i30.5$ ).**

**Uniaxial anisotropic:** The isotropic comparisons/findings are not surprising. Many metamaterials are considered anisotropic, since they often do not meet the unit cell or inclusion constraints that would allow an effective media description at their design wavelength [4]. The amplitude Fresnel reflectance equations for uniaxial anisotropic materials are [70] when  $\tilde{n}_x = \tilde{n}_y$

$$r_{s\_anisotropic} = \frac{\cos(\theta_i) - \sqrt{\tilde{n}_y^2 - \sin^2(\theta_i)}}{\cos(\theta_i) + \sqrt{\tilde{n}_y^2 - \sin^2(\theta_i)}} \quad (6-18)$$

and

$$r_{p\_anisotropic} = \frac{\tilde{n}_x \tilde{n}_z \cos(\theta_i) - \sqrt{\tilde{n}_z^2 - \sin^2(\theta_i)}}{\tilde{n}_x \tilde{n}_z \cos(\theta_i) + \sqrt{\tilde{n}_z^2 - \sin^2(\theta_i)}}. \quad (6-19)$$

For the uniaxial case,  $\tilde{n}_x$  is assumed to be equal to  $\tilde{n}_y$ , while  $\tilde{n}_z$  is allowed to vary according to the resonant design. Exotic behaviors can be seen when a large variation in  $\tilde{n}_z$  is available (but may not be physically realizable). Figure 6-8 illustrates example findings. The complex refractive indexes for  $n_x$  and  $n_y$  were held constant at values representative of gold at 5.0  $\mu\text{m}$  ( $n = 3.7$ ,  $\kappa = 20.5$ ), while values for  $\tilde{n}_z$  were tested for resonant behavior. Behavior similar to the MMA's  $R_p$  could not be replicated.

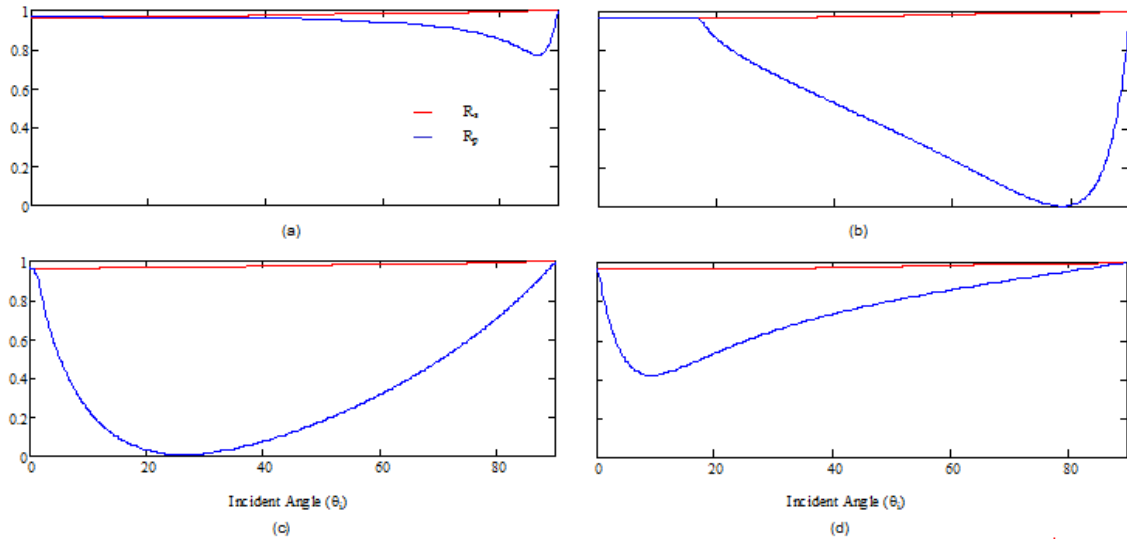


**Figure 6-8. Modeled Fresnel reflectance curves for an anisotropic uniaxial material, where  $n_x = n_y = 3.7$ ,  $\kappa_x = \kappa_y = 30.5$ ,  $n_z = 3$  (a), 0.3 (b), 0.03 (c), and 0.003 (d)  $\kappa_z = 0.01$ .**

**Biaxial anisotropic:** With two sets of complex refractive indexes to vary ( $\tilde{n}_y$  was held constant while  $\tilde{n}_x$  and  $\tilde{n}_z$  were varied), resonant behavior *similar* to those seen in the MMA data was obtained. But, like the previous modeling results, these are only of qualitative value. Figure 6-9 illustrates the resonant feature found from this modeling. The biaxial model is not expected to work either because the resonance in the measured  $R_p$  is attributed to an SPP resonance rather than from an effective medium.

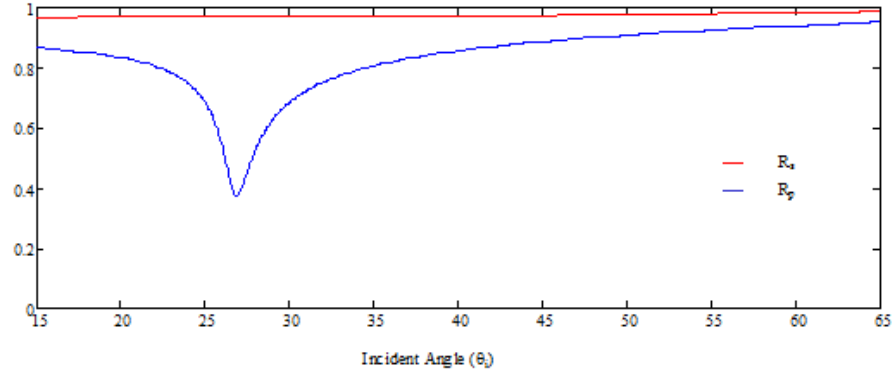


**Figure 6-9. Predicted Fresnel reflectances using an anisotropic biaxial model ( $n_x = 0.03$ ,  $\kappa_x = 0.05$ ,  $n_y = 3.7$ ,  $\kappa_y = 30.5$ ,  $n_z = 0.45$ ,  $\kappa_z = 0.01$ ).**

## 6.7 Example Behavior of the MMA

### 6.6.1 Stokes Interpretation

Three reflected Stokes vectors are shown in Figure 6-10, where (a) is from applying a linear horizontal polarization state (s-pol), (b) is from a linear  $+45^\circ$  state and (c) is from a right-hand-circular (RHC) polarization state. When the linear horizontal state is incident on the MMA, a linear horizontal state is returned. This trivial case is presented to illustrate the  $m_{11}$  term of the measured  $M_m$  can be used to determine this behavior and will always be unity for a Fresnel-type reflector. When a linear  $+45^\circ$  state is incident, a left-handed elliptical state is produced (values are present in  $S_1$ ,  $S_2$  and  $S_3$ ), which switches its rotation to right-handed at the resonance. The behavior of the elliptical state over the full range of incident angles is more accessible in the Poincaré sphere analysis presented in the next section. When the RHC state is incident, a left-hand elliptical state is produced with resonant behavior at the SPP mode.

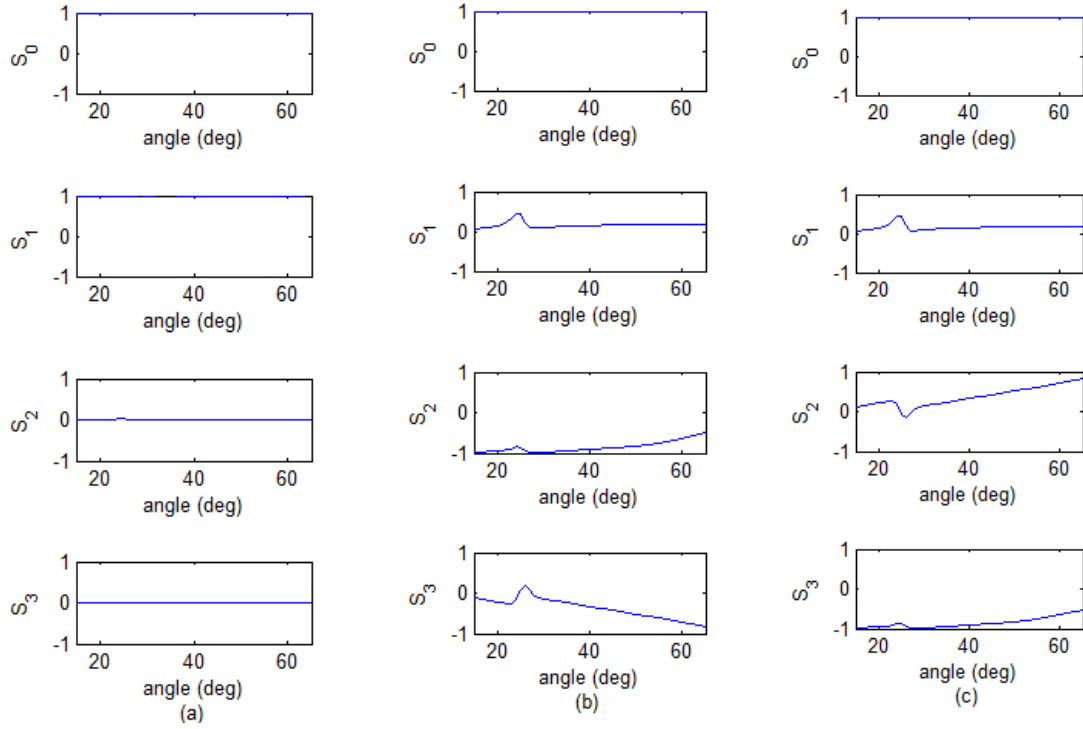


**Figure 6-10. Stokes plots for the MMA when canonical Stokes polarization states (a) horizontal (b)  $+45^\circ$  and (c) right-hand circular are applied to the extracted Mm, with the respective incident Stokes vector shown below each plot.**

### 6.7.2 Poincaré Sphere Interpretation

The Stokes vectors presented in the last section are inverted here to arrive at a more direct approach to evaluating the reflected behavior of the polarization states following the introduction of the linear  $+45^\circ$  and RHC states. The relationship between the Stokes-vector Poincaré-sphere angles' ellipticity ( $\chi$ ) and orientation ( $\psi$ ) are shown in the following equation [46].

$$\mathbf{S} = \begin{bmatrix} S_0 \\ S_1 \\ S_2 \\ S_3 \end{bmatrix} = \begin{bmatrix} 1 \\ \cos(2\chi) \cos(2\psi) \\ \cos(2\chi) \sin(2\psi) \\ \sin(2\chi) \end{bmatrix} \quad (6-20)$$

The value of the ellipticity ( $\chi$ ) is directly retrievable using  $S_3$ .

$$\chi = \frac{\sin^{-1}(S_3)}{2} \quad (6-21)$$

The orientation ( $\psi$ ) can be found from the ratio of  $S_2$  and  $S_1$ .

$$\psi = \frac{1}{2} \tan^{-1} \left( \frac{S_2}{S_1} \right) \quad (6-22)$$

Each of these angles is plotted for the linear  $+45^\circ$  and RHC cases in Figures 6-11 and 6-12.

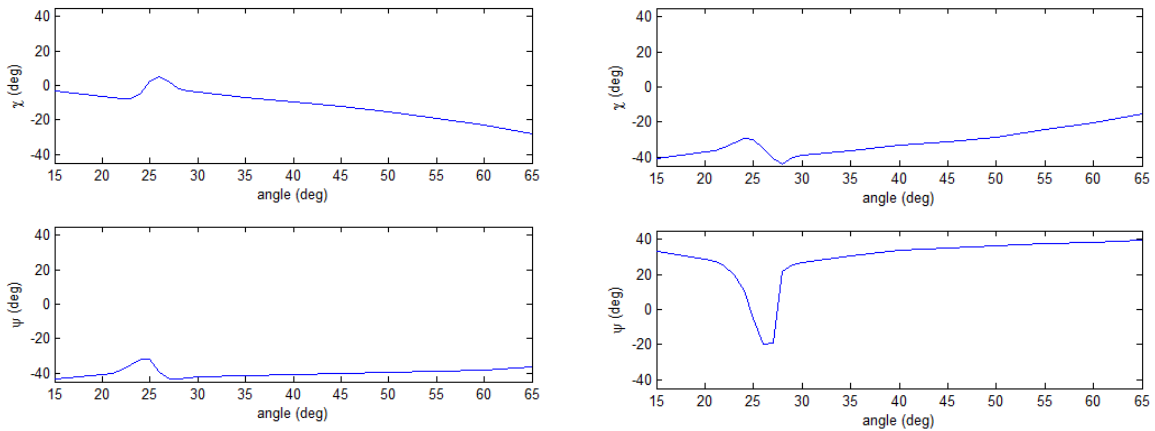


**Figure 6-11. The ellipticity ( $\chi$ ) and major axis orientation ( $\psi$ ) of the reflected Stokes vector with linear  $+45^\circ$  (left) and right hand circular (right) polarization states incident on the MMA at  $5.0\mu\text{m}$ .**

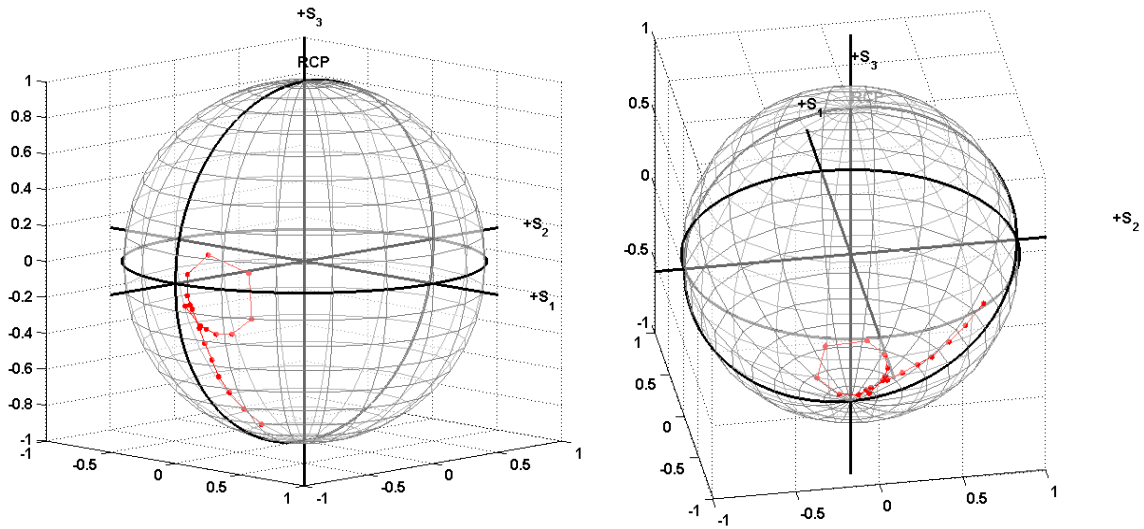


**Figure 6-12. Traces of the reflected polarization states on the Poincaré sphere for the MMA when the incident wavelength is 5.0μm and the polarization state is linear +45° (left) and RHC (right).**

## 6.8 Discussion and Conclusion

Measurements were conducted on an MMA with the Mm polarimeter to capture the SPP behavior in Mm form. The instrument was tuned to 5.0μm and measurements were collected at incident angles spanning 15-65°. The Mm extracted for the series of incident angles was distilled into s-pol and p-pol reflectance behaviors and the phase behavior found between the s-pol and p-pol reflectances. This was conducted so the experimental results could be analyzed in the context of Fresnel reflectance models for the isotropic, uniaxial anisotropic and biaxial anisotropic cases. It was determined that the isotropic and uniaxial anisotropic models could not be used to replicate the resonant behavior found in the p-pol reflectance data. And, while a resonant behavior could be produced using a biaxial anisotropic model ( $n_x \neq n_y \neq n_z$ ), a match to the measured data

could not be achieved. It is concluded that analyzing this MMA with an effective-medium Fresnel reflectance model is not appropriate due to the SPP resonance resulting from the MMA's periodic structure. An appropriate reflectance model having a periodic dependent description is required to simulate the measure results. Such a model should also demonstrate the conservation of energy interpretation (like Fresnel) to fully predict the Mm behavior of the sample.

Despite the lack of agreement between the measured data and the Fresnel reflectance models, the extracted Mm is valid (physically realizable) and follows the Mm reflectance model description. This said, example polarimetric reflectance behavior of the MMA was examined, assuming a set of canonical polarization states (linear horizontal, linear  $+45^\circ$ , and RHC) were incident on the material. This was used to show the predicted outgoing Stokes vectors and produce a Poincaré sphere interpretation of the reflected polarization states. The effects of the resonant reflectance behavior as well as the phase relationships between the s-pol and p-pol states were readily observed in this analysis.

This chapter demonstrated the modeling methodology and data distillation process applied to the first IR optical metamaterial measured with the tunable IR Mm polarimeter-scatterometer. Future measurement efforts with this instrument are expected to leverage from this analysis methodology. With this said, the next chapter reviews a compilation of recent samples/materials from literature with unique behaviors in the spectral range of this instrument and illustrate a non-exhaustive review of basic optical physics research opportunities available due to the development of this instrument.

## VII. FUTURE WORK

The Mueller matrix (Mm) polarimeter-scatterometer has demonstrated its ability to produce a unique data set for the analysis of infrared (IR) metamaterials samples. This instrument can be used to perform basic optical physics research of IR metamaterials and any other materials developed for applications in the 4.35-9.71 $\mu\text{m}$  wavelength range. Thus, this chapter is dedicated to identifying future work, as many novel materials are being developed in the spectral range of the tunable IR Mm polarimeter-scatterometer.

### 7.1 Metamaterial Absorbers

Metamaterial absorbers (MMAs) are among some of the most recent mid-wave IR (MWIR) and long-wave IR (LWIR) material developments. The Mm polarimeter-scatterometer has already been used to characterize the polarimetric behavior a MMA at 5.0 $\mu\text{m}$  [33]. However, there are several other architectures which have recently been developed and reside in the spectral range of the Mm polarimeter-scatterometer. Figure 7-1 shows the results of a theoretical study for materials designed for high absorption at infrared frequencies, where unit cell structure dimensions as well as dielectric thicknesses were modified to examine the predicted absorption behavior of these structures [74]. In Figure 7-2 and 7-3, two separate experimental MMA developments are shown which operate in for near the spectral domain of the Mm polarimeter-scatterometer. In Figure 7-2, a MMA was designed to have wide-band absorption from 3-12 $\mu\text{m}$  [75]. In Figure 7-3, a multiplexed MMA was designed for resonant absorption  $\sim 3.5\ \mu\text{m}$  [76] but could easily be modified to reach the spectral range of the instrument using guidance from [74].

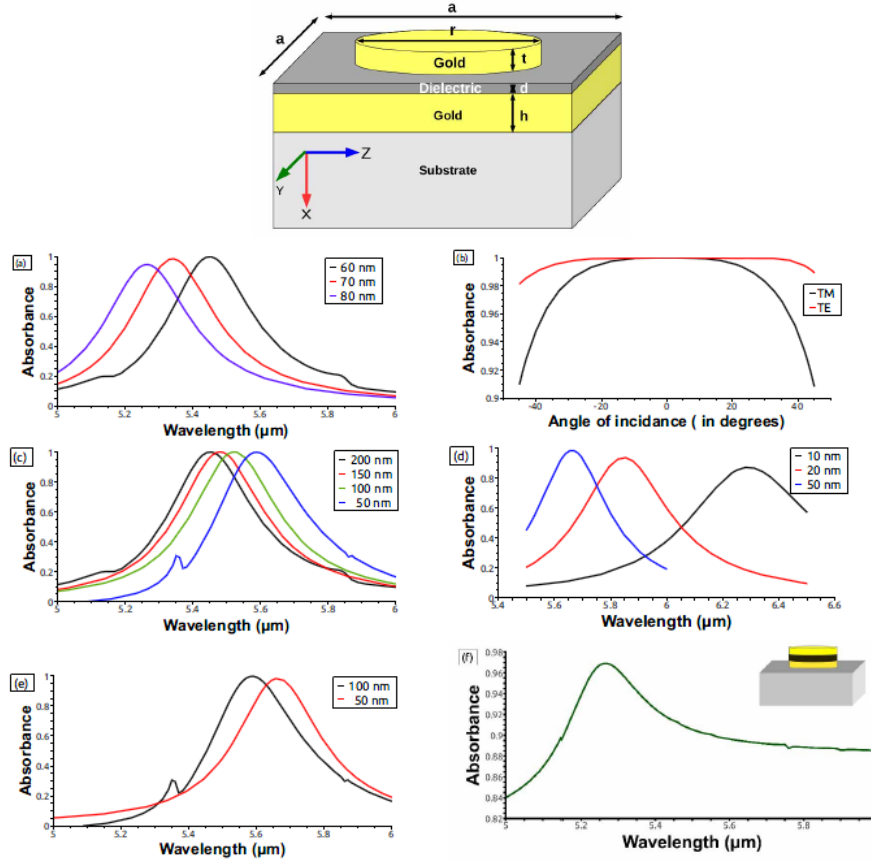


Figure 7-1. Theoretical MMA design (top) where the available unit cell dimensions are varied to show the expected changes in the resonant response [74].

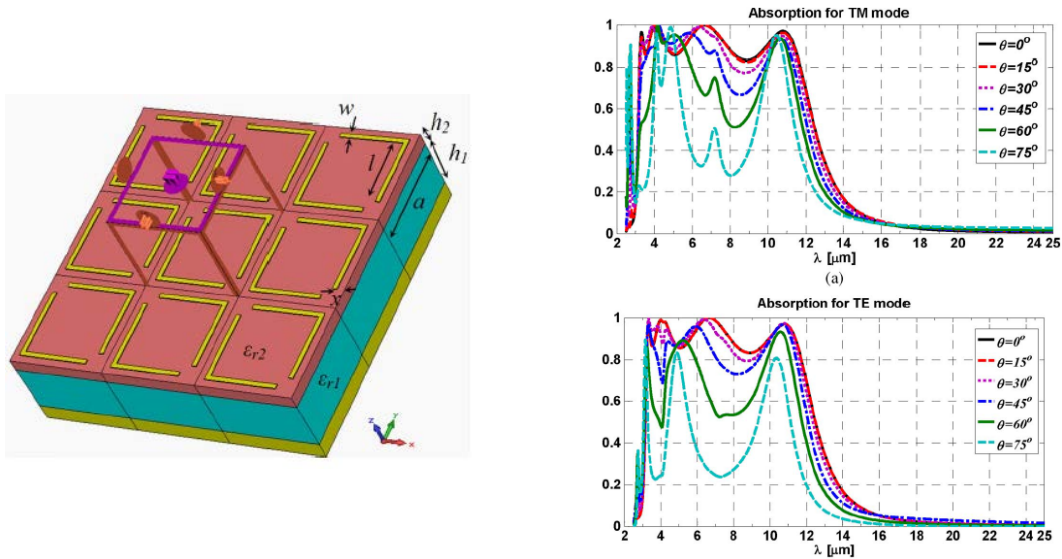
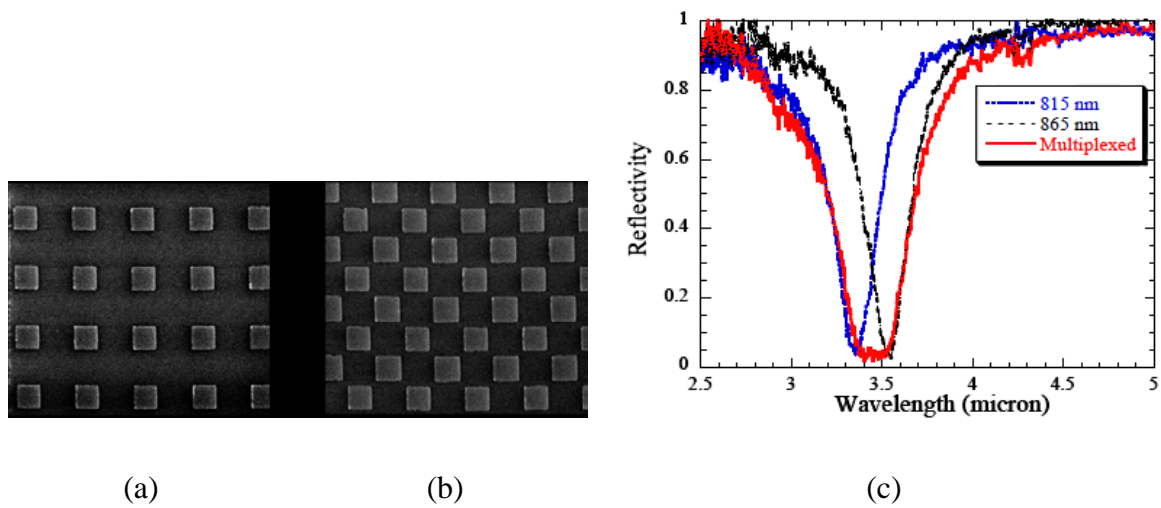


Figure 7-2. A wide-band MMA design (left) with its measured absorption (right) [75].



**Figure 7-3.** A non-multiplexed (a) and multiplexed (b) MMA design with the measured reflectance (c) [76].

## 7.2 Releasable IR Metamaterials

The concept of releasable IR metamaterials came from the need to deposit spectrally selective structures on a non-planar surface [77]. Much of the metamaterial work has been directed at developing resonant structures on substrates and thereby restricting their use to planar surfaces. These materials are in a unique research domain, and the Mm polarimeter-scatterometer has the spectral range to characterize them.

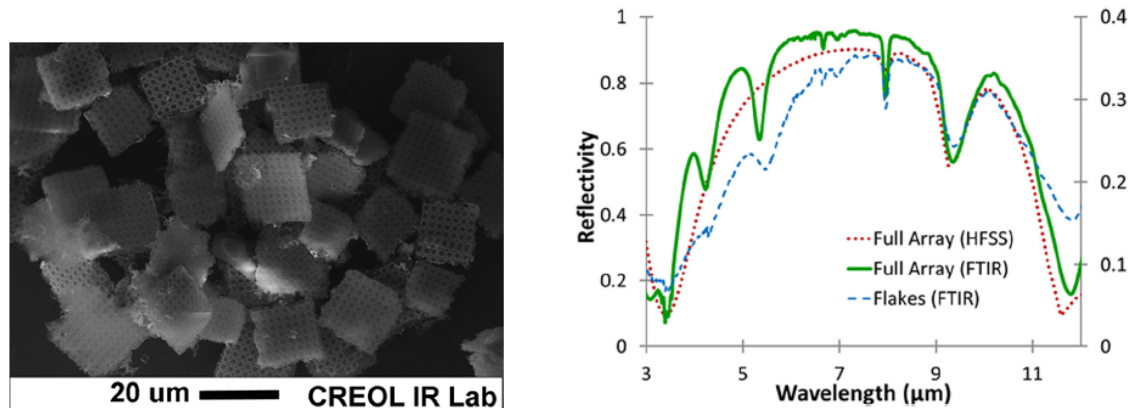


**Figure 7-4.** Scanning electron microscope (SEM) image of releasable IR metamaterial flakes (left) and the spectral reflectance (right), with the right axis depicting the measured results for the flakes [77].

### 7.3 Photonic Crystals

Photonic crystals represent yet another material with IR designs found in the spectral range of the Mm polarimeter-scatterometer. Figure 7-5 shows a three-dimensional photonic crystal made from tungsten having a photonic bandgap over the range of 8-20 $\mu\text{m}$  and strong absorption at 6 $\mu\text{m}$  near the band edge [78].

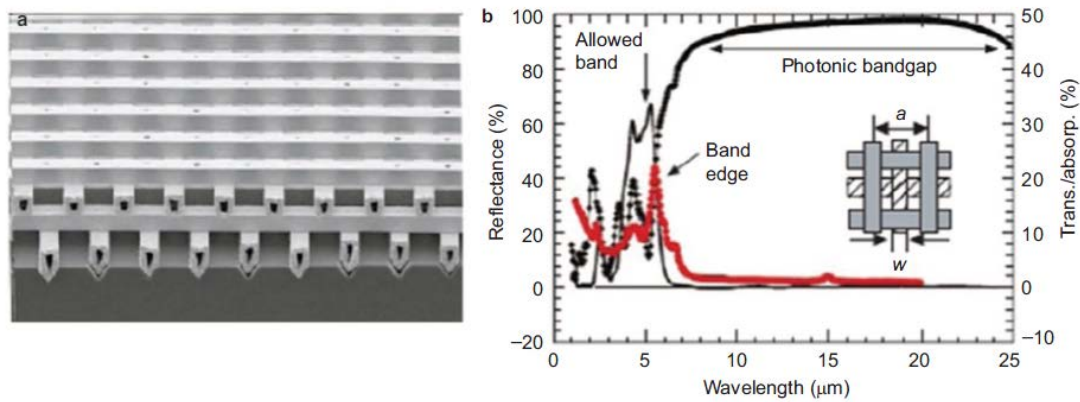


**Figure 7-5. SEM image (left) for a photonic crystal made of tungsten, which demonstrated a photonic bandgap over 8-20 $\mu\text{m}$  [78].**

### 7.4 Dielectric Resonators

Dielectric resonators have been recently introduced to metamaterials as a means of achieving optical magnetism with low-ohmic loss. Figure 7-6 shows the fabricated cubic dielectric array with its novel reflectance and transmittance spectra [79].

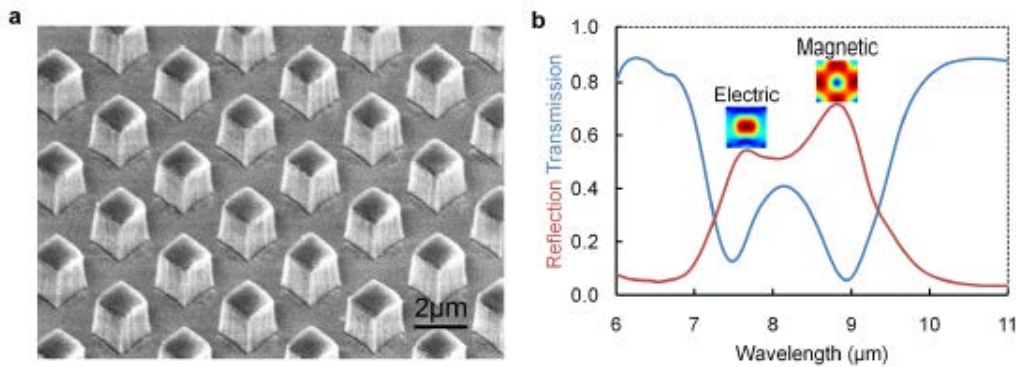


**Figure 7-6. SEM image of cubic dielectric array (left) with the unique reflectance and transmittance spectra (right) [79].**

## **7.5 Conclusion**

A non-exhaustive review of recent publications was conducted, where numerous materials have been developed for MWIR and LWIR wavelengths. Each of these materials was shown to have unique reflectance and transmittance spectra where basic optical physics research could be conducted on these materials with the use of the Mm polarimeter-scatterometer. This serves as further validation to the relevance of developing this one-of-a-kind instrument. Numerous collaboration opportunities are anticipated, and this instrument is expected to bring about deeper, physical understandings of these materials.

## VIII. DISCUSSION AND CONCLUSIONS

### 8.1 Research Objective Restatement

The body of research covered in this document was directed at identifying and solving problems affecting optical metamaterials research. A series of research objectives was assembled to address the use of effective medium theory (EMT) in the simplest structures of metamaterial research and address the absence of an instrument capable of meeting the full-directional and full-polarization characterization demands of infrared metamaterials.

- *Model, design, fabricate and test an optical near-zero permittivity structure and identify the appropriate design constraints to apply for EMT usage in the design and post-fabrication analysis steps*
- *Develop an optimal dual rotating retarder (DRR) polarimeter which is compatible with mid-wave infrared (MWIR, 4.37-6.54 $\mu\text{m}$ ) and long-wave infrared (LWIR, 7.41-9.71 $\mu\text{m}$ ) wavelengths*
- *Develop the first tunable IR Mm polarimeter-scatterometer for the characterization of IR optical metamaterials*
- *Measure an IR metamaterial with the tunable IR Mueller matrix (Mm) polarimeter, determine the appropriate model needed to replicate the experimental results, and perform polarimetric analysis using canonical polarization states to describe the measured results*

### 8.2 Research Objective Accomplishment

The research objectives in this research were primarily accomplished in a model, design, and then experimentally verify approach. The first of which was identifying the dimensional constraints necessary to bring EMT and transfer matrix method (TMM) modeling into agreement for near-zero permittivity designs created from periodic, layered metal-dielectric media. Four near-zero permittivity design structures with periods

numbering one to four and having a  $\lambda/3$  design constraint were fabricated for this work, and the TMM model was confirmed accurate for all four samples. The EMT model did not accurately predict the reflectance and transmittance results for these structures. Using TMM as the model truth source, design dimensions of the near-zero permittivity design were reduced until evidence of model-to-model agreement was achieved – that dimensional constraint was  $\lambda/10$ . The contributions from this research have been accepted for publication in Optics Express [8].

The next problem confronted in this research was the development of a tunable IR Mm polarimeter-scatterometer. This instrument was needed because of the lack of an instrument having full-directional (specular, off-specular, in-plane, out-of-plane), full polarimetric and the spectral range to robustly characterize IR optical metamaterials. Targeting the IR was important for the early identification of problems in optical metamaterials because the natural design progression is from the IR to visible wavelengths. Initial efforts to develop this instrument commenced with beam train modifications to an existing SMS CASI® and utilizing existing sets of  $\lambda/4$  retarders designed for 3.39 and 10.6 $\mu\text{m}$  wavelengths to implement a dual rotating retarder (DRR), which is used to make the instrument a Mm polarimeter-scatterometer. The retarders, initially on-hand, were found incompatible with the tunable EC-QCL sources from FTIR measurements and random error analysis, which showed retardances below  $\lambda/4$  led to poor error performance of the instrument. This same error analysis was used to determine the optimal retarder and retarder rotation ratio to apply to the instrument – retarders having  $\lambda/3$  retardance and rotated according to a Fourier method rotation ratio (25:5 or

37.5:7.5 were found optimal) [28-30]. The contribution from this research has been submitted for publication in Measurement Science and Technology Journal in November 2012 [30].

The  $\lambda/3$  retarders were not on-hand, so design specs were coordinated with Gooch and Housego to produce two sets of achromatic  $\lambda/3$  retarders. Obtaining stable retardance and anti-reflective coatings is extremely challenging over the 4.35-9.71 $\mu\text{m}$  wavelengths spanned by the EC-QCLs and it was important to maintain the retardances below  $135^\circ$  for compatibility with an existing DRR calibration technique [40], so two sets were designed. One spanned 4.35-6.5 $\mu\text{m}$  and the other set spanned 7.4-10.6 $\mu\text{m}$ ; there was a natural break in the EC-QCLs that facilitated a clean definition for the two sets of retarders. The  $\text{CO}_2$  laser wavelength was included in the span of the second set of retarders as an improvement measure for the DRR at 10.6 $\mu\text{m}$ . When the  $\lambda/3$  retarders were introduced to the CASI®, they met the predictions of the random error analysis (~1% error in the free-space measurement). The contributions of this research are in draft form with a planned submission to the Review of Scientific Instruments [31].

While awaiting the delivery of the  $\lambda/3$  retarders, work with the CASI® was conducted at 3.39 $\mu\text{m}$ . It was while operating at this wavelength that Mm reflectance modeling commenced. This model was first used to predict the Mm behavior of a gold mirror at the 3.39 $\mu\text{m}$  operating wavelength. The modeling resumed once the  $\lambda/3$  retarders arrived, where Mm measurements were conducted at 5.0 $\mu\text{m}$ . Both sets of measurements were in good agreement with the Mm reflectance model despite being conducted at IR

wavelengths where a gold mirror behaves as an ideal reflector at nearly all incident angles. This model was later used to deduce the behavior of a MMA.

A unique MMA was measured with the tunable IR Mm polarimeter-scatterometer. As a scatterometer, the tiled features stemming from the electron-beam lithography mask used to design the material were evident, with strong diffractive results seen in the Mm plots [31]. As a Mm polarimeter, the behavior of an SPP resonance was observed when measurements were collected at  $5.0\mu\text{m}$  and incident angles spanning  $15^\circ$ – $65^\circ$ . The SPP resonance was first seen in the broad-band IR-VASE measurement, as an incident angle dependent resonance in the p-pol reflectance was observed. Phase matching analysis was conducted to confirm the presence of an SPP mode. This analysis predicted a  $5.0\mu\text{m}$  SPP resonance near  $25^\circ$  incident angle, where the SPP mode was found and the Mm that was extracted captured the polarimetric characteristics of an SPP mode for the MMA.

The extracted Mm for the MMA was found to populate the Mm elements similar to how a gold mirror would (a Fresnel reflector having a complex refractive index), with the exceptions of stronger roll-offs with increasing incident angles and the resonant feature coming from the SPP resonance. The behavior of the s-pol ( $R_s$ ) and p-pol ( $R_p$ ) reflectances were distilled from the measured data as was the phase behavior between these two polarization states. While  $R_s$  appeared similar to an isotropic Fresnel reflectance,  $R_p$  did not. In any case, the models for  $R_s$  and  $R_p$  were assumed Fresnel-like to perform analysis for the isotropic, uniaxial anisotropic and biaxial anisotropic cases – in an attempt to replicate the resonant behavior found in  $R_p$ .

The isotropic and uniaxial anisotropic models were found incapable of producing the resonant feature found in the  $R_p$  data. When the Fresnel model was relaxed to biaxial anisotropic considerations, a resonant feature similar to the  $R_p$  could be attained, but a match to the measured data could not be achieved. It is concluded that analyzing this MMA with an effective-medium Fresnel reflectance model is not appropriate due to the SPP resonance resulting from the MMA's periodic structure. Thus, it is concluded that Fresnel modeling could not be expected to replicate the  $R_p$  behavior accurately, and an energy-conserving, periodic description of the material is necessary to predict the p-pol reflectance and achieve Mm predictions for the MMA sample – and likewise will be needed for future SPP resonant analysis.

Despite these Fresnel model findings, the Mm extracted for the sample was found to be physically realizable and is valid. Thus, the extracted Mm for the MMA was used to produce predictions for the polarimetric behavior of reflected Stokes vectors under incident canonical Stokes states (or any Stokes-defined polarization state of interest). The Stokes analysis also led to a useful Poincaré sphere interpretation for a visual depiction of reflected states as a function of incident angle. The contributions from this research represent original, unpublished work, which are planned submission to *Applied Physics Letters*.

Table 8-1 provides a summary of the contributions from this research, which span refereed journals, conference proceedings papers and conference presentations.

**Table 8-1 List of Contributions**

<b>Refereed Publications</b>	
[8]	Vap, J., Seal, M.D., Marciniak, M.A., Johnson, L. and Moran, M., “Practical design constraints for stratified optical near-zero effective permittivity structures,” accepted to Opt. Exp. (Nov 2012).
[30]	Vap, J., Nauyoks, S. and Marciniak, M. A., “Evaluation and optimization of a tunable mid-wave infrared Mueller-matrix polarimeter-scatterometer,” Meas. Sci. and Tech, manuscript submitted 1 Nov 2012.
[31]	Vap J., Nauyoks, S., Benson, M., Fitzgerald, T. and Marciniak, M.A., “Tunable infrared Mueller-matrix polarimeter-scatterometer for the evaluation of optical metamaterials,” manuscript prepared for submission to Rev. of Sci. Instr.
	Vap J., Nauyoks, S. and Marciniak, M.A., “Full-polarimetric analysis of a metamaterial absorber,” preparing manuscript for submission to App. Phys. Lett.
<b>Conference Proceedings</b>	
[28]	Vap, J., Nauyoks, S., Fitzgerald, T. and Marciniak, M. A., “Development of a tunable polarimetric optical scattering instrument from 4.3-9.7 Microns,” Proc. SPIE <b>8154</b> , 815412 (2011).
[29]	Vap, J. Nauyoks, S. and Marciniak, M. A., “Optimization of a mid-wave tunable polarimetric optical scatter instrument,” Proc. SPIE <b>8364</b> , 836405 (2012).
[34]	Vap, J. and Marciniak, M.A., “Examining epsilon near zero structures through effective medium theory and optical thin film analysis,” Proc. SPIE <b>8364</b> , 836426 (2012).
<b>Presentations</b>	
	“Development of a tunable polarimetric optical scattering instrument from 4.3-9.7 Microns,” SPIE Optics and Photonics Conference, San Diego, CA, Aug 2011.
	“Optimization of a mid-wave tunable polarimetric optical scatter instrument,” SPIE Defense Sensing and Security Conference, Baltimore, MD, Apr 2012.
	“Examining epsilon near zero structures through effective medium theory and optical thin film analysis,” SPIE Defense Sensing and Security Conference, Baltimore, MD, Apr 2012.

## APPENDIX A

### A.1 Complex Refractive Index Data

There are two sets of commonly used complex refractive index data for the common noble metals referenced in metamaterial literature, Palik [36] and Johnson [37]. The common noble metals referred to are silver (Ag), gold (Au) and copper (Cu). Tabular forms of these data can be found in the original publications and electronic forms can be found at a refractive index website [73]. Comparisons of the data are shown in Figure A-1. The general findings for Johnson's Ag data were lower values for the real part and higher values for the imaginary part of the complex refractive index.

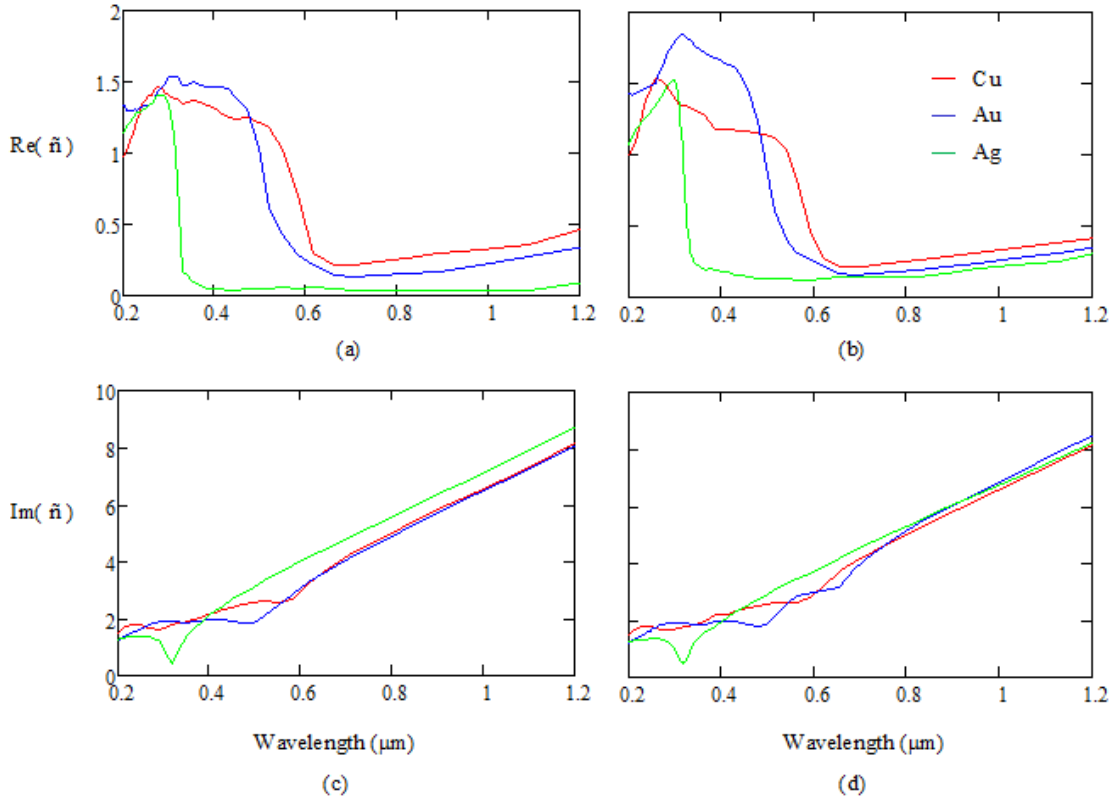


**Figure A-1. Comparison of complex refractive index data from Johnson [37] (a) and (c) Palik's [36] (b) and (d) for the noble metals copper (Cu), gold (Au) and silver (Ag).**

Differences between the data sets will obviously lead to differences in the modeled reflectance and transmittance spectra. When using Johnson's data for ENZ modeling, it over predicted the transmission results that were experimentally achieved at short wavelengths (long ultraviolet and short visible). It was originally believed due to lower values for the imaginary component of the complex refractive index. The data of Figure A-1 suggested otherwise – Johnson's  $\text{Im}(\tilde{n})$  data was actually higher than Palik's. Additionally found, the real component of the complex refractive index was found to be lower in Johnson's data than in Palik's. What this suggests is that considering each of these complex refractive index values in isolation at these wavelengths leads to erroneous expectations (expected high reflectance for low  $\text{Re}(\tilde{n})$  and low transmission for high  $\text{Im}(\tilde{n})$ ). Thus, I turned to modeling to arrive at to arrive at what could be expected from a 30nm layer of Ag using the transfer matrix modeling discussed in Chapter 3. The reflectance and transmittance spectra were calculated, and they were summed to illustrate conservation of energy and to identify where absorption would take place. The results are shown in Figure A-2.

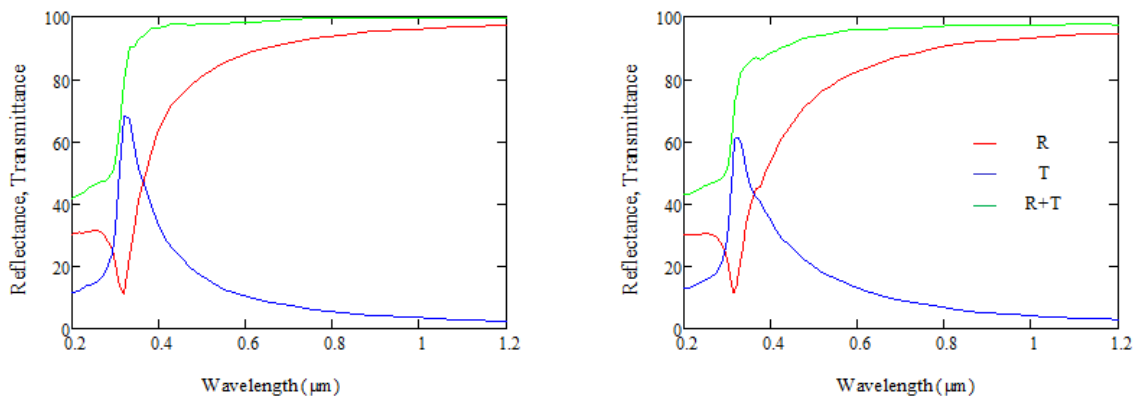


**Figure A-2. Modeled reflectance and transmittance spectra for a 30nm layer of Ag using the complex refractive index data from Johnson [37] (left) and Palik [36] (right).**

## A.2 Complex Permittivity Data

The relationship between the complex permittivity and the complex refractive index at optical frequencies is

$$\tilde{n} = n + i\kappa = \sqrt{\tilde{\epsilon}}, \quad (\text{A-1})$$

where  $n$  refers to the refractive index and  $\kappa$  refers to the absorption index. This leads to the following relationships for the real and imaginary components of the complex permittivity [1], which are plotted in Figure A-3 from bulk data [35,36].

$$\text{Re}(\tilde{\epsilon}) = n^2 - \kappa^2 \quad (\text{A-2})$$

$$\text{Im}(\tilde{\epsilon}) = 2n\kappa \quad (\text{A-3})$$

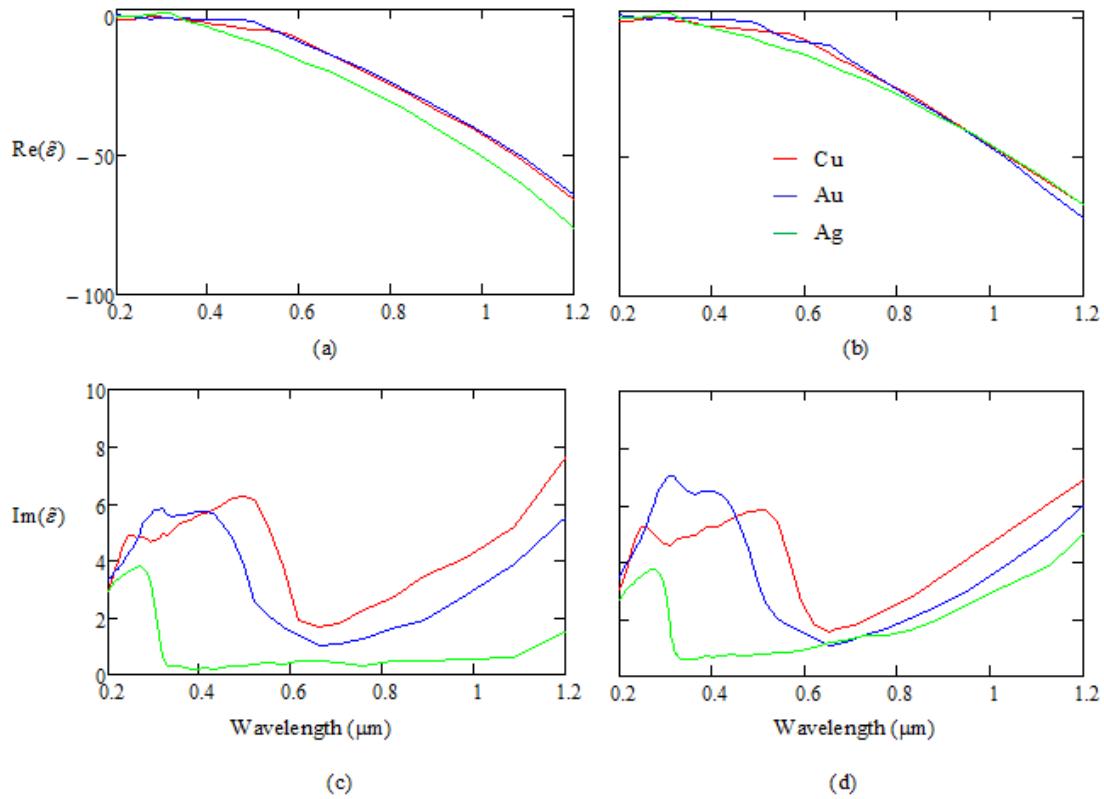


**Figure A-3. Comparison of complex permittivity data from Johnson [37] (a) and (c) and Palik [36] (b) and (d) for the noble metals copper (Cu), gold (Au) and silver (Ag).**

These plots again show the differences in the bulk data. Figure A-4 is a zoomed in view of the zero crossings for the permittivity of each of the noble metals each of which exist at ultraviolet frequencies (below  $0.4\mu\text{m}$ ). When developing zero permittivity structures for the visible frequencies using metal-dielectric layers, the design goal is to dilute the permittivity with the introduction of a positive permittivity material (dielectric). This *pushes* the zero permittivity to longer wavelengths, which will be observed in the modeling and experimental results when proper scaling of the dielectric thicknesses are adhered to [8].

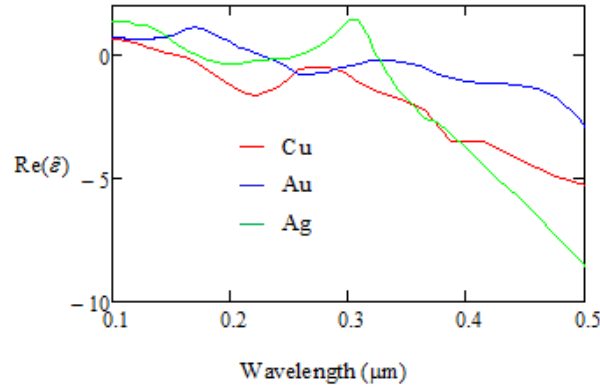


**Figure A-4. The real part of the complex permittivity from Palik's data [36], which show the zero crossings.**

### **A.3 Practical design constraints to achieve a near zero permittivity structure**

The contents of Chapter 3 were directed at finding the practical design constraints (dielectric thicknesses) to apply to a stratified composite metal-dielectric near-zero permittivity design structure. The plot in Figure 3-2 (f) illustrated the design region which should be targeted; this was the region where the best agreement between the transfer matrix method (TMM) and effective medium theory (EMT) modeling occurred. Table A-1 shows the design values for the perimeter of this figure (left hand side and the diagonal

running up the right hand side of the design region) as well as wavelengths in the heart of the design region (0.4 $\mu$ m). The highlighted region in the table depicts the near-zero permittivity design values for the Ag/AlN structures modeled and experimentally examined in Chapter 3.

**Table A-1.  $\lambda/10$  design values tested for TMM and EMT agreement**

$f_m(\lambda, n)$	$f_m$	$f_d$	$t_d$	$n$	$\lambda$
$f_m(2.0, 0.35)$	0.69	0.31	9.0nm	2.0	0.35 $\mu$ m
$f_m(3.0, 0.35)$	0.83	0.17	4.0nm	3.0	0.35 $\mu$ m
$f_m(4.0, 0.35)$	0.90	0.10	2.0nm	4.0	0.35 $\mu$ m
$f_m(2.0, 0.4)$	0.51	0.49	19.0nm	2.0	0.4 $\mu$ m
$f_m(3.0, 0.4)$	0.70	0.30	8.0nm	3.0	0.4 $\mu$ m
$f_m(4.0, 0.4)$	0.81	0.19	5.0nm	4.0	0.4 $\mu$ m
* $f_m(2.0, 0.63)$	0.20	0.80	80.0nm	2.0	0.63 $\mu$ m
$f_m(3.0, 0.47)$	0.56	0.44	16.0nm	3.0	0.47 $\mu$ m
$f_m(4.0, 0.55)$	0.60	0.4	14.0nm	4.0	0.55 $\mu$ m
*Actual values used in the ENZ design tested, which meet $\lambda/3$ design constraints rather than the $\lambda/10$ design constraints met among the points tested above.					

#### **A.4 TMM and EMT model agreement**

The design values identified in Table A-1 were used to generate the TMM and EMT plots found in Figures A-5 and A-6. Each plot in Figure A-5 shows good agreement between the TMM and EMT modeling; this is generally because the design values fall below the  $\lambda/10$  constraint. What is seen among the 0.4 $\mu$ m designs is diminishing

agreement between the TMM and EMT models as the refractive index is increased.

Figure A-6 shows that the  $\lambda/10$  constraint may require tightening up for designs using large refractive index ( $n=4$ ), as the agreement between the models above the design wavelength begins to deteriorate.

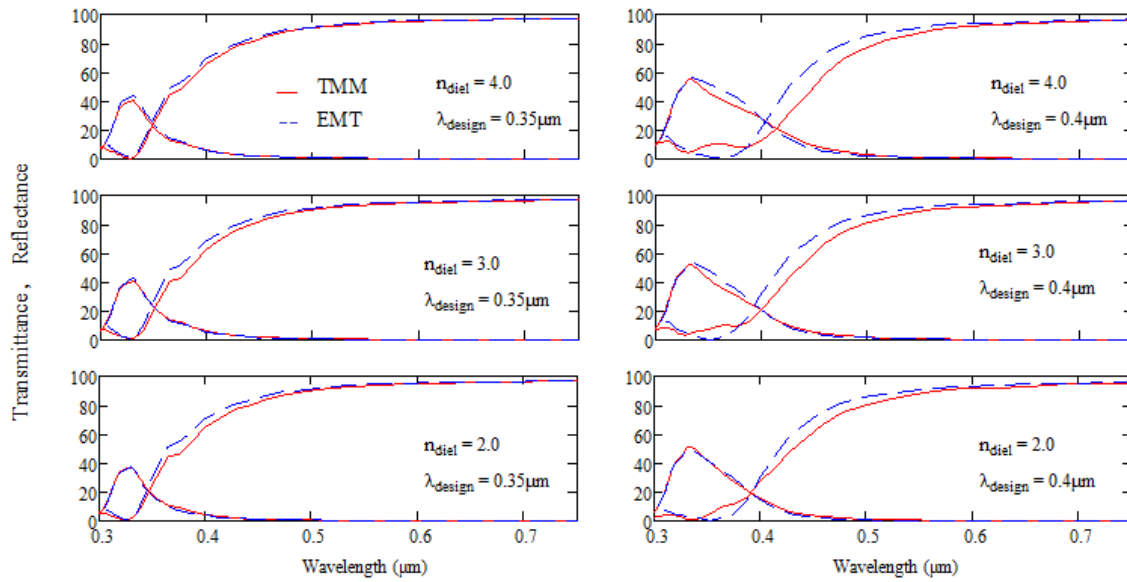


**Figure A-5. EMT to TMM modeling comparison of a four period structure at the design wavelengths of 0.35 and 0.4  $\mu\text{m}$  for the refractive indexes  $n=2, 3$  and 4.**

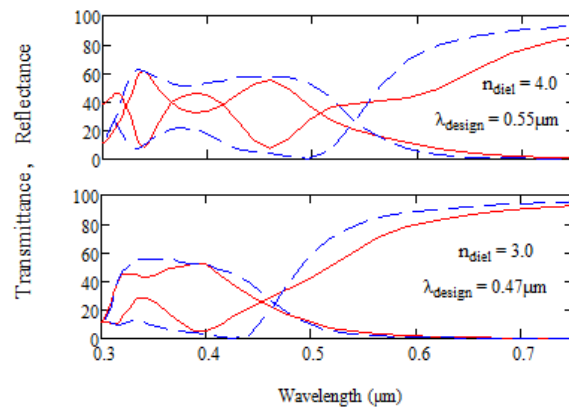


**Figure A-6. EMT to TMM modeling comparison of a four period structure at the design wavelengths 0.47 and 0.55  $\mu\text{m}$  for the refractive indexes  $n = 2.0$  and  $n = 4.0$ , respectively.**

## APPENDIX B

### B.1. Mueller Matrix Model for Fresnel Reflector – Gold Mirror

The Mueller matrix (Mm) for a gold mirror can be modeled according to the Mm reflectance model covered in Chapter 6. The normalized Mm of Eqn. (6-13) is restated as Eqn. (B-1) here.

$$M_{R\_nmeas} = \begin{bmatrix} \frac{R_s + R_p}{R_s + R_p} & \frac{R_s - R_p}{R_s + R_p} & 0 & 0 \\ \frac{R_s - R_p}{R_s + R_p} & \frac{R_s + R_p}{R_s + R_p} & 0 & 0 \\ 0 & 0 & \frac{-2\sqrt{R_s R_p} \cos(\delta_p - \delta_s)}{R_s + R_p} & \frac{-2\sqrt{R_s R_p} \sin(\delta_p - \delta_s)}{R_s + R_p} \\ 0 & 0 & \frac{2\sqrt{R_s R_p} \sin(\delta_p - \delta_s)}{R_s + R_p} & \frac{-2\sqrt{R_s R_p} \cos(\delta_p - \delta_s)}{R_s + R_p} \end{bmatrix} \quad (B-1)$$

The reflectance terms ( $R_s$  and  $R_p$ ) refer to the s-polarized (s-pol) and p-polarized (p-pol) Fresnel reflectances and phases ( $\delta_s$  and  $\delta_p$ ) gained upon reflection. Each of these terms are not repeated here but can be found in Eqns. 6-7 through 6-10. When the complex refractive index ( $\tilde{n}$ ) is used in these relationships, each of the elements in the reflectance-defined Mm can be modeled. Figure B-1 and B-2 are used to illustrate the expected behavior of the affected Mm elements for reflectance from a gold mirror as a function of incident angle and wavelength. Figure B-1 just shows the  $m_{10}$  term, which is the same as the  $m_{01}$  term. The  $m_{00}$  and  $m_{11}$  terms evaluate to unity and thus are not shown. Figure B-2 shows  $m_{22}$ ,  $m_{23}$ ,  $m_{32}$ , and  $m_{33}$ , which are the elements that show the retardance effects of the gold mirror due to the phase differences between the reflected s-pol and p-pol states.

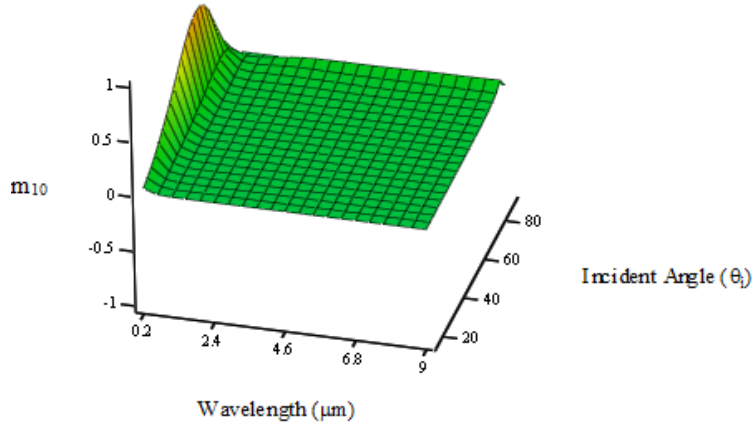


**Figure B-1.** The modeled  $m_{10}$  term of the normalized reflectance  $M_m$  for a gold mirror.

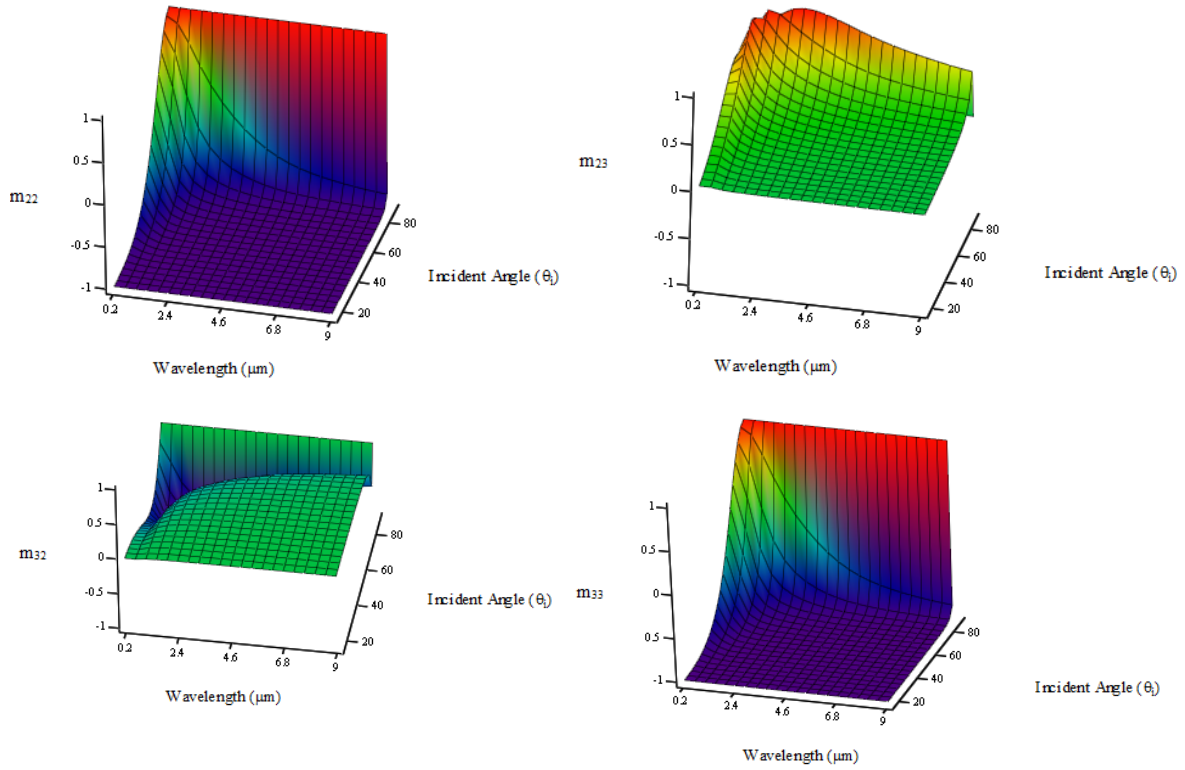


**Figure B-2.** The modeled  $m_{22}$ ,  $m_{23}$ ,  $m_{32}$ , and  $m_{33}$  terms of the normalized reflectance  $M_m$  for a gold mirror.

From the modeled results it can be seen that there is not a strong signature in the  $m_{10}$  term (and similarly the  $m_{01}$  term) at infrared wavelengths; however there are strong

differences between the s-pol and p-pol reflectances that lead to an observable signature at the visible (0.4 to 0.7 $\mu\text{m}$ ) and ultra-violet (0.2-0.4 $\mu\text{m}$ ) wavelengths shown. Similar effects can be seen in the Mm elements shown in Figure B-2, where there is not a strong signature found at infrared wavelengths but strong signatures exist again at the visible and ultra-violet wavelengths shown.

Mm measurements were collected of a gold mirror at 3.39 $\mu\text{m}$  and 5.0 $\mu\text{m}$  with the Mm polarimeter and compared with the modeling results coming from the use of Eqn. (B-1) and Palik's bulk complex refractive index data for Au [36] at these wavelengths. Comparisons between the measured and modeled results for the  $m_{22}$ ,  $m_{23}$ ,  $m_{32}$ , and  $m_{33}$  elements are shown in Figure B-3. The other Mm elements are not shown because they

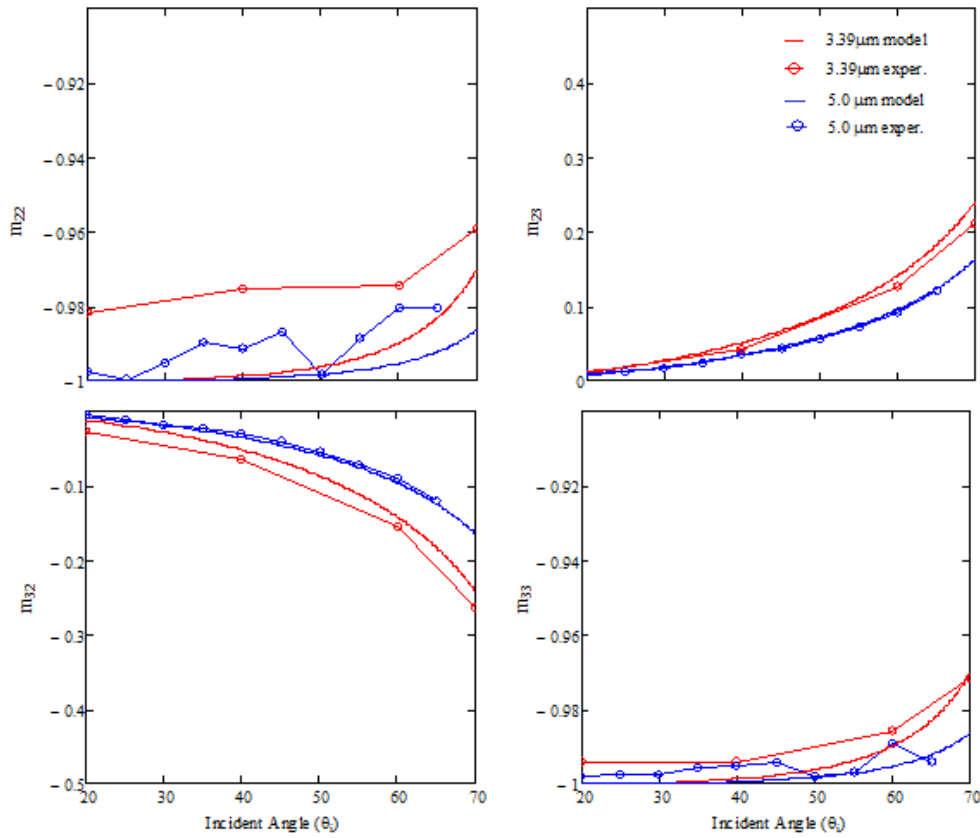


**Figure B-3. Modeled-to-measured results comparison of the  $m_{22}$ ,  $m_{23}$ ,  $m_{32}$ , and  $m_{33}$  elements of a Mm reflectance for a gold mirror at 3.39 $\mu\text{m}$  and 5.0 $\mu\text{m}$ .**

evaluate to one or zero. Overall, good agreement between the modeled and measured Mm for the gold mirror were found at  $3.39\mu\text{m}$  and  $5.0\mu\text{m}$  and provided the necessary confidence in measurements collected from the Mm polarimeter to move forward with measuring metamaterials.

## B.2 Mm Polarimeter Measurements of Gold Mirror

The full Mm results from the gold mirror measurements collected at  $3.39\mu\text{m}$  and  $5.0\mu\text{m}$  are shown in Figure B-4 and B-5, respectively. To reiterate, the values found in the Mm elements  $m_{22}$ ,  $m_{23}$ ,  $m_{32}$  and  $m_{33}$  of these two plots are shown in Figure B-3 for the Mm reflectance model comparison.

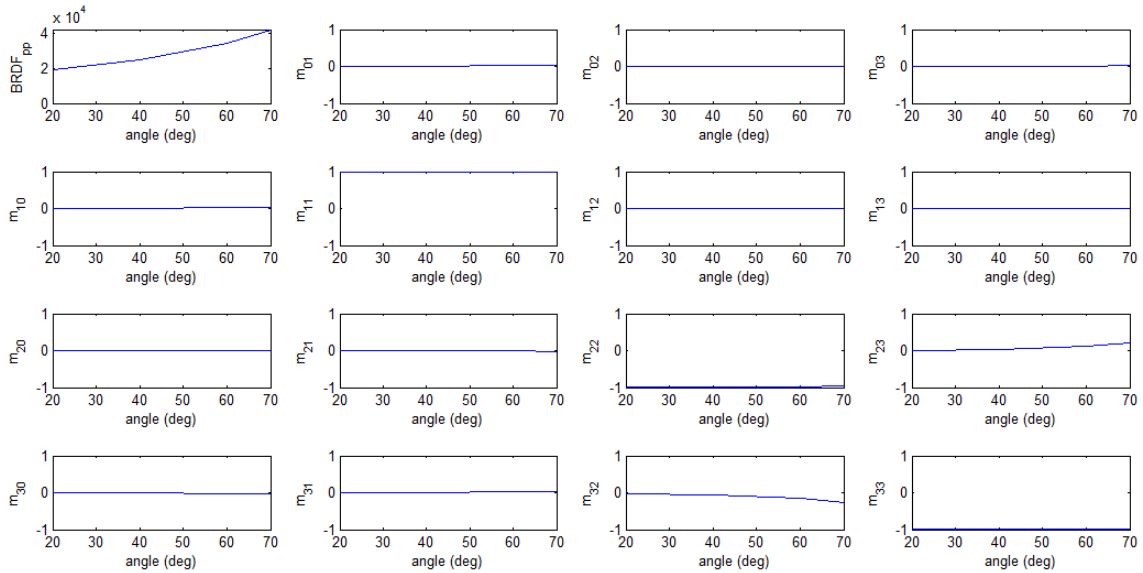


**Figure B-4. Mm plot for a gold mirror at  $3.39\mu\text{m}$ .**

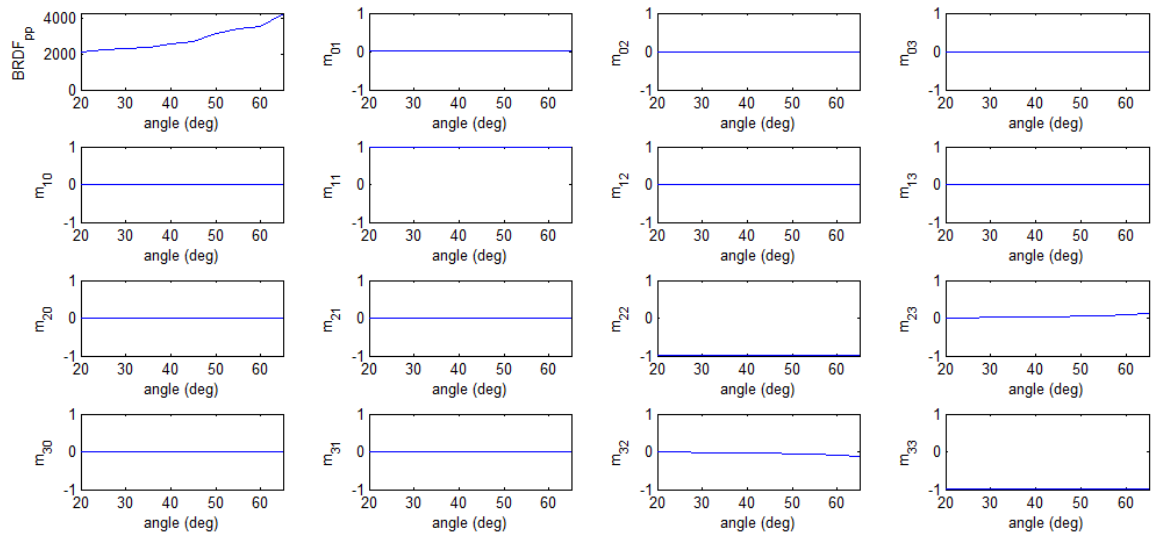


**Figure B-5. Mm plot for a gold mirror at  $5.0\mu\text{m}$ .**

## BIBLIOGRAPHY

- [1] Cai, W. and Shalaev, V., [Optical Metamaterials], Springer, New York (2010).
- [2] Pendry, J., "Metamaterials in the sunshine," *Nature* **5**, 599-600 (2006).
- [3] "Photonic Metamaterials." *Article on Photonic Metamaterials, Negative-index Media, Negative Refraction, Cloaking*. N.p., N.d. Web. 21 Nov. 2012. <[http://www.rp-photonic.com/photonic\\_metamaterials.html](http://www.rp-photonic.com/photonic_metamaterials.html)>.
- [4] Simovski, C.R. and Tretyakov, S.A., "Local constitutive parameters of metamaterials from an effective-medium perspective," *Phys. Rev. B* **75**, 195111 (2007).
- [5] Soukoulis, C.M., Zhou, J., Koschny, T., Kafesaki, M. and Economou, E.N., "The science of negative index materials," *J. Phys: Condens. Matt.* **20**, 304217 (2008).
- [6] Karri J. and Mickelson, A.R., "Silver dielectric stack with near-zero epsilon at a visible wavelength," 2009 IEEE Nano. Matl. Dev. Conf., 148-53 (2009).
- [7] Roberts, M.J., Feng, S., Moran, M. and Johnson, L., "Effective permittivity near zero in nanolaminates of silver and amorphous polycarbonate," *J. Nano.* **4**, 043511 (2010).
- [8] Vap, J., Seal, M.D., Marciniak, M.A., Johnson, L. and Moran, M., "Practical design constraints for stratified optical near-zero effective permittivity structures," accepted to *Opt. Exp.* (Nov, 2012).
- [9] Menzel, C., Rockstuhl, C., Paul, T. and Lederer, F., "Retrieving effective parameters for metamaterials at oblique incidence," *Phys. Rev B* **77**, 195328 (2008).
- [10] Jakoljecic, M.M., Isic, G., Basic, B., Oates, T.W.H., Hinrichs, K., Bergmair, I., Hingerl, K., and Gajic, R., "Spectroscopic ellipsometry of split ring resonators at infrared frequencies," *Appl. Phys. Lett.* **100**, 11105 (2012).
- [11] Marciniak, M.A., Sellers, S.R., Lamott, R.B., and Cunningham, B.T., "Bidirectional scatter measurements of a Guided Mode Resonant Filter photonic crystal structure," *Opt. Exp.* **20**, 27242 (2012).
- [12] Burckel, D.B., Wendt, F.R., Ten Eyck, G.A., Ellis, A.R., Brener, I. and Sinclair, M.B., "Fabrication of 3D Metamaterial resonator using self-aligned membrane projection lithography," *Adv. Matt.* **22**, 3171 (2010).
- [13] Burckel, D.B., Wendt, J.R. Ten Eyck, G.A., Ginn, J.C., Ellis, A.R., Brener, I., and Sinclair, M.B., "Micrometer-scale cubic unit cell 3D metamaterial layers," *Adv. Matt.* **22**, 5053 (2010).

- [14] Jiu, B., Wu, S., Li, J. and Gu, M., "Near-infrared high refractive-index three-dimensional inverse woodpile photonic crystals generated by a sol-gel process," *J. Appl. Phys.* **102**, 096102 (2007).
- [15] Wu, C., Nuener III, B., John, J., Milder, A., Zollars, B., Savoy, S. and Shvets, G., "Metamaterial-based integrated plasmonic absorber/emitter for solar thermovoltaic systems," *J. Opt.* **14**, 024005 (2012).
- [16] El-Kady, I., Biswas, R., Ye, Y., Su, M.F., Puscasu, I., Pralle, M., Johnson, E.A., Daly, J. and Greenwald, A., "Tunable narrow-band infrared emitters from hexagonal lattices," *Photonics and Nanostructures – Fundamental and Applications* **1**, 69 (2003).
- [17] Watts, C.M., Liu, X. and Padilla, W.J., "Metamaterial electromagnetic wave absorbers," *Advanced Opt. Matl.* **24**, 98-120 (2012).
- [18] Sai, H., Yugami, H., Kanamori, Y. and Hane, K., "Spectrally selective thermal radiators and absorbers with periodic microstructured surface for high-temperature applications," *Microscale Thermophysical Engineering* **7**, 101 (2003).
- [19] Dahan, N., Niv, A., Biener, G., Gorodetski, Y., Kleiner, V. and Hasman, E., "Enhanced coherency of thermal emission: Beyond the limitation imposed by delocalized surface waves," *Phys. Rev. B* **76**, 045427 (2007).
- [20] Dahan, N., Nic, A., Biener, G., Gorodetski, Y., Kleiner, V. and Hasman, E., "Extraordinary coherent thermal emission from SiC due to coupled resonant cavities," *J. Heat Transfer* **130**, 112401 (2008).
- [21] Lin, S.Y., Moreno, J. and Fleming, J.G., "Three-dimensional photonic-crystal emitter for thermal photovoltaic power generation," *Appl. Phys. Lett.* **83**, 380 (2003).
- [22] Luk, T.S., Mclellan, T., Subramania, G. Verley, J.C. and El-Kady, I., "Emissivity measurements of 3D photonic crystals at high temperatures," *Photonics and Nanostructures-Fundamentals and Applications* **6**, 81 (2008).
- [23] Marquier, R., Joulain, K., Mulet, J.P., Carminati, R., Greffet, J.J. and Chen, Y., "Coherent spontaneous emission of light by thermal sources," *Phys. Rev. B* **69**, 155412 (2004).
- [24] Sai, H., Yugami, H., Akiyama, Y., Kanamori, Y. and Hane, K., "Spectral control of thermal emission by periodic microstructured surfaces in the near-infrared region," *J. Opt. Soc. Am. A* **18**, 1471 (2001).

- [25] Yeng, Y.X., Ghegreh, M., Bermel, P., Chan, W.R., Joannopoulos, J.D., Soljacic and I. Celanovic, "Enabling high-temperature nanophotonics for energy applications," PNAS **109**, 2280 (2012).
- [26] Le Gall, J., Olivier, M. and Greffet, J.J., "Experimental and theoretical study of reflection and coherent thermal emission by a SiC grating supporting a surface-phonon polariton," Phys. Rev. B **55**, 10105 (1997).
- [27] O'Sullivan, F., Celanovic, I., Jovanovic, N., Kassakian, J., Akiyama, S. and Wada, K., "Optical characteristics of one-dimensional Si/SiO<sub>2</sub> photonic crystals for thermophotovoltaic applications," J. Appl. Phys. **97**, 033529 (2005).
- [28] Vap, J., Nauyoks, S., Fitzgerald, T. and Marciniak, M. A., "Development of a tunable polarimetric optical scattering instrument from 4.3-9.7 Microns," Proc. SPIE **8154**, 815412 (2011).
- [29] Vap, J. Nauyoks, S. and Marciniak, M. A., "Optimization of a mid-wave tunable polarimetric optical scatter instrument," Proc. SPIE **8364**, 836405 (2012).
- [30] Vap, J., Nauyoks, S. and Marciniak, M. A., "Evaluation and optimization of a tunable mid-wave infrared Mueller-matrix polarimeter-scatterometer," Meas. Sci. and Tech, manuscript submitted 1 Nov 2012.
- [31] Vap J., Nauyoks, S., Benson, M., Fitzgerald, T. and Marciniak, M.A., "Tunable infrared Mueller-matrix polarimeter-scatterometer for the evaluation of optical metamaterials," manuscript prepared for submission to Rev. of Sci. Instr.
- [32] Silveirinha, M. and Engheta, N., "Tunneling of electromagnetic energy through subwavelength channels and bends using  $\epsilon$ -near-zero materials," Phys. Rev. Lett. **97**, 157403 (2006).
- [33] Liu, X., Tyler, T., Starr, T., Starr, A.F., Jokerst, N.M., and Padilla, W.J., "Taming the Blackbody with infrared metamaterials as selective thermal emitters," PRL **107**, 045901 (2011).
- [34] Adams, D.C., Inampudi, S., Ribaudo, T., Slocum, D., Vangala, S., Kuhta, N.A., Goodhue, W.D., Podolskiy, V.A. and Wasserman, D., "Funneling light through a subwavelength aperture with epsilon-near-zero materials," Phys. Rev. Lett., **107** 133901 (2011).
- [35] Vap, J. and Marciniak, M.A., "Examining epsilon near zero structures through effective medium theory and optical thin film analysis," Proc. SPIE **8364**, 836426 (2012).
- [36] E.D. Palik, [Handbook of Optical Constants], London-New York (1985).

- [37] Johnson P.B. and Christy R.W., "Optical-constants of noble-metals," *Phys. Rev. B* **6**, 4370 (1972).
- [38] Chipman, R.A., [Handbook of Optics, 3<sup>rd</sup> Edition], Chapter 14, McGraw Hill (2010).
- [39] Goldstein, D.H. and Chipman, R.A., "Error analysis of a Mueller matrix polarimeter," *J. Opt. Soc. Am. A* **7**(4), 693-00 (1990).
- [40] Chenault, D.B., Pezaniti, J.L. and Chipman, R.A., "Mueller matrix algorithms," *Proc. SPIE* 1726, 231-46 (1992).
- [41] Azzam, R.M.A., "Photopolarimetric measurement of the Mueller matrix by Fourier analysis of a single detected signal," *Opt. Lett.* **2**(6), 148-50 (1978).
- [42] Sabatke, D.S., Descour, M.R., Dereniak, E.L., Sweatt, W.C., Kemme, S.A. and Phipps, G.S., "Optimization of retardance for a complete Stokes polarimeter," *Opt. Lett.* **25**, 802-04 (2000).
- [43] Smith, M., "Optimization of a dual-rotating retarder Mueller matrix polarimeter," *Appl. Opt.* **41**, 2488 (2002).
- [44] Stover, J. C., [Optical Scattering Measurement and Analysis], SPIE Press (1995).
- [45] Schott, J.R., [Fundamentals of Polarimetric Remote Sensing], SPIE Press (2009).
- [46] Goldstein, D., [Polarized Light], CRC Press (2003).
- [47] Schubert, E.F., Kim, J.K. and Xi, J.-Q., "Low-refractive-index materials: A new class of optical thin-film materials," *Phys. Stat. Sol. B* **244**, 3002-08 (2007).
- [48] Xi, J.-Q., Kim, J.K., Schubert, E.F., Ye, D., Lu, T.-M. and Lin, S.-Y., "Very low-refractive-index optical thin films consisting of an array of SiO<sub>2</sub> nanorods," *Opt. Lett.* **31**, 601-03 (2006).
- [49] Xi, J.-Q., Schubert, M.F., Kim, J.K., Schubert, E.F., Chen, M., Lin, S., Liu, W. and Smart, J.A., "Optical thin-film materials with refractive index for broadband elimination of Fresnel reflectance," *Nat. Photon.* **1**, 176-79 (2007).
- [50] Grosso, D., Boissière, C. and Sanchez, C., "Ultralow-dielectric-constant optical thin films built from magnesium oxyfluoride vesicle-like hollow nanoparticles," *Nat. Mat.* **6**, 572-75 (2007).
- [51] Chi, F., Yan, L., Yan, H., Jiang, B., Lu, H. and Yuan, X., "Ultralow-refractive-index optical thin films through nanoscale etching of order mesoporous silica films," *Opt. Lett.* **37**, 1406-08 (2012).

- [52] Schwartz, B.T., Piestun, R., "Waveguiding in air by total external reflection from ultralow index metamaterials," *App. Phys. Let.* **85**, 1-3 (2004).
- [53] Brown, J., "Artificial dielectrics having refractive indices less than unity," *Proc. IRE* **100C**, 51-62 (1953).
- [54] Rotman, W., "Plasma simulation by artificial dielectrics and parallel-plate media," *IRE Trans. Antennas Propag.* **10**, 82-95 (1962).
- [55] Garcia, N., Ponizovskaya, E.V., and Xiao, J.Q., "Zero permittivity materials: band gaps at the visible," *Appl. Phys. Let.* **80**, 1120-22 (2002).
- [56] Schwartz, B.T. and Piestun, R., "Total external reflection from metamaterials with ultralow refractive index," *J. Opt. Soc. Am. B* **20**, 2448-53 (2003).
- [57] Edwards, B., Alù, A., Young, M. E., Silveirinha, M., and Engheta, N., "Experimental verification of epsilon-near-zero metamaterial coupling and energy squeezing using a microwave waveguide," *Phys. Rev. Let.*, **100**, 033903 (2008).
- [58] Born, M. and Wolf, E., [Principles of Optics], Cambridge University Press, New York (2006).
- [59] Schiff, T. C., Stover, J. C., Bjork, D. R., Swimley, B. D., Wilson, D. J. and Southwood, M. E., "Mueller matrix measurements with an out-of-plane polarimetric scatterometer," *Proc. SPIE* 1746, 295-306 (1992).
- [60] Germer, T. and Asmail, C., "Goniometric optical scatter instrument for out-of-plane ellipsometry measurements," *Rev. of Sci. Instr.* **70**(9), 3688-95 (1999).
- [61] Bahar, E. and Kubik, R., "Description of versatile optical polarimetric scatterometer that measures all 16 elements of the Mueller matrix for reflection and transmission: application to measurements of scatter cross sections, ellipsometric parameters, optical activity, and the complex chiral parameter," *Opt. Eng.* **47**(9), 093603 (2008).
- [62] Weiwei, F. and Qingnong, W., "A scatterometer for measuring the polarized bidirectional reflectance distribution function of painted surfaces in the infrared," *Infrared Physics and Technology* **51**, 559-63 (2008).
- [63] Liu, C., Liu, T. and Fu, W., "Out-of-plane ellipsometry measurements of nanoparticles on surfaces for thin film coated wafer inspection," *Optics and Laser Technology* **42**, 902-10 (2010).
- [64] Liu, C., Fu, W., Lin, T., Chang, C. and Chen, J., "Nanoscale surface roughness characterization by full field polarized light-scattering," *Optics and Lasers in Engineering* **49**, 145-51 (2011).

- [65] Shen, Y., Zhu, Q. and Zhang, Z., "A scatterometer for measuring the bidirectional reflectance and transmittance of semiconductor wafers with rough surfaces," *Rev. of Sci. Instr.* **74**(11), 4885-92 (2003).
- [66] Hauge, P. S., "Mueller matrix ellipsometry with imperfect compensators," *J. Opt. Soc. Am.* **64**, 1519-28 (1978).
- [67] Compain, E., Poirier, S., and Drevillon, B., "General and self-consistent method for the calibration of polarization modulators, polarimeters, and Mueller-matrix ellipsometers," *Appl. Opt.* **38**(16), 3490-3502 (1999).
- [68] Fitzgerald, T.M. and Marciniak, M.A., "Full optical scatter analysis for novel photonic and infrared meta-materials," *Advances in Science and Technology* **75**, 240 (2010).
- [69] Fitzgerald, T.M., Marciniak, M.A. and Nauyoks, S.E., "Development of a tunable polarimetric scatterometry system in the MWIR and WLIR," *Proc. SPIE* **7792**, 779209 (2010).
- [70] Fujiwara, H., [Spectroscopic Ellipsometry Principles and Applications], Wiley (2007).
- [71] Maier, S.A., [Plasmonics Fundamentals and Applications], Springer (2007).
- [72] Sellers, S.R., Vap, J., Nauyoks, S.E., Marciniak, M.A., and Ku, Z., "Investigation of surface plasmonic extraordinary transmission for spectral, polarimetric, and off-normal incidence," *Proc. SPIE* **8457**, 845730 (2012).
- [73] "RefractiveIndex.INFO." – *Refractive Index Database*. n.p., n.d. Web. 9 Nov. 2012. <<http://refractiveindex.info/>>.
- [74] Dayal, G. and Ramakrishna, S.A., "Design of highly absorbing metamaterials for infrared frequencies," *Opt. Exp.* **20**, 17503-08 (2012).
- [75] Jaradat, H. and Akyurtlu, A., "Infrared (IR) absorber based on multiresonant structure," *IEEE Antennas and Wireless Propagation Letters* **11**, 122-25 (2012).
- [76] Hendrickson, J., Guo, J., Zhang, B., Buchwald, W. and Soref, R., "Wideband perfect light absorber at midwave infrared using multiplexed metal structures," *Opt. Lett.* **37** 371-73 (2012).
- [77] D'Archangel, J.A., Boreman, G.D., Shelton, D.J., Sinclair, M.B. and Brener, I., "Releasable infrared metamaterials," *J. Vac. Sci. Technol. B* **29**, 051806 (2011).
- [78] Talghader, J., Gawarikar, A.S. and Shea R.P., "Spectral selectivity in infrared thermal detection," *Light: Science and Applications* (2012).

- [79] Ginn, J.C. and Brener, I., “Realizing optical magnetism from dielectric metamaterials,” *Phys. Rev. Lett.* **108**, 097402 (2012).

REPORT DOCUMENTATION PAGE				Form Approved OMB No. 074-0188	
<p>The public reporting burden for this collection of information is estimated to average 1 hour per response, including the time for reviewing instructions, searching existing data sources, gathering and maintaining the data needed, and completing and reviewing the collection of information. Send comments regarding this burden estimate or any other aspect of the collection of information, including suggestions for reducing this burden to Department of Defense, Washington Headquarters Services, Directorate for Information Operations and Reports (0704-0188), 1215 Jefferson Davis Highway, Suite 1204, Arlington, VA 22202-4302. Respondents should be aware that notwithstanding any other provision of law, no person shall be subject to any penalty for failing to comply with a collection of information if it does not display a currently valid OMB control number.</p> <p><b>PLEASE DO NOT RETURN YOUR FORM TO THE ABOVE ADDRESS.</b></p>					
1. REPORT DATE (DD-MM-YYYY) Dec 2012		2. REPORT TYPE Doctoral Dissertation		3. DATES COVERED (From – To) Sept 2009 – Nov 2012	
4. TITLE AND SUBTITLE Design and Characterization of Optical Metamaterials Using Tunable Polarimetric Scatterometry				5a. CONTRACT NUMBER	
				5b. GRANT NUMBER	
				5c. PROGRAM ELEMENT NUMBER	
6. AUTHOR(S) Vap, Jason C., Maj, USAF				5d. PROJECT NUMBER N/A	
				5e. TASK NUMBER	
				5f. WORK UNIT NUMBER	
7. PERFORMING ORGANIZATION NAMES(S) AND ADDRESS(S) Air Force Institute of Technology Graduate School of Engineering and Management (AFIT/EN) 2950 Hobson Way, Building 640 WPAFB OH 45433-7765				8. PERFORMING ORGANIZATION REPORT NUMBER AFIT-ENP-DS-12-03	
9. SPONSORING/MONITORING AGENCY NAME(S) AND ADDRESS(ES) Intentionally left blank				10. SPONSOR/MONITOR'S ACRONYM(S)	
				11. SPONSOR/MONITOR'S REPORT NUMBER(S)	
12. DISTRIBUTION/AVAILABILITY STATEMENT APPROVED FOR PUBLIC RELEASE; DISTRIBUTION UNLIMITED					
13. SUPPLEMENTARY NOTES This material is declared a work of the U.S. Government and is not subject to copyright protection in the United States					
14. ABSTRACT Optical metamaterials are a class of engineered materials with a wide range of material properties and an equally wide range of anticipated applications. This research targets optical metamaterials in two ways. First, the dimensional constraints necessary to bring effective medium theory (EMT) into agreement with the already well-established transfer matrix method (TMM) modeling for a periodic, stratified (metal-dielectric) near-zero permittivity structure were determined. This provided a path to leverage the use of EMT in the design of near-zero permittivity structures and accurately predict its post-fabrication behavior. Second, the first tunable infrared (IR) Mueller matrix polarimeter-scatterometer was developed to capture the full-directional, full-polarimetric behavior of IR metamaterials. Modeling was used to determine the optimal dual rotating retarder configuration to apply to the instrument design, which was subsequently implemented. Free-space measurements corroborated the optimized design with Mueller matrix extractions having less than 1% error. The instrument was then used to measure a unique metamaterial absorber at 5 microns and captured the polarimetric behavior of a surface plasmon polariton resonance as a function of incident angle. Modeling was used to distill the s-polarized and p-polarized reflectance behavior and phase differences in the reflectances that led to the resonant signature in the measured results. As a final step, the measured results were used to predict the reflectance behavior of the material against a series of incident canonical polarization states.					
15. SUBJECT TERMS Dual Rotating Retarder, Polarimetry Scatterometry, Metamaterials, Near-Zero Permittivity					
16. SECURITY CLASSIFICATION OF:			17. LIMITATION OF ABSTRACT	18. NUMBER OF PAGES	19a. NAME OF RESPONSIBLE PERSON
a. REPORT	b. ABSTRACT	c. THIS PAGE			Marciniak, Michael A., PhD, ENP
U	U	U	UU	131	19b. TELEPHONE NUMBER (Include area code) (937) 255-6565, x 4529 (michael.marciniak@afit.edu)